UNIVERSITY OF
BIRMINGHAM

MICROBUBBLE DYNAMICS NEAR RIGID BOUNDARIES

by

Mehdi Hassan Mahmud

A thesis submitted to
The University of Birmingham
for the degree of
Doctor of Philosophy

School of Mathematics
The University of Birmingham
January 2020

Abstract

This thesis is concerned with the interaction of a microbubble with rigid boundaries. This phenomenon is associated with comprehensive and critical applications such as cavitation erosion, cavitation cleaning, sonochemistry, biomedical ultrasonics and underwater explosions. Our numerical model is based on the viscous potential theory coupled with the boundary integral method. The Lagrangian time integration is used to update the bubble surface and the potential on the bubble surface. We described the physical, mathematical and numerical model for bubble dynamics. A Post-Processor was implemented for displaying bubble motion, velocity field and pressure contour. Three typical cases have been investigated. The first case is for a bubble at a corner consisting of two flat rigid walls. The Green function is obtained, satisfying the impenetrable conditions at the rigid walls using the method of images. The computational results agree well with the experimental data. Parametric studies were accomplished in terms of bubble stand-off distances from the two walls, corner angles, etc. The second case is for the interaction of a microbubble with a suspended spherical particle based on a nonlinear interaction model. The computational results are again in good agreement with the experimental results for this case. Our computations show that the particle and the bubble move away during expansion and move back during the collapse stage. The third case is a bubble in a circular cylinder. The model was firstly validated with experimental data. Numerical analyses were performed in terms of the tube radius, tube length, the eccentricity of the bubble from the axis of the symmetry, etc.

Acknowledgements

I would like to sincerely thank my supervisors, Dr. Qianxi Wang and Dr. Warren R. Smith for their unfaltering support and guidance throughout the years. Their immense knowledge of bubble dynamics provided me with invaluable insights into the field. Without their continuous feedback this PhD would not have been achievable.

I would also like to show my appreciation to the University of Birmingham itself and all staff members in the Mathematics School who have assisted me on several occasions. The learning environment here allowed me to thrive and fulfil my potential.

I wish to express my wholehearted gratitude to the 'Higher Committee for Education Development in Iraq' for the scholarship I have received as well as all the support from the Kurdistan Regional Government (KRG).

I would like to dedicate this thesis to my father and my late mother. Their tenacity and supportive outlook on education inspired me to accomplish this endeavour. Finally, I would like to thank my family and friends, mainly Dr. Kawa Manmi and my beloved wife Catrin. Thank you for your ongoing faith in this project.

LIST OF PUBLICATIONS

Wang, Q., Mahmud, M., Cui, J., Smith, W.R. and Walmsley, A.D., 2020. Numerical investigation of bubble dynamics at a corner. *Physics of Fluids*, 32(5), p.053306.

Contents

List of Figures

List of Symbols

$\boldsymbol{r}$	position vector	t	time
$\boldsymbol{v}$	velocity vector	$\boldsymbol{a}$	acceleration
φ, Υ, Ψ	velocity potential	ψ	normal velocity
Ω	fluid domain	$\partial\Omega$	calculation domain
S	surface of the domain	V	volume
M	number of triangular elements on $\partial\Omega$	N	number of vertices on $\partial\Omega$
$\boldsymbol{I}$	Kelvin impulse	$\boldsymbol{F}$	force
p	pressure	κ	Specific heat of a liquid
R, $\mathfrak{R}$	radius	R_m	maximum bubble radius
L, ℓ	length	r_c	curvature radius
c	solid angle	C	viscose correction constant
R_e	Reynolds's number	W_e	Weber number
δ	buoyancy	ε	dimensionless pressure
ρ	density	σ	surface tension
γ	stand-off distance	λ	weight parameter
α, β, θ	angles	ξ	eccentricity
D/Dt	Lagrangian derivative	$\partial/\partial t + \boldsymbol{v} \cdot \nabla$	Eulerian derivative

Chapter 1

Introduction

Cavitation is the creation of vapour bubbles in a fluid at low-pressure areas. For instance, in the operation of water turbines, centrifugal pumps, and marine propellers, cavitation occurs as a result of the accelerated liquid to high velocities. Authentically, liquid always includes a substantial number of gas particles or nano air-bubbles that acts as cavitation nuclei, which may not be evident to the naked eyes. When the fluid pressure decreases to vapour pressure, cavities begin to develop. Subsequently, the pressure is further reduced, causing vapour bubbles to expand simultaneously with the flow. Unexpectedly, when vapour cavities reach regions of higher pressure, they start to collapse . The sudden expansion and collapse of these vapour cavities produce extreme pressure that hit the near surfaces and cause damage.

1.1 Application background

The study of cavitation bubbles can be divided into two principal domains. Firstly, uncontrolled cavitation bubbles can create a destructive force as observed in hydrodynamic systems such as pumps, turbines, and propellers. Thus, the primary concern of bubble dynamics near rigid boundaries is associated with cavitation damage to pumps, turbines, and propellers (Blake and Gibson, 1987; Brennen, 2013; Lauterborn and Kurz, 2010; Rayleigh, 1917). The subsequent motion of cavitation bubbles can cause severe degradation to surrounding structures in many industrial systems (see Figure 1.1(b)). Secondly,

when cavitation is controlled precisely, we can observe many beneficial uses of bubbles. One of the most significant current discussions in bubble dynamics is cavitation near rigid materials, particularly due to its important role in different areas of science and engineering. Such areas include micro-fluids (Wu et al., 2012), chemistry (Virot et al., 2010), and medicine (Brennen, 2015; Freund, Colonius and Evan, 2007). The characteristics of the interaction between a cavitation bubble and rigid/elastic boundaries has become the focus of many technical fields, for instance water conservancy, shipbuilding, the chemical industry, and many other industries (Luo et al., 2018; Wang, 1998).

(a) (b)

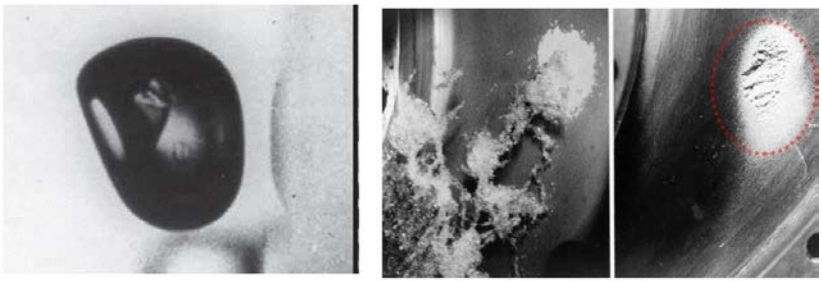

Figure 1.1: Experimental images of bubble cavitation, (a) The formation of an inclined jet near a rigid wall adapted from (Benjamin and Ellis, 1966) and taken by Albert Ellis (Brennen, 2015), and (b) cavitation damage on the hub of a centrifugal pump impeller (Soyama, 1992).

Surface cleaning is one of the most widely used applications of bubble-boundary interactions (Chahine et al., 2016; Dijkink and Ohl, 2008). More specifically, it can be used to clean non-simple surfaces which are difficult to access, such as various medical tools, with the help of both pressure waves and the bubble interacting with the surface. Figure 1.1(a) illustrates the dynamics of individual millimetre-sized cavitation bubbles. It depicts that by the end of the collapse stage a high-speed jet forms towards the rigid wall. Due to the size of the bubble, the jet is inclined upwards and might contribute to the cavitation damage (Brennen, 2015). Bubbles are also observed in sonoluminescence and sonochemistry phenomena (Kolasinski, 2014; Lugli and Zerbetto, 2007). In both of

these phenomena, a high-temperature (in excess of 5000 K) and a high-pressure (exceeding 1000 atm) are achieved as a result of conversion of the kinetic energy of the liquid due to bubble collapse. A unique type of chemical reaction forms as a consequence, due to the combination of rapid heating and cooling rates which are associated with acoustic cavitation and bubble collapse during ultrasonic irradiation (Kolasinski, 2014).

Recent developments in cavitation bubbles have heightened the interest in various medical applications. In medicine, shockwave lithotripsy is a crucial technique in kidney stone destruction which is based on collapsing bubble shockwave propagation (Bailey et al., 2006; Freund, Colonius and Evan, 2007; Johnsen and Colonius, 2008; Maeda et al., 2016). Due to the violent oscillation of cavitation microbubbles near a kidney stone, under the lithotripter shock wave, a liquid jet forms and destroys the surface of the kidney stone. Also, during the procedure, the microbubbles would collapse in on themselves (inertial cavitation). The past decade has seen the rapid development of the implementation of bubble-boundary interactions in medical applications, including tissue ablating (histotripsy) (Roberts et al., 2006; Coussios et al., 2007), extracorporeal shock wave lithotripsy (Klaseboer, Khoo and Hung, 2005; Calvisi, Iloreta and Szeri, 2008; Iloreta, Fung and Szeri, 2008), oncology and cardiology (Leslie and Kennedy, 2006). Thus, due to bubble-bubble and bubble-wall interaction, the above procedure may be harmful and cause vascular injuries such as kidney edema, haemorrhage, and haematomas (Lugli and Zerbetto, 2007; Sreedhar, Albert and Pandit, 2017). Therefore, a more profound understanding of the bubble-bubble and bubble-wall interactions is fundamental to reducing the aforementioned side effects. The dynamics of tiny microbubbles occurring near boundaries subject to an acoustic wave are associated with applications in biomedical ultrasonics (Coussios et al., 2007; Curtiss et al., 2013; Lauterborn and Mettin, 2015; Manmi and Wang, 2017; Vyas et al., 2016, 2017), and ultrasonic cavitation cleaning (Chahine et al., 2016; Ohl and Allison, 2006). However, the exact cleaning mechanisms induced by bubbles have not yet been explained clearly. What is not yet clear is the relative contribution of shockwaves,

jets, and other phenomena.

Bubbles are also used in industry for ultrasonic homogenization. Here, an intense sonic pressure wave is generated in a liquid media, and under the right conditions, microbubbles form rapidly. Subsequently, the formed bubbles grow and merge until they reach their resonant size, which is followed by violent vibration and eventually collapse (Dhankhar, 2014). Moreover, the shockwave emitted from the implosion of vapour bubbles has sufficient energy to break covalent bonds. Cavitation is also being researched for use in biological wastewater treatment (cleaning) (Dular et al., 2016; Shrikant and Khambete, 2017).

Bubbles generated by underwater mine or a torpedo, are subjected to very high-pressure and have the potential to be highly damaging. Undoubtedly, the resulting shock from the explosion is less harmful than the fluid dynamics following their creation. In laser-based surgical techniques, active use of the fluid motion can be greatly beneficial, due to the generation of high-pressure microbubbles through laser vapourization of the liquid (Brennen, 2015; Fuster, 2019). High-Intensity Focused Ultrasound techniques (HIFU), and pulsed high-intensity focused ultrasound techniques (pHIFU) use other important properties of bubble dynamics for medical purposes. HIFU was used for non-invasive thermal destruction of benign and malignant tumours (Li, 2014). Throughout the HIFU, an intense acoustic energy is delivered into a small region within the body. Another vital factor which can be considered is the contribution of bubble-induced heating, as it can be several times higher than the usual heat deposition from the conversion of energy from the primary ultrasound field (Farny, Holt and Roy, 2009; Pahk et al., 2018). The pHIFU therapy causes transient bubble activity using short pulses, produced at low pulse recurrence frequency. It has been shown that this procedure enhances drug and gene delivery to tissues (Li et al., 2014).

Bubbles can also be used in drug delivery applications. Here, encapsulated bubbles are directed towards a specific part of the body and are then subsequently exploded to

release drugs. This significantly increases the efficiency of the treatment process. In this technique, the thermal effects together with the shear stresses are competing mechanisms which are influenced by the presence of bubbles (Brennen, 2015). However, the overall efficiency of medical treatment techniques is unclear. The dynamics of an acoustic microbubble in a deformable vessel has been the subject of recent research (Dindyal and Kyriakides, 2011; Wang et al., 2018). A related medical application is sonography. More specifically, for the purpose of the ultrasound imaging, microbubbles are injected into the bloodstream to make a contrast agent. They are often used in clinical ultrasonic diagnoses due to the considerable difference in compressibility between the microbubbles and surrounding tissues.

1.2 Literature review

Cavitation phenomena were first postulated by Euler in 1754, however cavitation was actually discovered much later in 1893 by Barnaby and Parsons (Li, Brennen and Matsumoto, 2015). They discovered that the failure of the British high-speed warship HMS Daring in 1885 was caused by the formation of cavitation bubbles on the propeller blades. Parsons established the first water tunnel to study cavitation in 1895, and he discovered that the damage to the propeller is associated with the cavitation. One of the most fundamental works on the subject of cavitation was written by Osborne Reynolds and entitled 'On the dynamical theory of incompressible viscous fluids and the determination of the criterion' (1894).

In the aforementioned article, Reynolds made observations on the formation of bubbles as they passed through a constriction in a tube. This later became crucial to the understanding of why steamboat propellers experienced a fast decline in performance (1915). These pioneering works led to the discovery of the exceptional abilities of these tiny bubbles to release an intense energy during their collapse, and their capacity to erode most materials in any fluid machinery. Cavitation thus became the principal focus of research

in turbo-machinery and in industry. It became apparent that bubbles can cause a large amount of wear and tear on hydraulic devices, due to the hydraulic blows resulting from the violent collapse of cavities. Slightly later investigations concerning cavitation can also be traced back to 1917. These later investigations aimed to understand the response of hydrodynamic cavitation flows and the interaction mechanisms between the bubbles and pressure waves (Rayleigh, 1917). By predicting the collapse of an empty cavity in a large mass of liquid, Rayleigh laid the theoretical foundation for cavitation.

The dynamics of a single bubble have been intensely investigated theoretically, experimentally, and numerically for hundreds of years. Many pioneering studies have shown that the collapse of these cavitation bubbles near rigid boundaries results in high-speed re-entrant liquid jets. The resulting jets penetrate the bubbles and strike the nearby boundary generating a hammer-like water pressure (Chahine, 1982; Crum, 1979; Naude and Ellis, 1961; Plesset and Chapman, 1971).

Throughout the years, a wide range of techniques have been developed to demonstrate cavitation in computational fluid dynamics applications (CFD). Each of these methods has its area of use, and some methods will be computationally too expensive to even consider. Another significant decision lies with the fact that the cavitation can be modelled in compressible or incompressible fluids. Theoretically, the Rayleigh-Plesset equation (RPE) or relative equations based on the RPE are suitable tools to predict the motion of spherical or nearly spherical bubbles in an incompressible liquid (Rayleigh, 1917). The Keller-Miksis formulation (KMF) is another model used to describe the oscillatory behaviour of a bubble in a fluid with the effects of acoustic radiation. The major difference between the KMF and RPE is that the KMF does not assume the liquid to be incompressible (Keller and Kolodner, 1956; Keller and Miksis, 1980). Some other types of equations considering the compressibility of the fluid and time-dependency of the pressure fields are the Gilmore model or equations by Tomita and Shima (Shima and Tomita, 1977, 1981).They used the perturbation technique to derive the equation of motion of a spherical bubble in a viscous

compressible liquid.

Numerically, traditional methods such as the boundary integral method (BIM) (Wang and Manmi, 2014; Wang, 1998; Zhang, Duncan and Chahine, 1993), the finite element method (FEM) (Liu et al., 2018; Tian et al., 2018), the finite volume method (FVM) (Li et al., 2018; Koukouvinis et al., 2016) and other new methods such as the lattice Boltzmann method (LBM) (Peng et al., 2018; Wang, Shi and Zhang, 2015) are used to predict the bubble motion and migration. A 3D-numerical model for the interaction of a bubble and nearby movable structures is established by Harris (1993) which thereafter became a tool for many numerical studies is known as the loose coupling model (LCM) (Borkent et al., 2008; Chahine, Kalumuck and Hsiao, 2003; Li, Sun and Zong, 2013; xia Wang et al., 2018). Recently, a coupled system of BIM-FEM has been developed to address bubble dynamics near elastic boundaries. Kalumuck, Duraiswami and Chahine (1995) have coupled a fully fluid-structure model using their existing BIM and FEM code. They observed significant effects on the bubble dynamics due to the structural response including the bubble period, jet formation, and the generated pressure on the solid body. Miao and Gracewski (2008) utilised this method for an axisymmetric simulation of the linear interaction between a bubble near an infinite elastic surface and a confined bubble in an elastic tube. Their results agreed well with the experimental results of Brujan et al. (2001). Wang et al. (2020) simulated the dynamics of explosion bubbles and their interactions with stiffened structures. In their method, the bubbles physical characteristics is investigated using BIM , while the FEM is utilzed to calculate the structural response. However, the axisymmetric simulation had limitations, leading to the inability to model the jet development towards the tube wall. Also, coupling the BIM/vortex ring for the fluid dynamics and FEM model for a plate has been used in the three-dimensional simulation of the interaction between a toroidal bubble and an elastic plate by Klaseboer et al. (2005). They successfully captured the plastic deformation of the steel plate which was caused by the dynamics of the explosion bubble.

The BIM is grid-free in the flow domain. The axisymmetric BIM has been implemented for the motion of a bubble near a rigid wall or a free surface (Calvisi et al., 2007; Gordillo and Pérez-Saborid, 2006; Wang and Blake, 2010, 2011). The BIM is an efficient method of analysing this interaction, as demonstrated by its extensive application in this area of study (Best, 1993; Blake and Gibson, 1981, 1987; Brujan et al., 2002; Chahine and Bovis, 1980; Guerri, LuccA and Prosperetti, 1981; Lee, Klaseboer and Khoo, 2007; Lucca and Prosperetti, 1981; Ohl and Allison, 2006; Pearson et al., 2004; Taib, 1985; Zhang, Duncan and Chahine, 1994, 1993). The three-dimensional BIM was implemented for the motion of bubbles near free surfaces, inclined walls, and a rigid body (Blake et al., 1997; Chahine and Perdue, 1988; Joseph and Wang, 2004; Klaseboer et al., 2005; Manmi and Wang, 2017; Manmi, 2015; Wang, 1998; Zhang, Zhang and Deng, 2019).

In engineering applications, experimental methods are implemented. For instance, an underwater explosion bubble generated using a TNT charge (Hung and Hwangfu, 2010), high-pressure air-gun generated bubbles (De Graaf, Brandner and Penesis, 2014), and so on. Also, there are many alternative experimental methods used to generate bubbles, such as by spark (Ohl et al., 2015), focused laser beam (Brujan et al., 2018; Lindau and Lauterborn, 2003; Vogel, Lauterborn and Timm, 1989) and so on. Vogel, Lauterborn and Timm (1989) captured the micro jetting flows for asymmetric collapsing bubbles. They described a relationship between the stand-off distance γ (the distance between the bubble centroid at inception and the surface of the wall) and the noises induced by bubble collapse. Gonzalez-Avila and Ohl (2018) measured the pressure emission of laser-induced bubble collapse. For a bubble close to a rigid boundary, the pressure amplitude was found to be up to $1k$ Bar.

The past decade has seen rapid development in the understanding of the bubble's collapsing behaviour near a flat rigid wall. It has been treated with various degrees of sophistication both theoretically and experimentally. Subsequently, various exciting dynamical features of the collapsing bubble have been observed, such as bubble formation,

motion, jet formation, jet penetration, and bubble rebound. A collapsing bubble migrates to a flat rigid boundary resulting in the creation of a high-speed liquid jet on the distal side pointing towards the boundary and reaching velocities of the order of 100 ms^{-1} (Benjamin and Ellis, 1966; Brujan et al., 2002; Lauterborn and Bolle, 1975; Plesset and Chapman, 1971; Taib, 1985; Tomita and Shima, 1986; Zhang, Duncan and Chahine, 1993). Furthermore, after time has progressed from the bubble inception, jetting leads to fluid transport and a local concentration of energy (Han et al., 2015). Several studies thus far have linked physical action of liquid jets with surface damage and erosion (Benjamin and Ellis, 1966; Philipp and Lauterborn, 1998; Tomita and Shima, 1986). However, with sufficient control over the established effect, jetting might be beneficial (Chahine, 1977; Blake and Gibson, 1981; Blake, Taib and Doherty, 1986; Brujan et al., 2001; Shima et al., 1981; Wang and Blake, 2010, 2011).

The jet concentrates momentum along its direction and influences on a small area of the boundary. This concept is considered to be one of the principal mechanisms of damaging or cleaning a rigid boundary (Chahine et al., 2016; Hsiao et al., 2014). The emitted shock waves from the torus ring coming into contact with the boundary are the extra main cause of cavitation erosion (Philipp and Lauterborn, 1998; Tomita and Shima, 1986; Wang, 2014). Further investigations have been carried out on the jet velocity (Shima et al., 1981; Philipp and Lauterborn, 1998; Vogel, Lauterborn and Timm, 1989), bubble centroid translations (Blake, Tomita and Tong, 1998; Brujan et al., 2001; Wang, 1998; Wang and Khoo, 2004), shockwave emissions after the bubble rebound (Lindau and Lauterborn, 2003; Vogel, Lauterborn and Timm, 1989), luminescence pulse (Brujan et al., 2005; Ohl, Lindau and Lauterborn, 1998), the viscoelasticity effects of the liquid (Brujan, Ikeda and Matsumoto, 2004; Chahine, 1982), the calculation of the pressure contours and the velocity vectors in the surrounding liquid (Brujan, Pearson and Blake, 2005; Li et al., 2016; Pearson, Blake and Otto, 2004).

Multi-bubble interaction is another interesting research direction. A number of in-

vestigations have been carried out experimentally (Bremond et al., 2006; Chew et al., 2011; Fong et al., 2009; Sankin, Yuan and Zhong, 2010; Tomita, Sato and Shima, 1994), and computationally (Bremond et al., 2006; Blake et al., 1993; Fong et al., 2009; Hsiao et al., 2013). More recent researches are focused on other types of rigid boundaries. For example, the bubble dynamics between two parallel walls (Chahine, 1982; Hsiao et al., 2013; Ishida et al., 2001; Kucherenko and Shamko, 1986; Shima and Sato, 1980; Ueki, Kimoto and Momse, 1984). The radial jet formation can be regarded as one of the most interesting behaviours of the bubble as it causes a bubble to split and form two axial jets in the direction of the walls.

Recently, Zhang, Zhang and Deng (2019) investigated numerically the collapses of both a single cavitation bubble and a cluster consisting of 8 bubbles. their main concern was on the conversions between different forms of energy. For a single bubble near a solid wall, they have found that the rate of energy conversion declines with the stand-off distance, γ, between the wall and the bubble centroid. However, for the collapse of multiple bubbles, this relationship reverses. Furthermore, in reality, there are clouds of bubbles in the system. Large numbers of bubbles with varying sizes form the cavitation cloud that collapses either adjacent to the rigid boundaries or in the bulk liquid. Ohl, Klaseboer and Khoo (2015) paid particular attention to the cloud bubbles in the context of high-intensity focused ultrasound, which is of major importance in biomedical applications.

Bubbles oscillate spherically under the condition that the surrounding liquid of the bubble is isotropic and requires the stability conditions regarding the spherical shape to be fulfilled, such as parametric and Rayleigh-Taylor instability (Plesset, 1954; Chahine, 1982; Lucca and Prosperetti, 1981; Ohl, Lindau and Lauterborn, 1998; Lauterborn et al., 1999).The collapsed bubbles, eventually become either spherically symmetric or asymmetric. Due to the environmental effect on the bubble, asymmetry becomes established and consequently, when the bubble is far from rigid boundaries or when the pressure gradient, which drives the collapsed bubble, is relatively small, the bubble remains approximately

spherical (spherically symmetric collapse) (Benjamin and Ellis, 1966; Sreedhar, Albert and Pandit, 2017). However, for large bubbles, due to the effects of gravity, the spherical form becomes unstable (Benjamin and Ellis, 1966; Wang, 1998). During a spherically symmetric collapse, with the presence of rigid boundaries, the pressure and temperature inside the bubble rise drastically (Sreedhar, Albert and Pandit, 2017). Consequently, the radial inward movement of the bubble stops and the bubble rebounds followed by a pressure transient that evolves into a shock wave. The wave-boundary interaction results in damage to the solid surface. Asymmetric collapse occurs in the case of cavities attached or adjacent to a solid boundary or when the bubble is affected by other external forces (Han et al., 2016; Wang and Manmi, 2014; Manmi, 2015; Tagawa and Peters, 2018). However, the collapse type of a bubble depends on its closeness to the boundary. When the bubble is relatively far from the borders, it can collapse multiple times before it is fragmented and dissolves in the liquid.

Relatively, much less research has been carried out on bubble dynamics near non-flat rigid boundaries. However, geometries in applications are usually more complicated than just a plane surface. Tomita et al. (2002) studied a bubble collapsing near a curved rigid boundary for an axisymmetric configuration, using high-speed photography and the boundary integral method (BIM). They observed that collapsed bubble near a curved boundary, produces higher jet velocity and higher pressures can occur, which may be more significant than the one near a flat boundary. Tomita et al. (2002) claimed that "The most pronounced migration takes place when a boundary is slightly concave, which is completely different to the convex boundary case where a drastic suppression of translational bubble motion is evident". Also, by decreasing the curvature, the velocity of a liquid jet impacting on the boundary surface tends to increase. Brujan et al. (2018) studied the behaviour of a laser-induced cavitation bubble near two perpendicular rigid walls. A liquid jet is formed during bubble collapse stage tending to the surface of the near-wall and inclined to the far-wall. Subsequently, and the bubble migrates in the direction of the jet.

In recent years, there has been an increasing interest in the interaction of a small particle with the dynamics of bubbles in a liquid. It has increased the attention of researchers due to several unique and exciting applications. For example, a cavitation bubble created by laser, spark or ultrasound can move nearby particles in a particular direction (Arora, Ohl and Mørch, 2004; Borkent et al., 2008; Ohl et al., 2015; Poulain et al., 2015). Also, surface cleaning from the small particles; the interaction between sand particles and cavitation bubbles have an impact on turbine blades (Watanabe and Hashimoto, 1996; Xu et al., 2017; Zhang et al., 2016). Moreover, particle-induced bubble jets can be used for microinjection or damaging tumour cells (Goh et al., 2017; Helfield et al., 2016; Sankin, Yuan and Zhong, 2010). However, the harmful effects caused by the bubbles is another side of the research area in cavitation bubble such as the emitted shock wave in the final collapse of a cavitation bubble (Brennen, 2013; Brujan, Ikeda and Matsumoto, 2005; Lauterborn and Kurz, 2010; Lauterborn and Vogel, 2013; Philipp and Lauterborn, 1998; Supponen et al., 2017). In practical applications, bubble shapes are affected by the boundary and shape of the particles. Nevertheless, a few pieces of research were focused on this matter. Lv et al. (2019) investigated the interactions between a laser-generated cavitation bubble and a spherical particle experimentally. Their analysis was based on the radius ratio and the distance between the bubble and the particle (Poulain et al., 2015).

Additionally, one area that appears to be lacking in research is the dynamics of a bubble in a tube. Bubble dynamics in a tube can be related to drug delivery as the tube can represent a blood vessel. Ory et al. (2000) numerically studied the fluid mechanical aspects of the axisymmetric growth and collapse of a bubble in a narrow tube filled with a viscous liquid. They found that when the bubble is situated on either side of the tube (i.e not at the midpoint), it results in the development of a net flow which can transport fluid from one reservoir to another.

1.3 Techniques for microbubble creation/formation

The way in which microbubbles can be created is developing and changing over time. Microbubble creation in experiments and applications has changed along with the research that involves them, however it is challenging to create microbubbles smaller than 25μm efficiently (Marui, 2013). For instance; in propeller cavitation, bubbles form due to vaporous growth in reduced ambient pressure, in laser beam pulse,bubbles are created by applying locally high-energy in the liquid, and in machines to crush kidney stones, the formation is due to intense acoustical beams, or by spark charge electric inside liquids (Best, 1993; Fuster, 2019; van Wijngaarden, 2016; Han et al., 2015).

Since the 1970s, laser impulses have been used to form microbubbles (Brujan et al., 2002; Lauterborn, 1974; Tong et al., 1999). In this technique, a cavity forms using a strong pulse on the liquid surface which forms a microbubble filled with dissolved gasses and liquid vapour. Also, bubbles can be generated ultrasonically, by laser, hydrodynamic effects, or other techniques. In all of the cases mentioned, initially, micro-size bubbles grow and finally collapse due to the return of high-pressure in their surrounding area. The final stage of the bubble collapse contributes to the cleaning purpose, and therefore it is worthwhile to observe this somewhat further (van Wijngaarden, 2016). Recently, a new technique of creating single microbubble has been developed by a group of chemists in Canada using micro-pipette (Najafi, Xu and Masliyah, 2008).

1.4 Thesis overview

In the present thesis, a three-dimensional boundary integral method (3D-BIM) is used to simulate the bubble dynamics near rigid boundaries. The present work is organized in 5 main chapters as follows:

In Chapter 1, we introduced the phenomenon of cavitation, with reference to the application background and a short history of the beginning of the bubble dynamics. A literature review was presented to describe the most recent work done in the research area

of bubble dynamics.

Chapter 2 illustrates the basic mathematical concepts and physical modelling of bubble dynamics near rigid boundaries as we intend to consider different types of rigid boundaries in our work. For instance, we start to present the dynamics of a bubble near a flat rigid wall using BIM method and then we consider more complicated boundaries such as a corner and spherical particles. Moreover, we discussed the BIM viscous model which is essential when the flow has low Reynolds number or when we consider microbubbles. In the numerical computations, we usually need to improve the mesh quality throughout the iterative procedure, which can be done in a variety of ways. In this chapter, we present two types of mesh improvement with each having its own advantage. The modified elastic mesh technique MEMT, and the volume-preserving smoothing technique VPST are both essential tools to produce better mesh and a more accurate simulation for bubble dynamics. The former will reduce the mesh density around the jet area while the later will reduce the noise around the jet whilst preserving the bubble volume.

In chapter 3, we will study the three-dimensional (3D) bubble dynamics in a corner formed by two flat, rigid boundaries, using the potential flow theory and BIM. Corners are a basic type of non-flat surfaces, which frequently occur in engineering due to practical needs and/or manufacturing procedures. The Green function is obtained to satisfy the impenetrable conditions at the flat rigid boundaries using the method of images. Here we demonstrate how the images together with the original source are symmetric concerning both of the walls. We aim to study the expansion, collapse, and migration of the bubble, the behaviour of the jet, and the pressure contours of the flow field. The predicted bubble shapes have excellent agreement with the published experiments for $\alpha = \pi/2$ as well as the experiments performed for electric spark generated bubbles for $\alpha = \pi/4$. A parametric study is accomplished in terms of the dimensionless standoff distances of the bubble centre at inception from the two walls and the corner angle.

In chapter 4, the bubble dynamics of fully nonlinear interaction of a microbubble with a

suspended spherical particle is investigated using BIM coupled with an auxiliary function method and viscous effects. The particle and the bubble move away during the bubble expansion and move back during the bubble collapse due to the violently expanding and collapsing bubble. To validate the model, the results are compared with two experimental images for fixed and suspended particles. Our results agree well with the experimental images as well as previous studies by (Liu, Wang and Zhang, 2016; Li et al., 2019) in terms of bubble shapes, particle displacement and velocity. Analysis is carried out based on three parameters, particle density, ρ_p, particle radius, R_p, the standoff distance between the bubble centre and the surface of the particle, γ. Further analysis has been undertaken of the effect of the maximum radius, R_m, and the particle mass, m_p.

In chapter 5, the bubble dynamics in a circular cylinder is investigated numerically. We compare the computational results with experimental images by (Wang et al., 2019). Little research has been undertaken for this model. We analyse the dynamics of the bubble by considering the length of the tube and by adding some boundary conditions on the tube caps. With this condition, we are going to show that we may have the same results by considering the tube length as $\ell = 30$, while without the condition, a longer tube must be considered with the length of $\ell = 100$. More analysis is performed to show the effect of the tube radius $\mathfrak{R}$, the maximum bubble volume, and the eccentricity ξ of the bubble from the axis of the symmetry.

Finally, in chapter 6, summary, numerical conclusions, and possible future developments are presented.

Chapter 2

Physical, Mathematical and Numerical Models of Bubble Dynamics using 3D BIM

In this chapter, we present an overview of the basic physical assumptions and mathematical governing equations to model bubble dynamics near a rigid wall as a simple case of rigid boundaries. Initially, a spherical bubble which contains a high-pressure gas is surrounded by a liquid having a domain Ω and boundaries $\partial\Omega$. In addition, detailed descriptions of the surface discretization, boundary integral method (BIM) and its advantages and disadvantages, numerical integration technique on the boundaries, techniques for surface smoothing, and Lagrangian time integration are presented. Moreover, the viscous effect on the bubble dynamics is considered based on the viscous potential flow theory (VPFT) (Joseph and Wang, 2004; Manmi and Wang, 2017; Wang and Khoo, 2004). The viscosity effects will be important as the Reynolds number R_e is small, or when the bubble in micron size. As a result, viscosity will damp the development of the liquid jet and delay the formation of the toroidal bubble. Lastly, we discuss an algorithm based on the boundary integral method BIM for calculating the pressure contours and velocity field in the computational domain.

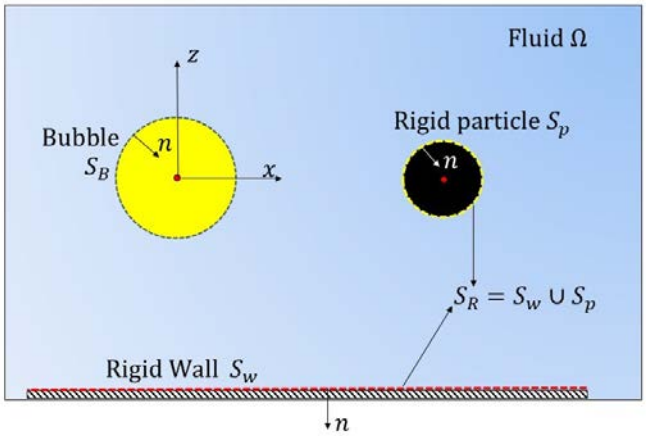

Figure 2.1: Schematic of a bubble near rigid boundaries surrounded by a fluid Ω.

2.1 Physical and Mathematical Modelling

Throughout this thesis we assume that; a spherical bubble is initiated at the origin of the Cartesian coordinate system xyz. It has a surface, S_B, and is surrounded by a fluid having domain Ω (ideally water), in equilibrium, i.e having zero velocity and pressure gradient everywhere.Further, the fluid flow is irrotational and all velocities are sufficiently smaller than the speed of sound in the fluid (c in water is approximately 1500 m/s) i.e (the fluid is incompressible $\nabla \cdot \boldsymbol{v}$=0). The fluid velocity $\boldsymbol{v}$ thus has a potential $\boldsymbol{v} = \nabla\varphi$, satisfying Laplaces equation, $\nabla^2\varphi = 0$. Using the second Green identity, the velocity potential thus transformed into the boundary integral equation as follows

$$c(\boldsymbol{r},t)\varphi(\boldsymbol{r},t) = \int_{\partial\Omega} \Big[\psi(\boldsymbol{q},t)G(\boldsymbol{r},\boldsymbol{q}) - \varphi(\boldsymbol{q},t)\frac{\partial G(\boldsymbol{r},\boldsymbol{q})}{\partial n}\Big] dS(\boldsymbol{q}), \tag{2.1.1}$$

where $\psi(\boldsymbol{q},t) = \partial\varphi(\boldsymbol{q},t)/\partial n$ is the normal velocity, $\boldsymbol{r}$ and $\boldsymbol{q}$ are the field and source points respectively, $\partial\Omega$ represents all the boundaries for the computation of the domain Ω, i.e $\partial\Omega = S_B \cup S_R$, where S_R represents the surface of all rigid boundaries (see figure 2.1). The term $c(\boldsymbol{r},t)$ is the solid angle which for a smooth surface satisfies

$$c(\boldsymbol{r},t) \approx \begin{cases} 4\pi, & \boldsymbol{r} \in \Omega/\partial\Omega, \\ 2\pi, & \boldsymbol{r} \in \partial\Omega. \end{cases} \tag{2.1.2}$$

The outward normal from the flow and the normal derivative can be expressed as $\boldsymbol{n} = (n_x, n_y, n_z)$ and $\partial/\partial n = \boldsymbol{n} \cdot \nabla$ respectively, and the Green function, $G(\boldsymbol{r}, \boldsymbol{q})$, is given by

$$G(\boldsymbol{r}, \boldsymbol{q}) = \frac{1}{|\boldsymbol{r} - \boldsymbol{q}|}. \tag{2.1.3}$$

2.1.1 Kinematic and dynamic boundary conditions

The kinematic boundary conditions on the bubble surface S_B requires a liquid particle on the bubble surface to remain there, i.e.

$$\frac{D\boldsymbol{r}}{Dt} = \nabla\varphi, \ \boldsymbol{r} \in S_B. \tag{2.1.4}$$

On the rigid boundaries

$$\nabla\varphi \cdot \boldsymbol{n} = \boldsymbol{U} \cdot \boldsymbol{n}, \tag{2.1.5}$$

where $\boldsymbol{U}$ is the velocity of the rigid boundary.

The dynamic boundary condition on the bubble surface is obtained from balancing the bubble surface pressure by including surface tension effects for an inviscid fluid as follows

$$p_L = p_B - 2\sigma r_c, \tag{2.1.6}$$

where p_L is the liquid pressure on the bubble surface S_B, p_B is the pressure inside the bubble, σ is the surface tension coefficient on the flow domain $\partial\Omega$, and $r_c = \nabla \cdot \boldsymbol{n}$ is the mean curvature of the bubble surface.

The momentum conservation considering the irrotationality and incompressibility pro-

vides the Bernoulli equation and reads as follows

$$\frac{\partial \varphi}{\partial t} + \frac{1}{2}\left|\nabla \varphi\right|^2 + gz + \frac{p}{\rho_L} = f(t). \tag{2.1.7}$$

Far-field boundary conditions are used to determine the value $f(t)$, for instance, if it is assumed that $\varphi, \psi \to 0$ as $r \to \infty$, then equation (2.1.7) reads $f(t) = p_\infty/\rho_L$, and hence equation (2.1.7) becomes

$$\frac{\partial \varphi}{\partial t} + \frac{1}{2}\left|\nabla \varphi\right|^2 + gz + \frac{p}{\rho_L} = \frac{p_\infty}{\rho_L}. \tag{2.1.8}$$

Bubble Content

The internal bubble pressure p_B requires more deliberation. The basic approach is to presume that the content inside the bubble is uniform and contains either some condensable vapour (as in (Blake and Gibson, 1981)) or non-condensable gas (as in (Best and Kucera, 1992). An appropriate approximation of the condensable vapour contents can be achieved by considering a constant internal pressure inside the bubble. It is due to evaporation of the vapour during the expansion stage, and condensation during the collapse stage (Lee, Klaseboer and Khoo, 2007). The non-condensable gas contents are frequently modelled as an adiabatic ideal gas, as follows

$$p_B = p_v + p_{g0}\left(\frac{V_0}{V}\right)^\kappa, \tag{2.1.9}$$

where V and V_0 are the current and initial volumes of the bubble, respectively, p_v is a constant vapour pressure, and κ is the ratio of specific heats which is taken as 1.4 unless stated otherwise. The bubble oscillation is induced by the presence of these contents during the collapse stage. This is due to the high pressures built up by the internal gas.

The equations are non-dimensionalised by using maximum bubble radius R_m as the length scale and $\Delta p = p_\infty - p_v$ as the pressure scale. We thus introduce the following

dimensionless variables, indicated by asterisks:

$$U_{ref} = \sqrt{\frac{\Delta p}{\rho_L}}, \tag{2.1.10a}$$

$$t^* = \frac{t}{R_m U_{ref}} \tag{2.1.10b}$$

$$\boldsymbol{r}^* = \frac{\boldsymbol{r}}{R_m}, \tag{2.1.10c}$$

$$dS^* = R_m^2 dS, \tag{2.1.10d}$$

$$\varphi^* = \frac{\varphi}{R_m U_{ref}}, \tag{2.1.10e}$$

$$\delta = \sqrt{\frac{\rho g R_m}{\Delta p}}, \tag{2.1.10f}$$

$$\varepsilon = \frac{p_0}{\Delta p}, \tag{2.1.10g}$$

$$W_e = \frac{R_m \Delta p}{\sigma}, \tag{2.1.10h}$$

$$R_e = \frac{R_m \rho U_{ref}}{\nu}, \tag{2.1.10i}$$

where δ, W_e, and R_e are the buoyancy, the Weber number and the Reynolds number, σ is the surface tension (0.072 N/m for pure water) and ν is the kinematic viscosity of water ($1.003 \times 10^{-6}\ m^2/\text{s}$). In general, the other values are taken as $p_\infty = 101$ kPa, $p_v = 2.3$ kPa and $\rho_L = 1000\text{kg m}^{-3}$. Thus we arrive at the following dimensionless boundary conditions

$$\frac{D\boldsymbol{r}^*}{Dt^*} = \nabla\varphi^*, \quad \boldsymbol{r}^* \in S_B, \tag{2.1.11}$$

$$\frac{D\varphi^*}{Dt^*} = 1 + \frac{1}{2}\left|\nabla\varphi^*\right|^2 - \delta^2 z^* - \varepsilon\Big(\frac{V_0}{V}\Big)^\kappa. \tag{2.1.12}$$

Dimensionless variables are used in the remaining text (without asterisks) unless stated otherwise.

2.2 Boundary integral method (BIM)

Boundary integral equations are the key point in partial differential equations for the analysis of boundary value problems. The term "boundary integral method" (BIM) based

on the potential flow theory is well developed for the simulation of bubble dynamics. BIM generally refers to any method to approximate the numerical solution of these boundary integral equations.

The BIM has emerged as a compelling alternative to finite element methods FEM, mainly to obtain a better accuracy for some exceptional cases, for instance, for problems arising from an infinite domain or problems with stress concentration. The beginning of implementing the numerical BIM can be traced back to the 1960s since the development of electronic devices and computers (López-Villa, Zamudio and Medina, 2014). In the late 1970s, the complete development of the numerical technique is identified as the boundary element or boundary integral method. In the last three decades, under the hypothesis of an inviscid incompressible fluid, the BIM has been developed successfully for simulating the bubble dynamics (Fu and Popov, 2011). As of yet, for the case of non-spherical bubble collapse, there are no suitable methods to predict the energy loss of the bubble system. Regarding the energy lose for a bubble system, Cole and Weller (1948) suggested that the mechanism by which energy can be dissipated: the compressibility of the water, by which energy is radiated as a wave and ultimately dissipated as heat as the wave passes to an infinite distance, . It has been confirmed by numerous experiments on bubble dynamics that there is an emission of steep pressure waves at bubble inception and at the end of collapse, which consequently dampen the bubble oscillation due to energy loss (Lauterborn and Vogel, 2013; Wang, 2016). Lee, Klaseboer and Khoo (2007) improved the BIM method by eliminating a part of the potential energy on the bubble at the end of the first cycle of oscillation. After three decades of development, an advantageous application of BIM has been found concerning the numerical solution of the partial differential equations. With the improvement of computational technology, numerical studies have been achieved for the understanding of bubble dynamics. Compared with recent numerical domain methods, for example, the Finite Difference Method (FDM) and the Finite Element Method (FEM), the BIM is distinguished as a boundary method.

Advantages of the BIM

The numerical BIM method is superior to the other numerical methods and has several advantages, given as follows:

- The methodology formulation of BIM, as boundary integral equations, require describing problems only by equations with known and unknown boundary states.
- Consequently, the discretizations are performed on the boundaries of the domain to reduce spatial dimension. For instance, in the 2D case, the boundaries only consist of simple curves and in the 3D case, only surfaces.
- Less data is required to get efficient results. Also, there is less unwanted information compared with FEM. Therefore, it explains why such a technique is not costly.
- It is well-suited to problems of open domains (Mushtaq, Shah and Muhammad, 2010).
- A high convergence rate can be accomplished in the approximation to the solution in the interior of the domain. Moreover, the same percentage of convergence perseveres for all derivatives of any order of the solution in the domain (Sandip, Anil and ingh, 2017).
- Due to the initial and boundary conditions, we may obtain a unique solution. Therefore, at any vertices, the value of the function can be evaluated as a contribution to the boundary values.
- The mesh generation is more straightforward compared with the other numerical methods.

Disadvantages of the BIM

The mathematics used in BIM formulation may seem unfamiliar to non-mathematicians. However, many FEM numerical procedures, such as numerical integration, surface in-

terpolation and dealing with the boundary conditions, are directly applicable to BIM solutions. Also,

- Rotational flows may not be simulated.
- The obtained matrices in BIM are asymmetric and fully populated such that they are expensive to solve.
- Different boundary integral equations exist for a certain boundary element method, and for each of them, several approximation methods are provided. Thus plenty of mathematical analysis is required to handle a specific problem. Although the analysis of BIM has been an active area of research in the past decade, it is still not complete and the error estimation is not available for several widely used methods.
- Mathematically, the bulk of the available codes are in an experimental state, and there might exist problems of reliability (Mohamed, 2013).
- Boundary integral equations are generally of the first kind Fredholm integral equations which include singular kernels. If the singularities are not integrable, one has to regularize the integrals which are then defined in a distributional sense.
- For non-smooth surfaces or surfaces with edges and corners, the solution of the boundary value problem has singularities at the boundary. Similarly, in mixed boundary value problems singularities occur due to discontinuity in the boundary conditions.

2.3 Numerical modelling

2.3.1 Boundaries Discretization

The numerical model starts by discretizing the bubble and the rigid boundaries into M small triangular elements. The mesh of an initially spherical bubble starts with a regular

icosahedron 20-sided shape which has 12 vertices (see figure 2.2). To create a sphere with a triangular grid, the initial mesh is enhanced by subdividing each triangle into four triangles and then extrapolating the edges to a unit sphere (Manmi, 2015; Wang, 1998). Figure 2.2 shows the resultant grid up to level 10. Each subdivision or level increases the grid size by a factor of 4. The number of the triangles and vertices at n^{th} level is $20n^2$ and $10n^2 + 2$. The levels 8-12 triangulation have been used in this work. For the other surfaces, such as rigid walls, or more complex boundaries, the three-dimensional finite element mesh generator Gmsh is utilized.

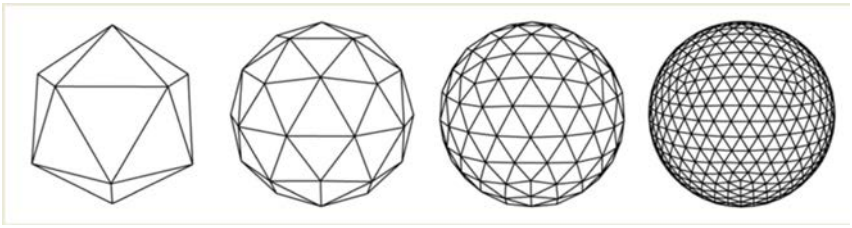

Figure 2.2: A diagram of the initial icosahedron and the the resultant grid up to level 4.

Consider the BIM (2.1.1) and re-order it as follows

$$c(\boldsymbol{r},t)\varphi(\boldsymbol{r},t) + \int_S K(\boldsymbol{r},\boldsymbol{q})\varphi(\boldsymbol{q},t)\ dS(\boldsymbol{q}) = \int_S L(\boldsymbol{r},\boldsymbol{q})\psi(\boldsymbol{q},t)\ dS(\boldsymbol{q}), \tag{2.3.1}$$

where K and L are two kernel functions defined as follows

$$K(\boldsymbol{r},\boldsymbol{q}) = \frac{\partial}{\partial n}\Big(\frac{1}{|\boldsymbol{r}-\boldsymbol{q}|}\Big), \quad \text{and} \tag{2.3.2}$$

$$L(\boldsymbol{r},\boldsymbol{q}) = \frac{1}{|\boldsymbol{r}-\boldsymbol{q}|}. \tag{2.3.3}$$

Each integral in (2.3.1), can be expressed as the summation of the surface integral over all the boundary elements. In our code, the global coordinate system, $Oxyz$, is transformed into a local one, (ξ,η) as depicted in figure 2.3. On each triangular element m, the interpolation scheme is used for the position vector $\boldsymbol{q}$, potential φ and the normal velocity ψ, as follows

$$\boldsymbol{q}_m = (1-\xi-\eta)\boldsymbol{q}_m^1 + \xi\boldsymbol{q}_m^2 + \eta\boldsymbol{q}_m^3, \tag{2.3.4a}$$

$$\varphi_m = (1-\xi-\eta)\varphi_m^1 + \xi\varphi_m^2 + \eta\varphi_m^3, \tag{2.3.4b}$$

$$\psi_m = (1-\xi-\eta)\psi_m^1 + \xi\psi_m^2 + \eta\psi_m^3. \tag{2.3.4c}$$

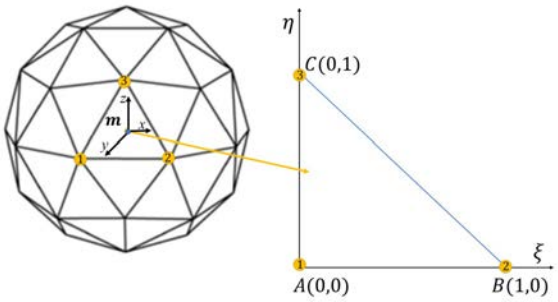

Figure 2.3: Normalised coordinate system (ξ, η) on the triangle $\triangle_m$:ABC.

where the superscripts $1, 2$, and 3 represent the three vertices A, B and C on the element m as shown in figure 2.3. Moreover, the surface integral over all the elements in the local coordinate system (ξ, η) is as follows

$$\iint_{\triangle_m} dS(\boldsymbol{q}) = \int_0^1 \int_0^{1-\eta} J_m d\xi d\eta, \tag{2.3.5}$$

where $J_m = \left|(\boldsymbol{q}_m^1 - \boldsymbol{q}_m^2) \times (\boldsymbol{q}_m^1 - \boldsymbol{q}_m^3)\right|$ is the transformation Jacobian from the global coordinate system to the local one for the element m. Therefore, the integrals in (2.3.1) can be discretized as follows

$$\begin{aligned} c(\boldsymbol{r}^i, t)\varphi(\boldsymbol{r}^i, t) + \sum_{m=1}^{M}\sum_{k=1}^{3} \varphi_m^k(\boldsymbol{r}^i, t) \int_0^1 \int_0^{1-\eta} K_m^i f_k J_m d\xi d\eta \\ = \sum_{m=1}^{M}\sum_{k=1}^{3} \psi_m^k(\boldsymbol{r}^i, t) \int_0^1 \int_0^{1-\eta} L_m^i f_k J_m d\xi d\eta, \end{aligned} \tag{2.3.6}$$

for the superscripts $i = 1, 2, \cdots, N$ refer to the evaluations according to the node i, where N and M are the total number of vertices and triangles on the boundaries $\partial\Omega$, respectively

and functions f_k are

$$f_1(\xi,\eta) = 1-\xi-\eta, \quad f_2(\xi,\eta) = \xi \quad \text{and} \quad f_3(\xi,\eta) = \eta. \tag{2.3.7}$$

The two kernels, $K^i_m = K_m(\boldsymbol{r}^i, \boldsymbol{q})$ and $L^i_m = L_m(\boldsymbol{r}^i, \boldsymbol{q})$, in the local coordinate system are updated as follows

$$K^i_m(\xi,\eta) = -\frac{d^i_m}{(\omega^i_m)^3}, \tag{2.3.8}$$

$$L^i_m(\xi,\eta) = \frac{1}{\omega^i_m}, \tag{2.3.9}$$

where

$$\omega^i_m = \sqrt{e_1\xi^2 + e_2\eta^2 + e_3\xi\eta + e_4\xi + e_5\eta + e_6}\ , \tag{2.3.10a}$$

$$d^i_m = \boldsymbol{n}_m \cdot (\boldsymbol{r}^i - \boldsymbol{q}^1_m), \tag{2.3.10b}$$

$$e_1 = \left|\boldsymbol{q}^1_m - \boldsymbol{q}^2_m\right|^2, \quad e_2 = \left|\boldsymbol{q}^1_m - \boldsymbol{q}_m{}^3\right|^2, \tag{2.3.10c}$$

$$e_3 = (\boldsymbol{q}^1_m - \boldsymbol{q}^2_m).(\boldsymbol{q}^1_m - \boldsymbol{q}^3_m), \quad e_4 = (\boldsymbol{q}^1_m - \boldsymbol{q}^2_m)\cdot(\boldsymbol{r}^i - \boldsymbol{q}^1_m), \tag{2.3.10d}$$

$$e_5 = (\boldsymbol{q}^1_m - \boldsymbol{q}^3_m)\cdot(\boldsymbol{r}^i - \boldsymbol{q}^1_m), \quad e_6 = \left|\boldsymbol{r}^i - \boldsymbol{q}^1_m\right|^2, \tag{2.3.10e}$$

in which $\boldsymbol{n}_m$ is the unit normal of the element m. Hence, equation (2.3.6) reads more simply as

$$c^i\varphi^i + \sum_{m=1}^{M}\sum_{k=1}^{3} b^i_{m,k}\varphi^i_{m,k} = \sum_{m=1}^{M}\sum_{k=1}^{3} a^i_{m,k}\psi^i_{m,k}, \quad i = 1,2,...,N \tag{2.3.11}$$

with

$$a^i_{m,k} = \int_0^1\int_0^{1-\eta} L^i_m f_k J_m d\xi d\eta, \tag{2.3.12}$$

$$b^i_{m,k} = \int_0^1\int_0^{1-\eta} K^i_m f_k J_m d\xi d\eta. \tag{2.3.13}$$

Here, $i,j = 1,\cdots,N$ being the index of all the vertices, new influence coefficient matrices A and B are introduced as follows

$$A_{i,j} = \sum_{m=1}^{M} \sum_{k=1}^{3} \delta_{kj} a^i_{m,k}, \tag{2.3.14}$$

$$B_{i,j} = \sum_{m=1}^{M} \sum_{k=1}^{3} \delta_{kj} b^i_{m,k}, \tag{2.3.15}$$

in which the condition δ_{kj} is a Dirac delta function and $\delta_{kj} = 1$ when node k in the element m and node j in the domain coincide, otherwise $\delta_{kj} = 0$. In a similar way, both φ^i and $\varphi^i_{m,k}$ are two different notations for the same velocity potential. After performing the integrals using all the vertices i, the above equations can be expressed in the matrix form as follows

$$\mathbf{HX} = \mathbf{GY}, \tag{2.3.16}$$

with

$$H_{i,j} = \begin{cases} A_{i,j} : & \text{vertex } j \text{ is on } S_B, \\ -B_{i,j} : & \text{vertex } j \text{ is on } S_R, \end{cases} \tag{2.3.17}$$

and

$$G_{i,j} = \begin{cases} B_{i,j} : & \text{vertex } j \text{ is on } S_B, \\ -A_{i,j} : & \text{vertex } j \text{ is on } S_R, \end{cases} \tag{2.3.18}$$

in which S_B and S_R on the bubble surface and the surface of the rigid boundaries. Finally, the following are going to be determined

$$X_i = \begin{cases} \psi_i : & \text{vertex } i \text{ is on } S_B, \\ \varphi_i : & \text{vertex } i \text{ is on } S_R, \end{cases} \tag{2.3.19}$$

while the following are known:

$$Y_i = \begin{cases} \varphi_i : & \text{vertex } i \text{ is on } S_B, \\ \psi_i : & \text{vertex } i \text{ is on } S_R. \end{cases} \tag{2.3.20}$$

Calculating the influence of coefficient matrices, A, and B is the most challenging part

in the coding. Also, most of the CPU times goes into calculating them (Li et al., 2012; Wang, 1998). However, when the calculation domain size, N, is large, solving the linear systems (2.3.16) requires longer time compared with the influence matrices. To deal with this, the most advanced Linear Algebra Package, LAPACK, is used in order to save the CPU time and to solve the linear systems more accurately parallelly. The seven-point Gaussian quadrature is used to perform the integration in the off-diagonal elements of the matrix of influence coefficients. However, singularities appear on the diagonal elements of B and A. The polar coordinate transformation can be used to solve the singularities of the A matrix due to a weak singularity for the diagonal elements (Li et al., 2012; Wilkerson, 1992). However, the so-called 4π rule is adopted to eliminate the singularity in the diagonal elements of the matrix B. In the mentioned rule, and for a closed surface, the diagonal elements of B are equal to the solid angles as follows

$$B_{ii} = 4\pi - \sum_{\substack{j=1,\\ i\neq j}}^{N} B_{ij} \quad \text{for } i = 1, ..., N. \tag{2.3.21}$$

Actually, from spherical triangle theory, the solid angle can be calculated analytically (Wang, 2005), as follows

$$c(\boldsymbol{r}^i, t) = \sum_{k=1}^{M^i} \Theta_k^i(t) + (2 - M^i)\pi, \tag{2.3.22}$$

where the superscript i refers to any vertex on the domain surfaces, M^i is the number of the surrounding elements/vertices to that vertex, and $\Theta_k^i(t)$ is the angle between every two connected surrounding elements to the vertex i at time t as shown in figure 2.4.

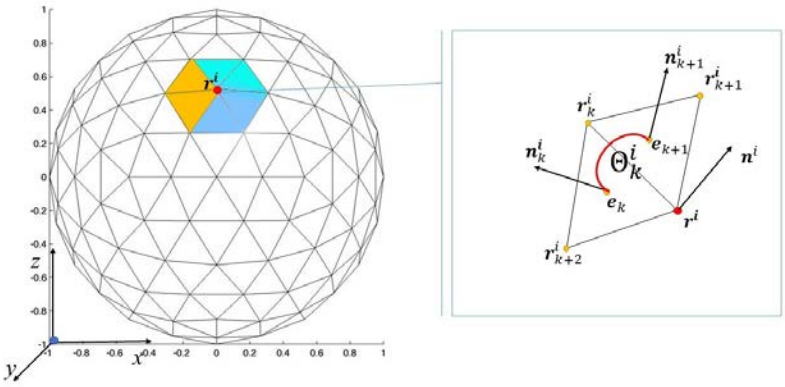

Figure 2.4: Sketch of the surrounding elements to a control point $\boldsymbol{r}^i_k$, outward normal $\boldsymbol{n}^i$, $\boldsymbol{n}^i_k$ and the angle Θ^i_k between any two connected triangular elements in a triangular mesh.

2.3.2 Normal vector, Mean Curvature, Tangential Velocity and bubble centroid Calculations

Accurately determining the normal $\boldsymbol{n}^i$ on a vertex i in triangulated surfaces is of great importance to the accuracy of the BIM computation, as well as smoothing techniques. However, there is no suitable method to evaluate the normal vectors on the vertices of the non-flat meshed boundaries due to the non-uniqueness of that normal. Here, we implement the method suggested for computing the mean curvature vector, to the problem of accurate computing vertex normal.

Initially, we estimate the normal vector $\boldsymbol{N}^i_0$ on the vertex $\boldsymbol{r}^i$ using the weighted average of the normal vectors of the surrounding elements. Thus

$$\boldsymbol{N}^i_0 = \sum_{k=1}^{M^i} W_k \boldsymbol{n}^i_k, \tag{2.3.23}$$

where M^i is the number of the surrounding triangles/vertices to the vertex $\boldsymbol{r}^i$, $\boldsymbol{n}^i_k$ and w_k are the normal vector and weighted coefficient for surrounding elements. Various W_k can be taken regarding the type of the simulation. Here, a spline function is chosen as the

weighted following (Han et al., 2016; Wang, 2005) as follows

$$W_k = \begin{cases} \frac{2}{3} - 4\overline{d}^2 + 4\overline{d}^3, & \overline{d} \leqslant \frac{1}{2} \\ \frac{4}{3} - 4\overline{d} + 4\overline{d}^2 - \frac{4}{3}\overline{d}^3 & \frac{1}{2} < \overline{d} \leqslant 1, \\ 0 & \overline{d} > 1 \end{cases} \tag{2.3.24}$$

where $\overline{d} = (|\boldsymbol{r}_k^i - \boldsymbol{r}^i|/2d)$ is the ratio of the distance from vertex $\boldsymbol{r}^i$ to the surrounding vertices, d is the average distance from the neighbouring vertices $\boldsymbol{r}_k^i$ to the vertex $\boldsymbol{r}^i$, and M^i is the number of the surrounding elements to the vertex $\boldsymbol{r}^i$ as shown in figure 2.4.

The estimated normal vector can be used to interpolate the patch of the bubble surface using a moving least square method following Han et al. (2016); Wang (2005); Zhang et al. (2001). A local Cartesian coordinate system, $Oxyz$ is introduced, with its origin O at the point considered, and its z-axis along the normal direction $\boldsymbol{n}^i$. A second-order polynomial is implemented to interpolate the bubble surface, or any other smooth surface in the model, as follows,

$$Z = F(X, Y) = a_1 + a_2X + a_3Y + a_4X^2 + a_5XY + a_6Y^2. \tag{2.3.25}$$

The weighted least squares method with the error function is defined as follows:

$$\Psi(a_1, a_2, a_3, a_4, a_5, a_6) = \sum_{k=1}^{M^i} W_k[F(X_k, Y_k) - Z_k]^2. \tag{2.3.26}$$

To minimise the error, the partial derivative of the function Ψ is set to be zero for a_j to calculate the coefficients a_j

$$\frac{\partial \Psi}{\partial a_j} = 0, \quad \text{for } j = 1, 2, ..., 6. \tag{2.3.27}$$

Rearranging Eq. (2.3.27) yields

$$\sum_{j=1}^{6} \mathcal{A}_{ij} a_j = \mathcal{B}_i, \quad \text{for } i = 1, 2, ..., 6, \tag{2.3.28}$$

where $\mathcal{A}_{ij}$ and $\mathcal{B}_i$ are given in terms of W_k and (X_k, Y_k, Z_k),

$$\mathcal{A}_{ij} = \sum_{k=1}^{M^i} W_k \mathcal{B}_{kj} \mathcal{B}_{ki}, \quad \mathcal{B}_i = \sum_{k=1}^{M^i} W_k Z_k \mathcal{B}_{ki}, \tag{2.3.29}$$

in which

$$\mathcal{B}_{k1} = 1,\ \mathcal{B}_{k2} = X_k,\ \mathcal{B}_{k3} = Y_k,\ \mathcal{B}_{k4} = X_k^2,\ \mathcal{B}_{k5} = X_k Y_k,\ \mathcal{B}_{k6} = Y_k^2. \tag{2.3.30}$$

Thus, a more accurate normal vector N^i can be obtained as follows

$$\boldsymbol{N_l^i} = \frac{\nabla f}{\left|\nabla f\right|} = \pm \frac{(a_2, a_3, -1)}{\sqrt{a_2^2 + a_3^2 + 1}}, \tag{2.3.31}$$

where the sign can be chosen such that $(\boldsymbol{N}_l^i \cdot \boldsymbol{N}_{l-1}^i) > 0$, l is the iteration index and the iteration stops when $||\boldsymbol{N}_l^i - \boldsymbol{N}_{l-1}^i|| < \varepsilon$, where ε is a constant and one can choose $\varepsilon = 0.001$. If the iteration condition did not satisfy assign $\boldsymbol{N}_{l-1}^i = \boldsymbol{N}_l^i$ and repeat the procedure again. Moreover, the mean curvature for the surface $f(X, Y, Z) = F(X, Y) - Z = 0$ is given by

$$\nabla \cdot \boldsymbol{N}_l^i = -\frac{a_5 + a_6 + a_6 a_2^2 + a_5 a_3^2 - a_2 a_3 a_4}{(1 + a_2^2 + a_3^2)^{3/2}}. \tag{2.3.32}$$

In the same manner, the potential interpolation has been used to compute the tangential velocity at the considered vertex as follows

$$\boldsymbol{v}_\tau = b_2 \nabla X(x, y, z) + b_3 \nabla Y(x, y, z), \tag{2.3.33}$$

where b_2 and b_3 are the coefficients of an interpolated potential function of the φ, $X(x, y, z)$

and $Y(x, y, z)$ are obtained from the transformation of the global coordinates into the local coordinate system.

In addition, as the bubble (3D-structures) surface is made up of tetrahedron elements, the bubble centroid coordinates $\boldsymbol{R}_c = (x_c, y_c, z_c)$ can be calculated as follows

$$\boldsymbol{R}_c = \frac{1}{V}\int_V \boldsymbol{R}\, dV \approx \frac{\sum_{k=1}^{M} \boldsymbol{R}_k V_k}{\sum_{k=1}^{M} V_k}, \tag{2.3.34}$$

where V_k is the volume of each tetrahedron, $\boldsymbol{R}_k$ is the centroid of the k^{th} tetrahedron having the vertices $\boldsymbol{E}_j = (x_j, y_j, z_j)$, for $j = 1, \cdots, 4$.

2.3.3 Lagrangian time integration

Whenever the material velocity on the boundary is known, the velocity potential on the bubble surface, the bubble shape and position at the next time step can be updated by solving the kinematic (2.1.4) and the dynamic (2.1.7) boundary conditions using the second-order predictor-corrector scheme. A non-uniform time step (Δt), for each iteration procedure, is chosen sensibly with the criterion

$$\Delta t = \left[\frac{\Delta\phi}{\max\left|1 + \frac{1}{2}\left|\nabla\varphi(\boldsymbol{r}, t)\right|^2 - \delta^2 z - \varepsilon\left(\frac{V_0}{V}\right)^{\kappa}\right|}\right], \tag{2.3.35}$$

where $\Delta\phi$ is a constant and it can take any values in the range $[0.001, 0.01]$ for studying the accuracy and efficiency of the models.

2.3.4 Kelvin Impulse Calculation

The Kelvin impulse is the global conservation of linear momentum. It was first introduced by Benjamin and Ellis (1966). The Kelvin impulse links the inertia of the linear momentum of a projectile and the cavitation bubble. It can be used to determine some characteristics of the bubble dynamics, such as the direction of the movement of the bub-

ble centroid (Blake, 1988; Blake and Cerone, 1982). The dimensionless Kelvin impulse $\boldsymbol{I}$ of a bubble is defined as

$$\boldsymbol{I} = \int_{S_B} \varphi \boldsymbol{n} dS. \tag{2.3.36}$$

where φ is the potential, S_B is the bubble surface and $\boldsymbol{n}$ is the outward normal to the fluid domain. The Kelvin impulse corresponds to the apparent inertia of the bubble and its direction indicates the directions of the bubble migration and bubble jet (Blake, Leppinen and Wang, 2015; Blake, 1988). Typically, during the latter stages of collapse, the sign of the Kelvin impulse indicates the direction of migration of a cavitational bubble. Accordingly, bubbles are repelled from free surfaces and attracted to rigid boundaries. The magnitude of the Kelvin impulse determines the intensity of the resulting jet as it is maintained as circulation around a toroidal bubble. The closer a bubble is to the boundary, the more powerful the jet is (Blake, 1988).

2.3.5 The viscous model for BIM

The viscous effects in bubble dynamics are not always negligible, for instance, micron-size bubbles and flows with low Reynolds number. In this section, we add the viscous effects into the BIM model based on the viscous potential flow theory through including the normal viscous stress and viscous correction pressure at the bubble surface (Joseph and Wang, 2004; Manmi and Wang, 2017; Wang and Manmi, 2014; Zhang and Ni, 2014). By considering the effects of the surface tension σ and the normal stress τ_n, the internal bubble pressure p_B is associated with the fluid pressure p_L on the bubble surface (Caboussat, 2006; Lamb, 1932). Thus, equation (2.1.6) of the bubble surface can be modified into

$$p_L = p_B - 2\sigma r_c + \tau_n, \tag{2.3.37}$$

when σ is the surface tension coefficient and r_c is the radius of mean curvature of the bubble surface.

On the bubble surface, the tangential stress of the liquid flow might be negligible due

to the relatively lower dynamic viscosity of the gas inside the bubble (Kang and Leal, 1988; Zhang and Ni, 2014). However, due to the irrotationality of the fluid velocity, $\boldsymbol{u}$, the normal viscous stress does not vanish on the bubble surface, and it has the following form

$$\tau_n = 2\mu \ \partial w_n/\partial n \approx 2\mu \ \psi_n \neq 0, \tag{2.3.38}$$

in which $w_n = \boldsymbol{w} \cdot \boldsymbol{n}$ for the total velocity field $\boldsymbol{w} = \nabla\varphi + \boldsymbol{u}$, and $\boldsymbol{u}$ is the rotational velocity field, μ is the dynamic viscosity of the fluid and $\psi_n = \partial^2\varphi/\partial n^2$. In order to deal with this difference, Joseph and Wang (2004) introduced a viscous pressure correction P_{vc} on the bubble surface. They claim that the non-zero shear stress power coincides with the power created by the viscous correction pressure as shown in figure 2.5,

$$-\int_{S_B} P_{vc} \ v_n \ dS = \int_{S_B} \boldsymbol{v} \cdot \boldsymbol{\tau}_s \ dS, \tag{2.3.39}$$

where $v_n = \boldsymbol{v} \cdot \boldsymbol{n}$. Furthermore, they assume that the viscous correction pressure P_{vc} and the normal stress τ_n are proportional for irrotational fluid flow,

$$P_{vc} = -C\tau_n = -2\mu C\psi_n, \tag{2.3.40}$$

where C is a constant. Thus the boundary condition in (2.3.37) becomes

$$p_L = p_B - \sigma r_c + 2\mu(1 + C) \ \psi_n. \tag{2.3.41}$$

To calculate normal stress τ_n, the term $\partial^2\varphi/\partial n^2$ is needed and can be calculated as follows

$$\psi_n = \boldsymbol{n} \cdot \frac{\partial}{\partial n}\nabla\varphi = n_x\psi_x + n_y\psi_y + n_z\psi_z, \tag{2.3.42}$$

where $\psi_x = \partial\varphi_x/\partial n$, since φ satisfies the Laplace's equation and the boundary integration equation (2.1.1). Thus, the quantities φ_x, φ_y and φ_z satisfy Laplace's equation too.

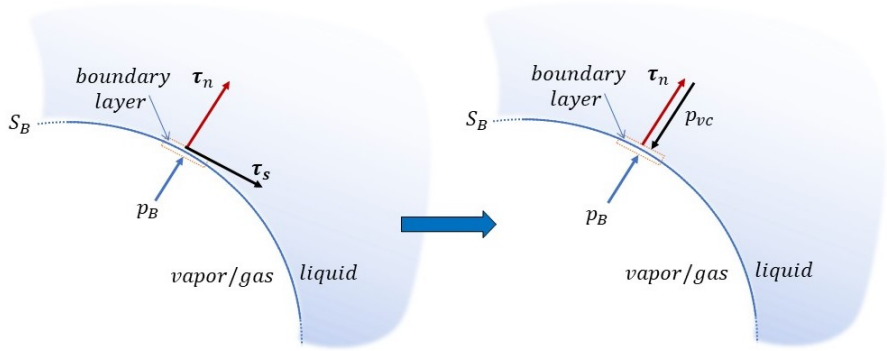

Figure 2.5: A Sketch to balance the non-zero shear stress by implementing viscous correction P_{vc} (Zhang and Ni, 2014)

Consequently, the velocity potential φ in equation (2.1.1) can be replaced by φ_x, φ_y and φ_z to formulate the boundary integral equations such as

$$c(\boldsymbol{r},t)\varphi_x(\boldsymbol{r},t) = \iint_S \Big[\psi_x(\boldsymbol{q},t)G(\boldsymbol{r},\boldsymbol{q}) - \varphi_x(\boldsymbol{q},t)\frac{\partial G(\boldsymbol{r},\boldsymbol{q})}{\partial n}\Big]dS(\boldsymbol{q}). \tag{2.3.43}$$

Comparing (2.3.43) and (2.1.1), ψ_x is easily obtained, as φ_x has been obtained on all the surfaces after solving equation (2.1.1). Likewise, ψ_y and ψ_z can be obtained. Consequently, ψ_n on the bubble surface is known and then the normal stress from (2.3.40) is easily obtained. Accordingly, equation (2.3.43) leads to the following system of linear equations in a matrix form

$$[\psi_x]_{N\times 1} = [A_x^{-1}]_{N\times N}[B_x]_{N\times N}[\varphi_x]_{N\times 1}, \tag{2.3.44a}$$

$$[\psi_y]_{N\times 1} = [A_y^{-1}]_{N\times N}[B_y]_{N\times N}[\varphi_y]_{N\times 1}, \tag{2.3.44b}$$

$$[\psi_z]_{N\times 1} = [A_z^{-1}]_{N\times N}[B_z]_{N\times N}[\varphi_z]_{N\times 1}, \tag{2.3.44c}$$

where N represents the total number all the vertices on the bubble surface and the rigid surfaces, A_x, A_y, A_z and B_x, B_y, B_z are the same coefficients of the influence matrices

obtained in (2.3.14) and (2.3.15).

It is inconvenient to calculate $\boldsymbol{\tau}_s$ directly from equation (2.3.39) to obtain P_{vc} or C. Zhang and Ni (2014), in order to achieve an indirect formula, introduce the rate of energy dissipation D_e as follows

$$D_e = 2\mu \int_V \nabla \boldsymbol{v} : \nabla \boldsymbol{v} \; dV = \int_{S_B} v_n \tau_n dS + \int_{S_B} \boldsymbol{v}_\tau \cdot \boldsymbol{\tau}_s dS. \tag{2.3.45}$$

Substituting $P_{vc} = -C\tau_n$ and equation (2.3.40) into the above equation yields

$$D_e = (1+C) \int_{S_B} v_n \tau_n dS = 2\mu(1+C) \int_{S_B} \psi \psi_n \; dS. \tag{2.3.46}$$

On the other hand, for irrotational flow, the surface integral can be used to express the rate of energy dissipation D_e

$$D_e = 2\mu \int_{S_B} \left(\varphi_x \psi_x + \varphi_y \psi_y + \varphi_z \psi_z \right) \; dS, \tag{2.3.47}$$

where $\psi_x = \partial \varphi_x / \partial n$, similarly for the other quantities. Solving equations (2.3.46)-(2.3.47) simultaneously yields

$$C = \frac{\int_{S_B} \left(\varphi_x \psi_x + \varphi_y \psi_y + \varphi_z \psi_z \right) \; dS}{\int_{S_B} \psi \psi_n \; dS} - 1. \tag{2.3.48}$$

A linear interpolation has been used on each triangular element for φ_x, φ_y, φ_z, ψ_x, ψ_y, ψ_z and ψ_n to evaluate the surface integrals in equation (2.3.48). Subsequently, the viscous correction term p_{vc} and the normal stress τ_n can be solved. Accordingly, the weak viscous effect is considered at high Reynolds number. Moreover, the modified Bernoulli equation regarding the viscous pressure correction is as follows

$$\frac{\partial \varphi}{\partial t} + \frac{1}{2} \left| \nabla \varphi \right|^2 + gz + \frac{p - P_{vc}}{\rho} = \frac{p_\infty}{\rho}, \tag{2.3.49}$$

where p_{vc} is pressure correction. Substituting (2.3.41) into (2.3.49), leads to a complete fully non-linear dynamic boundary condition on the bubble surface,

$$\frac{D\varphi}{Dt} = \frac{1}{2}\left|\nabla\varphi\right|^2 + 2\sigma r_c - 2\mu\psi_n - gz - \frac{p_B - P_{vc} - p_\infty}{\rho}. \tag{2.3.50}$$

Using the same scales as (2.1.10),the non-dimensional form of (2.3.50) reads as follows

$$\frac{D\varphi^*}{Dt^*} = 1 + \frac{1}{2}\left|\nabla\varphi^*\right|^2 - \delta^2 z^* - \varepsilon\Big(\frac{V_0}{V}\Big)^\kappa + 2\frac{r_c}{W_e} - 2\frac{(1+C)}{R_e}\psi_n^*, \tag{2.3.51}$$

where $R_e = R_m\sqrt{\rho\Delta p/\mu}$ is Reynolds number and $W_e = \Delta p R_m/\sigma$ is the Weber number. $\varepsilon = p_0/\Delta p$ is the dimensionless initial pressure of the bubble gas.

For a bubble subject to an ultrasonic wave, an incident wave should be incorporated into the model by adding the acoustic pressure in the equation (2.3.51) (Wang and Manmi, 2014). Ultrasonic wave effects can cause non-spherical collapse and formation of bubble jetting (Rosselló et al., 2018).

2.4 Optimization techniques and mesh density control

It has commonly been assumed that grid smoothness is a post-processing procedure designed to improve mesh quality. In contrast to the common description of mesh quality, which generally considers the particular criteria of each element, such as; skewness, aspect ratio, maximum corner angle, orthogonal quality, etc., smoothness of a mesh has a global meaning. Thus, these two separated measures, the mesh quality, and the mesh smoothness may be inconsistent for some cases. Certainly, a smoother mesh does not necessarily imply better mesh quality (Arabi, Camarero and Guibault, 2014; Falsafioon et al., 2014). Subsequently, improving the mesh quality may lead to losing some numerical accuracy, such as a change in volume and the shape of the actual mesh. Therefore, choosing an ideal smoothing is often challenging.

In this section, we introduce two smoothing techniques to improve the mesh quality and to reduce the noise reduction on the surface. When a bubble is close to rigid boundaries, during the bubbles expansion and the early stage of the collapse, the mesh vertices gather to the jet zone, as well as form some noise on the bubble surface during the collapse stage. For the former concern, during the expansion stage until the beginning of the jet formation, we use a modified elastic mesh technique (MEMT) which is based on the elastic mesh technique (EMT) to reduce the mesh density in the jet zone. However, for the latter problem, which happens after the jet formation in the collapse stage, we use the volume preserve smoothing technique (VPST). This technique is based on the Laplacian smoothing technique (LST), reducing the noise as well as preserving the volume of the bubble.

2.4.1 Modified elastic mesh technique (MEMT)

Using the material velocity to update the bubble surface in the BIM leads to a poor mesh quality, decreases the numerical stability, and the accuracy throughout the bubble oscillation, particularly during the jet development (Zhang and Liu, 2015). Subsequently, to reduce this instability, a density potential method may be used, which is based on the Elastic mesh technique of (Wang and Khoo, 2004; Wang, Khoo and Yeo, 2003). In the mentioned technique, it is assumed that each segment on the mesh surface has an elastic ribbon property. Thus, to have an optimum mesh, it is obligatory to minimize the stored total energy in each segment. For this, the material velocity on the bubble surface, for the current time step, can be replaced by any velocity with the same normal component to the bubble surface but identical to the material velocity. The modification on the elastic mesh technique (EMT) can be done by replacing the weight function $f(\ell)$, in Manmi (2015) and Wang, Khoo and Yeo (2003), by another weight function to get better results.

In this section, we modify the EMT technique based on the density potential method DPM described in (Li et al., 2019; Zhang and Liu, 2015) as follows.

Consider the i^{th} vertex on the bubble surface which is located in $\boldsymbol{r}_i$ with current

velocity $\boldsymbol{v}_i$, $i = 1, , N_b$), where N_b is the total number of the vertices of the bubble surface. For the next time step $t + \Delta t$, the i^{th} vertex will be located at $\boldsymbol{r}_{i+1} = \boldsymbol{r}_i + \Delta t \boldsymbol{v}_i$. The segment length for the next time step will be $\boldsymbol{r}_{ij} + \Delta t \boldsymbol{v}_{ij}$, where i and j are the label of the vertices connecting each segment, $\boldsymbol{r}_{ij} = \boldsymbol{r}_i - \boldsymbol{r}_j$, and $\boldsymbol{v}_{ij} = \boldsymbol{v}_i - \boldsymbol{v}_j$. Here, a density potential function $\Gamma(\varphi)$ is introduced for node i as follows

$$\Gamma(\varphi_i) = \frac{\Theta(\varphi_i)}{m_b} \sum_{j=1}^{m_b} A_{i,j}, \tag{2.4.1}$$

where $A_{i,j}$ and m_b are the area of the j^{th} element and the number of elements surround the vertex i, respectively, and Θ is the normalization function for the velocity potential and one can define it as follows

$$\Theta(\varphi_i) = \frac{\varphi_i}{\max(\varphi_j)}, \ i = 1, \cdots, N_b, \tag{2.4.2}$$

where j includes all the vertices surrounded the vertex i. Suppose the velocity at k^{th} iteration is $\boldsymbol{v}_i^k$, consequently the velocity in the $(k+1)^{th}$ iteration can be found using the following scheme

$$\boldsymbol{v}_i^{k+1} = \psi_i^k \boldsymbol{n}_i + P\left[\frac{\sum_{j=1}^{m_b} \Gamma(\varphi_i^k)(\boldsymbol{r}_{i,j} + \Delta t \boldsymbol{v}_j^k)}{\Delta t \sum_{j}^{m_b} \Gamma(\varphi_i^k)}\right], \tag{2.4.3}$$

where ψ_i is prescribed normal velocity at vertex i, P is an operator to project a vector on to the tangential plane for the i^{th} vertex, as follows

$$P(\boldsymbol{v}) = \boldsymbol{v} - (\boldsymbol{v} \cdot \boldsymbol{n}_i)\boldsymbol{n}. \tag{2.4.4}$$

We implement a hybrid-approach for MEMT as follows,

$$\boldsymbol{v}_i^{hybrid} = W \boldsymbol{v}_i + (1 - W)\boldsymbol{v}_i^s, \tag{2.4.5}$$

where $W \in (0,1)$ is the weight parameter chosen based on the simulation case. The optimum prescribed velocity $\boldsymbol{v}_i^s$ is obtained from equation (2.4.3) after finite number of iterations which can be used to update the bubble surface and the velocity potential for the next time step as follows

$$\frac{\delta \boldsymbol{r}}{\delta t} = \boldsymbol{v}_i^s, \tag{2.4.6a}$$

$$\begin{aligned} \frac{\delta \varphi}{\delta t} &= \frac{\partial \varphi}{\partial t} + \boldsymbol{v}_i^s.\nabla\varphi \\ &= (\boldsymbol{v}_i^s - \boldsymbol{v}_i).\nabla\varphi + \frac{D\varphi}{Dt}. \end{aligned} \tag{2.4.6b}$$

2.4.2 Volume preserving smoothing technique (VPST)

The volume-preserving smoothing (VPST) is adopted on triangular meshes over three-dimensional surfaces. In this approach, the standard Lagrangian smoothing technique (LST) is modified by using positive and negative weights in sequential cycles of the smoothing. Laplacian smoothing is an ordinarily used method to improve the quality of a mesh. In the Lagrangian approach, the material velocities at the vertices are used to update the bubble surface. This may lead to poor-quality mesh for a non-spherical bubble motion (Rypl and Nerad, 2016).

In the past, different approaches were developed to reduce the noise of a surface mesh and prevent the shrinking of its volume. A vertex balance procedure has been used based on the local volume control in (Kuprat et al., 2001; Liu et al., 2002; Sousa et al., 2007). Garimella, Shashkov and Knupp (2004) used a non-linear optimisation technique together with suitable objective functions to re-position vertices to improve the quality of the surface meshes. Based on the approach of (Taubin, 1995), the volume-preserving smoothing technique VPST is developed by (Rypl and Nerad, 2016). However, the weights for smoothing sub-cycles, corresponding to shrinkage and expansion phases, are derived differently. Contrary to TauTaubin (1995), where they determined the weights by spectral analysis using the Fourier transform, Rypl and Nerad (2016) used a "do not

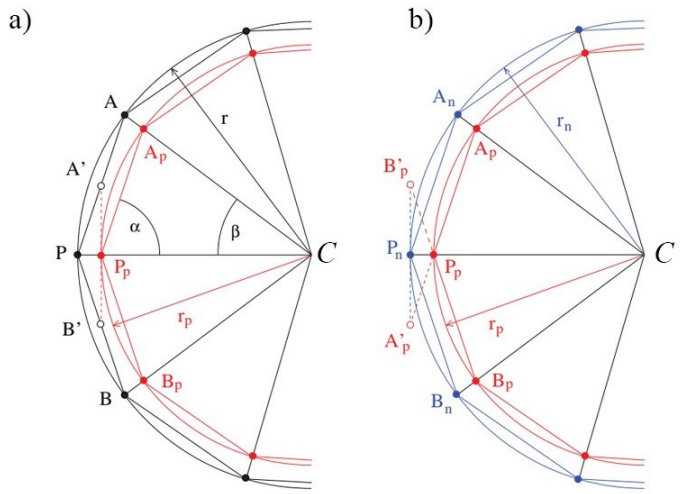

Figure 2.6: Schematic of the volume preserving smoothing showing sub-cycles of (a) the shrinkage sub-cycle (even smoothing cycles using positive weight ζ) and (b) the expansion sub-cycle (odd smoothing cycle using negative weight χ).

harm" concept. They used different weights for each of the shrinking and expansion cycles.

The idea behind the "do not harm" concept smoothing technique is to bring the vertices on the optimal mesh back to their original location. To start, we consider the first two successive cycles of a normal polygon centred at C with radius r as shown in figure 2.6. In the first cycle (the shrinking cycle) each vertex is re-positioned by using a weighted average of the vertex itself with all the neighbouring vertices as shown in figure 2.6(a). For instance, for a particular vertex, $\boldsymbol{P}$, in the first smoothing cycle, the new location for the position vector of the vertex $\boldsymbol{P}$ is given by

$$\begin{aligned}\boldsymbol{P}_p &= \frac{1}{2}\Big(\boldsymbol{A}' + \boldsymbol{B}'\Big) \\ &= \frac{1}{2}\Big(\Big[(1-\lambda_p)\boldsymbol{P} + \lambda_p \boldsymbol{A}\Big] + \Big[(1-\lambda_p)\boldsymbol{P} + \zeta \boldsymbol{B}\Big]\Big) \\ &= (1-\lambda_p)\,\boldsymbol{P} + \frac{\lambda_p}{2}\,(\boldsymbol{A}+\boldsymbol{B})\,, \end{aligned} \tag{2.4.7}$$

where $\lambda_p \in (0,1)$ is a positive weight, and the index p refers to re-positioned vertices. Due to fixed smoothing weight, λ_p, for all the vertices, all re-positioned vertices on the

new polygon lie on a circle cantered at C but with radius r_P. Since λ_p is positive, the shrinking of the initial polygon is obvious as shown in figure 2.6(a). The new polygon has a smaller radius compared to the initial polygon because the smoothing weight, λ_p, is positive. Next, to enforce its expansion, a negative smoothing weight, λ_n, is used to perform the second smoothing cycle. During the second cycle, the vertex $\boldsymbol{P}_p$ moves to a new location $\boldsymbol{P}_n$, see figure 2.6(b), as follows

$$\begin{aligned}\boldsymbol{P}_n &= \frac{1}{2}\Big(\boldsymbol{A}'_p + \boldsymbol{B}'_p\Big) \\ &= \frac{1}{2}\Big(\Big[(1-\lambda_n)\boldsymbol{P}_p + \lambda_n \boldsymbol{A}_p\Big] + \Big[(1-\lambda_n)\boldsymbol{P}_p + \lambda_n \boldsymbol{B}_p\Big]\Big) \\ &= (1-\lambda_n)\,\boldsymbol{P}_p + \frac{\lambda_n}{2}\,(\boldsymbol{A}_p + \boldsymbol{B}_p)\,, \end{aligned} \tag{2.4.8}$$

where subscript n refers to re-positioned vertices using a negative weight. After this stage all the vertices lie on a circle with radius r_n. As described before, the main goal of this smoothing technique is to maintain the volume of the geometry. Therefore, we have to choose a suitable smoothing weight, λ_p and λ_n that satisfies the following relationships

$$\boldsymbol{r} - \boldsymbol{r}_p = \lambda_p\,(\boldsymbol{r} - \boldsymbol{r}\cos\beta)\,, \tag{2.4.9a}$$

$$\boldsymbol{r}_p - \boldsymbol{r}_n = \lambda_n\,(\boldsymbol{r}_p - \boldsymbol{r}_p\cos\beta)\,. \tag{2.4.9b}$$

By adding the last two equations and contending $\boldsymbol{r} = \boldsymbol{r}_n$, one can obtain the relation

$$(\lambda_p \boldsymbol{r} + \lambda_n \boldsymbol{r}_p)\,(1-\cos\beta) = 0. \tag{2.4.10}$$

For $\beta > 0$, $1 - \cos\beta \neq 0$ and we have

$$\frac{r}{r_p} = -\frac{\lambda_p}{\lambda_n}. \tag{2.4.11}$$

The last equation verifies that $|\lambda_p| > \lambda_n > 0$. Substituting equations (2.4.9) into (2.4.11)

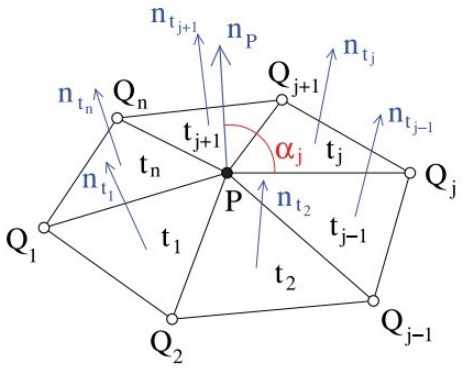

Figure 2.7: Geometrical setup for the evaluation of smoothing weights for inner vertex $\boldsymbol{P}$ of a surface mesh.

yields

$$\frac{1}{1-\lambda_p\,(1-\cos\beta)} = -\frac{\lambda_n}{\lambda_p}. \tag{2.4.12}$$

Finally, and since the triangle $\triangle(P_pSA_p)$ is isosceles triangle, we can consider $1-\cos\beta = 2\cos^2\alpha$, thus

$$\lambda_n = \frac{\lambda_p}{2\lambda_p\beta_1 - 1}, \tag{2.4.13}$$

where $\beta_1 = \sum_j \cos^2\alpha_j/m_b$, for $j = 1,\cdots,m_b$, and m_b is number of surrounding nodes to the node $\boldsymbol{P}$. Here, α_j is the angle between the normal $\boldsymbol{n}_P$ and the segment lines connecting the vertex $\boldsymbol{P}$ with its neighbouring vertex $\boldsymbol{Q}_j$, as shown in figure 2.7. Also, the normal $\boldsymbol{n}_P$ is evaluated from the weighted average of the normal on the surrounding elements to the vertex $\boldsymbol{P}$ just before the odd cycles. The weights here are proportional to the element's area. Besides, the above procedure can be generalised to definite cycles. Setting the subscript 0 to the initial position of vertices on the surface of a closed smooth mesh. The position of vertex $\boldsymbol{P}$ after $k = 1, 2, , N$ smoothing cycles, for even number N, is given by

$$\boldsymbol{P}^k = (1-W)\,\boldsymbol{P}^{k-1} + \frac{W}{M^P}\sum_{j=1}^{M^P}\boldsymbol{Q}_j^{k-1}, \tag{2.4.14}$$

where weight W is equal to λ_p in the odd smoothing cycles and λ_n in the even cycles, M^P is the number of surrounding vertices $\boldsymbol{Q}_j$ to the node $\boldsymbol{P}$. Moreover, the weight λ_n is

calculated from the geometrical setting just before every odd smoothing procedure and greater value for λ_n gives smoother surface. In addition, the same procedure can be used to optimise the noise reduction of the potential φ on the surface of the bubble using the following formula

$$\varphi^k = (1 - W)\,\varphi^{k-1} + \frac{W}{M^P} \sum_{j=1}^{M^P} \varphi_j^{k-1}, \tag{2.4.15}$$

where φ_j^{k-1} is the potential on the vertex $\boldsymbol{Q}_j$ at the smoothing cycle $k-1$ surrounding the vertex $\boldsymbol{P}$.

2.4.3 Comparing the smoothing techniques

Figures 2.8 and 2.9 show comparisons between different smoothing techniques applied to a bubble dynamics near a rigid wall with $\gamma = 1.0, 1.2$, $R_m = 19$mm, $\varepsilon = 200$, and $\delta = 0.04$. Time steps are chosen using $\Delta\varphi = 0.02$ and the smoothing techniques MEMT and VPST are applied every 3 and 10 steps, respectively. Figure 2.8(a) shows the bubble mesh during the collapse without applying any smoothing technique. The code has broken down at that stage due to the instability and noise around the jet area. To remove the noise, we implemented the VPST approach using $W = 0.3$ as shown in figure 2.8(b). The node density around the jet area is higher than the rest. The code broke down again just before the end of the simulation. Figure 2.8(c) used the same approach but with a different time step using $\Delta\varphi = 0.01$. The bubble size became smaller as the mesh density on the surface is not uniform, and the smoothing was applied more due to smaller time steps $\Delta\varphi = 0.01$. Next, the MEMT smoothing teaching is applied every 5 time steps using $\Delta\varphi = 0.03$, see figure 2.8(c). In this case, the node distribution around the bubble surface is more suitable compared to the previous cases. However, the code has broken down at the end due to the noise in the jet area.

Finally, to resolve the aforementioned problems, a combination of the MEMT and VPST techniques is applied as shown in figure 2.8(d). The combination of these two smoothing approaches is giving better mesh quality together with preserving the volume

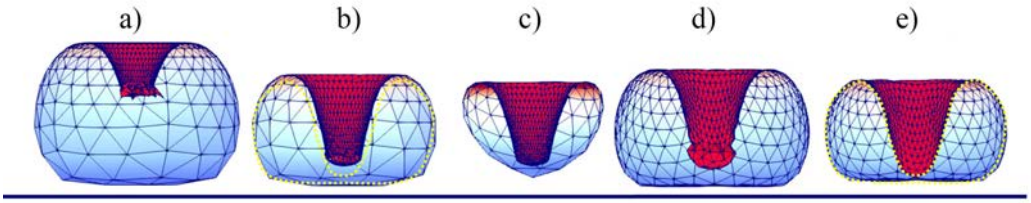

Figure 2.8: The comparison of the bubble shape just before the jet impact, compared with axisymmetric (dash-line) by (Zhang, Duncan and Chahine, 1994), using (a) no smoothing techniques are applied , (b) VPMT approach with $\Delta\varphi = 0.03$, (c) VPMT approach with $\Delta\varphi = 0.02$, (d) MEMT approach, and (e) MEMT together with VPMT with $\Delta\varphi = 0.03$. The remaining parameters are $\gamma = 1$, $R_m = 19$mm, $\varepsilon = 200$, $\delta = 0.04$, $We = 25900$, and $\kappa = 1.4$

and stability in the simulation. Also, the simulation took less time by at least 20% due to the larger time steps $\Delta\varphi = 0.03$. Moreover, the setting for the above smoothing techniques may vary according to the models and the simulation. For example, choosing a suitable weight, W, and the number of time steps that the smoothing is performing will affect the results such as the bubble size and the jet shape, as shown in figure 2.9.

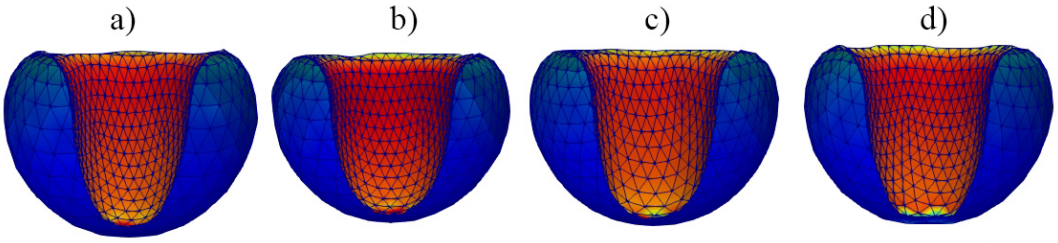

Figure 2.9: A comparison between the bubble shape just before the jet impact for a bubble placed above a horizontal wall at $\gamma = 1.2$, using (a) MEMT+VPST with $W = 0.5$, $\Delta\varphi = 0.03$, , (b) MEMT+VPST with $W = 0.5$, $\Delta\varphi = 0.02$, (c) MEMT+VPST with $W = 0.3$, $\Delta\varphi = 0.03$, and (d) EMT+VPST with $W = 0.5$, $\Delta\varphi = 0.03$. The remaining parameters are $R_m = 19$mm, $\varepsilon = 200$, $\delta = 0.04$, $W_e = 25900$, and $\kappa = 1.4$

2.5 Pressure calculation for bubble dynamics near a rigid wall

2.5.1 Direct BIM to calculate pressure contours

Consider the dynamics of a gas-bubble near a horizontal rigid wall as shown in Figure 2.10. Bernoulli equation can be used to calculate the pressure distribution

$$p = 1 - \frac{\partial \varphi}{\partial t} - \frac{1}{2}\left|\nabla\varphi\right|^2 - \delta^2 z. \tag{2.5.1}$$

Calculation of $\dot{\varphi} = \partial\varphi/\partial t$ using the finite difference method often results in unacceptable errors, due to very small time-steps usually used for simulating a violent collapsing bubble. However, the indirect boundary integral method (IBIM) is often used in the 3D-BIM to calculate the velocity potential and the pressure contours (Li et al., 2016; Wang and Khoo, 2004). We use the direct BIM to calculate $\dot{\varphi} = \partial\varphi/\partial t$ and the velocity field in the flow domain, which required different Green functions.

Consider the following boundary integral method

$$c(\boldsymbol{r}, t)\varphi(\boldsymbol{r}, t) = \int_{S_B} \Big[\psi(\boldsymbol{q}, t)G(\boldsymbol{r}, \boldsymbol{q}) - \varphi(\boldsymbol{q}, t)\frac{\partial G(\boldsymbol{r}, \boldsymbol{q})}{\partial n}\Big] dS(\boldsymbol{q}), \tag{2.5.2}$$

the Green function $G(\boldsymbol{r}, \boldsymbol{q})$ which satisfies the boundary conditions is chosen as

$$G(\boldsymbol{r}, \boldsymbol{q}) = \frac{1}{|\boldsymbol{r} - \boldsymbol{q}|} + \frac{1}{|\boldsymbol{r} - \boldsymbol{q}'|}, \tag{2.5.3}$$

where $\boldsymbol{q}'$ is the image of $\boldsymbol{q}$ on the rigid wall S_W. The term $\dot{\varphi}$ also satisfies the Laplace equation $\nabla^2\dot{\varphi} = 0$ in the flow (Tanizawa, 1995; Wu, 1998). It has the following boundary

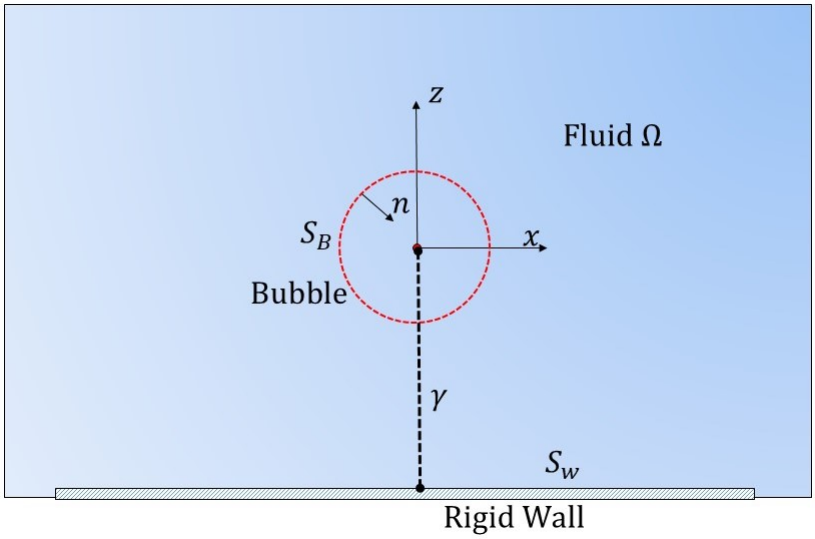

Figure 2.10: Geometry of a bubble near a flat rigid wall.

conditions

$$\begin{aligned} \dot{\varphi} &= 1 - \frac{1}{2}\left|\nabla\varphi\right|^2 - \delta^2 z - \varepsilon\left(\frac{V_0}{V}\right)^{\kappa}, \text{ on } S_B \\ \frac{\partial\dot{\varphi}}{\partial n} &= 0, \text{ on } S_W \\ \nabla\dot{\varphi} &\to 0, \text{as } r \to \infty. \end{aligned} \tag{2.5.4}$$

Here, $\dot{\varphi}$ satisfies the same boundary integral equation on the bubble surface as φ in (2.5.2) as follows

$$c(\boldsymbol{r},t)\dot{\varphi}(\boldsymbol{r}) = \int_{S_B}\Big[\dot{\psi}(\boldsymbol{q})G(\boldsymbol{r},\boldsymbol{q}) - \dot{\varphi}(\boldsymbol{q})\frac{\partial G(\boldsymbol{r},\boldsymbol{q})}{\partial n}\Big]dS(\boldsymbol{q}), \tag{2.5.5}$$

where $\dot{\psi}(\boldsymbol{q}) = \partial\dot{\varphi}/\partial n$ and $G(\boldsymbol{r},\boldsymbol{q})$ is the same Green function given in (2.5.3). After solving (2.5.5) for $\dot{\psi}(\boldsymbol{q})$ on the bubble surface, we have to put the control point $\boldsymbol{r}$ in the flow field, choose $c(\boldsymbol{r},t) = \pi/4$, and then solve (2.5.5) to obtain $\dot{\varphi}$ in the flow fields. The velocity in the flow field can be solved in the same manner as follows

$$4\pi\varphi_x(\boldsymbol{r}) = \int_{S_B}\Big[\psi_x(\boldsymbol{q})G(\boldsymbol{r},\boldsymbol{q}) - \varphi_x(\boldsymbol{q})\frac{\partial G(\boldsymbol{r},\boldsymbol{q})}{\partial n}\Big]dS(\boldsymbol{q}), \tag{2.5.6a}$$

$$4\pi\varphi_y(\boldsymbol{r}) = \int_{S_B}\Big[\psi_y(\boldsymbol{q})G(\boldsymbol{r},\boldsymbol{q}) - \varphi_y(\boldsymbol{q})\frac{\partial G(\boldsymbol{r},\boldsymbol{q})}{\partial n}\Big]dS(\boldsymbol{q}), \tag{2.5.6b}$$

$$4\pi\varphi_z(\boldsymbol{r}) = \int_{S_B} \Big[\psi_z(\boldsymbol{q})G(\boldsymbol{r},\boldsymbol{q}) - \varphi_z(\boldsymbol{q})\frac{\partial G(\boldsymbol{r},\boldsymbol{q})}{\partial n}\Big] dS(\boldsymbol{q}). \tag{2.5.6c}$$

To satisfy the boundary conditions we need to choose suitable Green functions. For equations (2.5.6a) and (2.5.6b) the same Green function as 2.5.3 can be used as it satisfies all the boundary conditions, $\nabla G \cdot \boldsymbol{n} = 0$, and $\psi_x = \psi_y = 0$ on S_W vanish on the rigid wall. However, $\psi_z \neq 0$ on S_W, therefore, a different Green function might be used to satisfy the boundary conditions as follows

$$G(\boldsymbol{r},\boldsymbol{q}) = \frac{1}{\big|\boldsymbol{r}-\boldsymbol{q}\big|} - \frac{1}{\big|\boldsymbol{r}-\boldsymbol{q'}\big|}. \tag{2.5.7}$$

The Green function (2.5.7) vanishes on the rigid wall S_W, however, $\varphi_z(\boldsymbol{q}) = 0$ vanished on the rigid wall. As such, all the calculations perform on the bubble surface S_B and the pressure on the flow field is obtained by plugging the results in the equation (2.5.1). In addition, the same idea is used for calculating the pressure contours for bubble dynamics in a corner with a right angle.

2.5.2 Validations of the pressure calculation

To verify the results, the numerical model is compared with the Rayleigh-Plesset equation (RPE) for a spherical bubble in an unbounded liquid. The pressure $p(\boldsymbol{r},t)$ from the spherical bubble theory is given as follows, in a coordinate system with the origin at the centre of the bubble

$$p(\boldsymbol{r},t) = 1 + \frac{R^2(t)}{r}\ddot{R}(t) + 2\left(\frac{R(t)}{r} - \frac{1}{4}\frac{R^4(t)}{r^4}\right)\dot{R}^2(t). \tag{2.5.8}$$

Figure (2.11) compares the BIM and the spherical bubble theory for the time histories of the pressure for two different field points, with radial distances from the bubble centre at $r = 1.5$ and 5 in figures (2.11a) and (2.11b), respectively. The BIM results has excellent agreement with that of the spherical bubble theory.

We next compare the present results with the pressure calculated with an axisymmetric

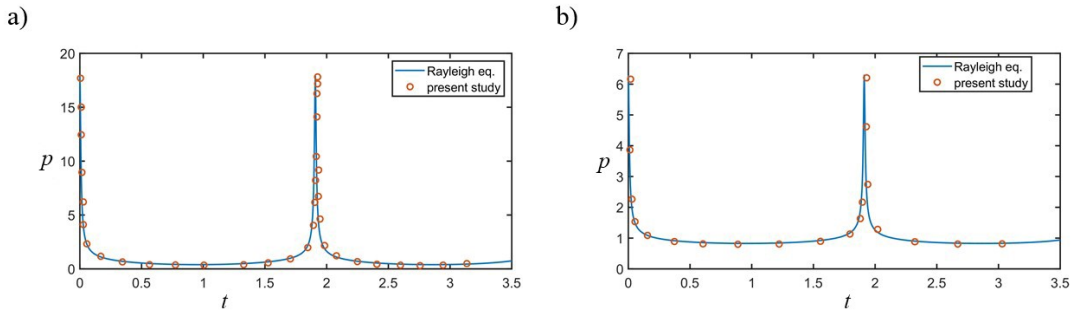

Figure 2.11: Comparison of the RPE and BIM for a bubble dynamic at infinity for the pressure a field point for (a) $r = 1.5R_m$ and (b) $r = 5R_m$. The remaining parameters are R_m= 0.8mm, $\varepsilon = 200$, $\delta = 0$ and $\kappa = 1.4$.

BIM by Li et al. (2016). It is for a bubble with $R_m = 16.6$ mm above a rigid wall, with $\gamma = 0.99$, $\varepsilon = 50$, $\delta = 0.04$ and $\kappa = 1.4$. The present 3D BIM (2.12a) agrees with the axisymmetric BIM (Li et al., 2016) (2.12b) for the pressure contour, velocity field, bubble shape and jet shape immediately before the jet impact.

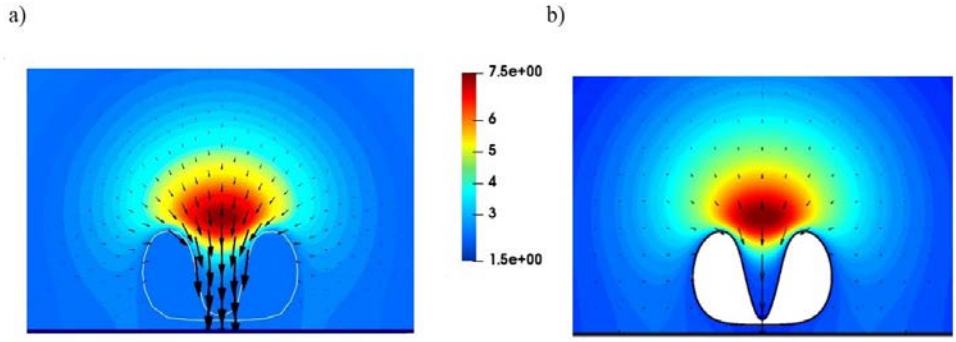

Figure 2.12: Comparison between the velocity field and pressure distributions of the (a) 3D-BIM model (present study) and (b) axisymmetric BIM (Li et al., 2016), for a bubble near a wall with $\gamma = 0.99$, and at $t = 2.32$. The rest of the parameters are $R_m = 16.6$mm, $\varepsilon = 50$, $\delta = 0.04$ and $\kappa = 1.4$.

Chapter 3

Numerical investigation of bubble dynamics at a corner

In this chapter, we aim to study the expansion, collapse and migration of the bubble, the behaviour of the jet, and the pressure contours of the flow field. The predicted bubble shapes have excellent agreement with the published experiments for $\alpha = \pi/2$ as well as the experiments performed for electric spark generated bubbles for $\alpha = \pi/4$. A parametric study is carried out in terms of the corner angle and the dimensionless standoff distances of the bubble centre at inception from the two walls.

3.1 Physical and mathematical modelling

Consider the dynamics of a gas bubble near a corner with an angle α formed by two rigid flat boundaries, to be called wall$_1$ and wall$_2$ henceforth, as shown in figure 3.1. The Cartesian coordinate system $Oxyz$ is set, with wall$_1$ being on $-\gamma_N$, wall$_2$ has an angle α from wall$_1$, $\alpha-$bisector being the symmetry plane of the configuration and the origin is the centre of the bubble at inception. The length scale is chosen as the maximum bubble radius R_m and the time reference scale is

$$T = R_m \sqrt{\frac{\rho_L}{\Delta p}}, \tag{3.1.1}$$

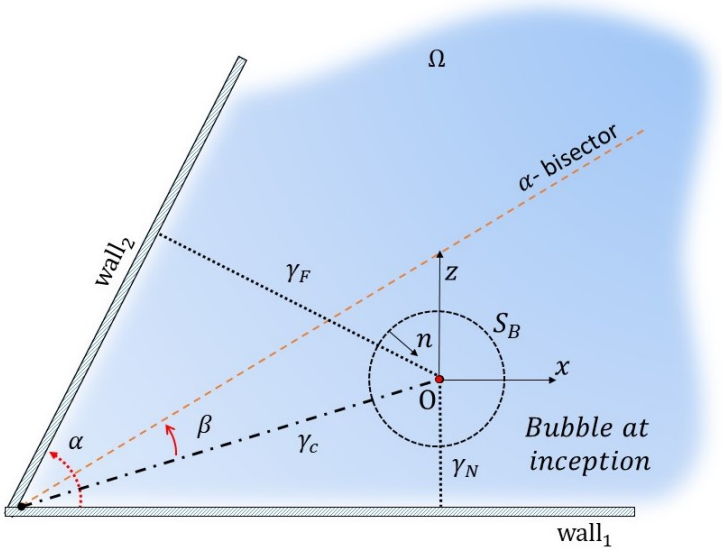

Figure 3.1: Configuration and coordinate system for bubble dynamics near a corner, with γ_c, γ_N and γ_F, being the dimensionless standoff distances of the bubble centre at inception from the corner, the near and far wall. The corner angle is α and the eccentricity angle of the initial position of the bubble centre from the α-bisector is β.

where $\Delta p = p_\infty - p_v$ is pressure scale, ρ_L, p_∞ and p_v are the liquid density, ambient atmospheric pressure and vapour pressure, respectively. Moreover, these values are taken as $\rho_L = 1000$ kg m^{-3}, $p = 101$ kPa and $p_v = 2.3$ kPa. Dimensionless variables are used in the remaining text unless stated otherwise.

This phenomenon is analysed using three main parameters α, β, and γ_c which are the angle between the two walls, the eccentricity from the $\alpha-$bisector (the lean angle from the bisector to the centre of the initial bubble), and the standoff distance from the corner to the centre of the bubble at inception, respectively as shown in figure 3.1,

$$\gamma_c = \frac{d}{R_m}, \tag{3.1.2}$$

where d is the dimensional distance from the corner to the centre of the bubble. Due to the symmetrical behaviour concerning β, the simulation is performed only for $\beta \in [0, \pi/2]$. Also, the standoff distances from the near wall and the far wall (γ_N and γ_F) are calculated

from their relation to α, β and γ_c as follows

$$\gamma_N = \gamma_c \sin\big(\frac{\alpha}{2} - \beta\big), \gamma_F = \gamma_c \sin\big(\frac{\alpha}{2} + \beta\big). \tag{3.1.3}$$

The flow is considered as inviscid, irrotational, and incompressible. Consequently, the fluid velocity $\boldsymbol{v}$ has a potential φ, $\boldsymbol{v} = \nabla\varphi$, satisfying Laplace's equation,

$$\nabla^2\varphi = 0. \tag{3.1.4}$$

The viscous effects of the liquid flow are neglected here since inertial effects are usually dominant for bubble dynamics (Manmi and Wang, 2017). The compressible effects are only essential during a short period at the end of the collapse (Wang and Blake, 2010, 2011; Wang, 2016).

The kinematic boundary conditions on the two walls, wall_1 and wall_2, the bubble surface S_B and at the far field are as follows

$$\frac{\partial\varphi}{\partial n} = 0 \text{ on } \text{wall}_1 \text{ and } \text{wall}_2, \tag{3.1.5a}$$

$$\frac{D\boldsymbol{r}}{Dt} = \nabla\varphi \text{ on } S_B, \tag{3.1.5b}$$

$$\nabla\varphi \to 0, \text{as } r \to \infty, \tag{3.1.5c}$$

where $\boldsymbol{r}$ is the position vector of the boundary, $\boldsymbol{n}$ is normal on the boundary surface, D/Dt denotes the material derivative, and r is the radial distance. The impermeable boundary condition on the rigid boundaries is (3.1.5a) and (3.1.5b) requires a material point on the bubble surface to remain there.

Assuming that the gas-bubble is under an adiabatic process, its dimensional pressure p_B satisfies

$$p_B = p_v + p_{g0}\Big(\frac{V_0}{V}\Big)^{\kappa}, \tag{3.1.6}$$

where p_{g0} is the initial pressure of the bubble gas, V_0 and V are the initial and transient bubble volumes, and κ is the polytropic index of the bubble gas. Additionally, heat and mass transfer across the bubble surface can be included (Szeri et al., 2003), but are neglected here.

The dynamic boundary condition on the bubble surface S_B requires that the pressure difference across the surface is equal to the Laplace pressure, which can be written as follows by

$$\frac{D\varphi}{Dt} = 1 + \frac{1}{2}\big|\nabla\varphi\big|^2 - \delta^2 z - \varepsilon\Big(\frac{V_0}{V}\Big)^{\kappa} + 2\frac{r_c}{We} \text{ on } S_B, \tag{3.1.7}$$

where $We = R_m\Delta p/\sigma$ is the Weber number, $\delta = \sqrt{\rho g R_m/\Delta p}$ is the buoyancy parameter, $\varepsilon = p_{g0}/\Delta p$ is dimensionless initial pressure inside the bubble and r_c is the radius of mean curvature of the bubble surface. The cases considered correspond to small bubbles, therefore the buoyancy effect is negligible, i.e. $\delta = 0$, unless explicitly stated otherwise. Buoyancy effects are essential for large bubbles (Wang, 1998, 2004).

3.2 Boundary integral method

In this section, we describe the BIM, the Kelvin impulse theory and the calculation of the velocity and pressure field in the flow domain.

3.2.1 Method of images

Using Green's second theorem, the potential can be expressed as the integral over the bubble surface

$$c(\boldsymbol{r},t)\varphi(\boldsymbol{r},t) = \int_{S_B}\Big[\psi(\boldsymbol{q},t)G(\boldsymbol{r},\boldsymbol{q}) - \varphi(\boldsymbol{r},t)\frac{\partial G(\boldsymbol{r},\boldsymbol{q})}{\partial n}\Big]dS(\boldsymbol{q}), \tag{3.2.1}$$

where $c(\boldsymbol{r},t)$ is the solid angle of bubble surface at the point $\boldsymbol{r}$ and $\psi(\boldsymbol{q},t) = \partial\varphi/\partial n$. Green's function $G(\boldsymbol{r},\boldsymbol{q})$ for Laplace's equation satisfies the impenetrable boundary conditions at the two walls. As the corner angle $\alpha = \pi/k$, in which k is a natural number,

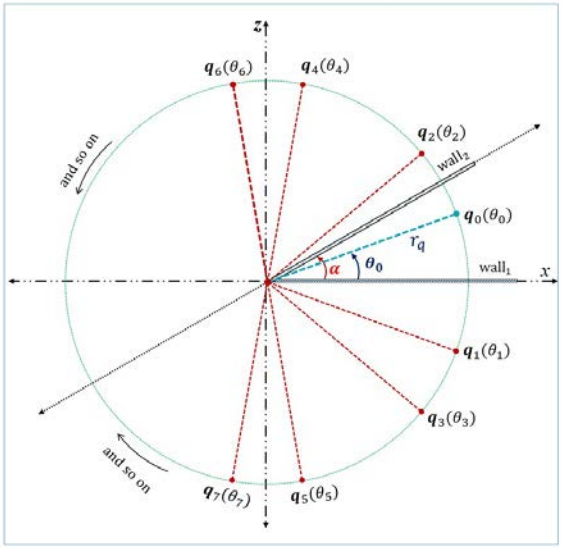

Figure 3.2: The images for a source point $\boldsymbol{q}_0$ which makes angle θ_0 with wall$_1$ for $\alpha = \pi/k$.

the Green function is given by

$$G(\boldsymbol{r}, \boldsymbol{q}) = \sum_{j=0}^{2k-1} \frac{1}{|\boldsymbol{r} - \boldsymbol{q}_j|}, \tag{3.2.2}$$

where $\boldsymbol{q}_0 = \boldsymbol{q}$ is the source point and $\boldsymbol{q}_j$, j = 1, 2,..., 2k-1 are 2k-1 images of $\boldsymbol{q}_0$ in the two walls. The images were provided by Kucera and Blake (1990) and Tagawa and Peters (2018). We provide a proof as follows.

Let the source point $\boldsymbol{q}_0 : (x_0, y_0, z_0)$ make an angle $\theta_a = \theta_0$ with wall$_1$ and its successive images $\boldsymbol{q}_j : (x_j, y_0, z_j)$, which make an angle θ_j with wall$_1$. The images lie on a circle with centre at $(0, y_0, 0)$ and a radius $r_q = \sqrt{x_0^2 + z_0^2}$. Figure 3.2 illustrates the images when a bubble is located between two walls inclined at an angle $\alpha = \pi/k$.

The angles of θ_j, j = 0, 1, 2, , 2k -1, can be divided into two groups as follows

$$\left\{ \frac{-2l\pi}{k} - \theta_a, \frac{2l\pi}{k} + \theta_a \right\}, l = 0, 1, 2, ..., k-1. \tag{3.2.3}$$

The source and images are thus symmetric to wall$_1$. Their angles relative to wall$_2$ are

$\Theta_j = \theta_j - \pi/k$ whose corresponding groups are

$$\left\{ \frac{-(2l+1)\pi}{k} - \theta_a, \frac{(2l-1)\pi}{k} + \theta_a \right\}, l = 0, 1, 2, ..., k-1. \tag{3.2.4}$$

Notice the last angle in the first group is $-(2k-1)\pi/k - \theta_a = -2\pi + \pi/k - \theta_a$, which is identical to $\pi/k - \theta_a$. Upon moving this last element from the first group to the first element, we have

$$\left\{ -\frac{(2l-1)\pi}{k} - \theta_a, \frac{(2l-1)\pi}{k} + \theta_a \right\}, l = 0, 1, 2, ..., k-1. \tag{3.2.5}$$

Therefore the source and the images are also symmetric to wall_2 (see appendix A for more details).

The BIM model is grid-free in the flow domain and computationally economical and is thus extensively used in the field of bubble dynamics. In the present BIM model, linear planar triangular elements are used on the bubble surface. At each time step, the bubble surface and potential distribution on the surface are known. With this information, the tangential velocity on the bubble surface can be calculated from the gradient of the potential at the surface S_B (Liu et al., 2016). The normal velocity on the bubble surface is obtained after solving the boundary integral equation (3.2.1). The bubble surface and potential distribution on the bubble surface are updated by performing the Lagrangian time integration to equations (3.1.5b, 3.1.7). This is obtained by using a second-order Runge-Kutta scheme, and an interpolated polynomial scheme coupled with the moving least square method. A variable time step is chosen for efficiency and accuracy, in such a way that a constant restrict the maximum change of the potential in each time step (Blake, Taib and Doherty, 1986; Blake and Gibson, 1987). A high-quality surface mesh is maintained by implementing a hybrid approach of the Lagrangian method and elastic mesh technique. The details of the numerical model using the BIM model for this problem can be found in chapter two.

3.2.2 Kelvin impulse theory for a bubble in a corner

The Kelvin impulse $\boldsymbol{I}$ of a bubble is defined as

$$\boldsymbol{I} = \int_{S_B} \varphi \boldsymbol{n} dS. \tag{3.2.6}$$

The Kelvin impulse corresponds to the apparent inertia of the bubble and its direction indicates the directions of the bubble migration and bubble jet (Blake, 1988; Blake, Leppinen and Wang, 2015).

If the bubble is taken a sufficient distance away from the boundary, it may be represented approximately by a time-varying point source. For a bubble at a corner with an angle of $\alpha = \pi/k$, where k is a natural number, the potential can be approximated by

$$\varphi(\boldsymbol{r}, t) = \frac{-m(t)}{4\pi} \sum_{j=0}^{2k-1} \frac{1}{|\boldsymbol{r} - \boldsymbol{q}_j|}, \tag{3.2.7}$$

where $m(t)$ is the source strength given by $4\pi R^2(t)\dot{R}(t)$, where $R(t)$ is the transient radius of the bubble and $\dot{R}(t)$ is its velocity. In this section, $\boldsymbol{q}_0$ denotes the initial bubble centroid and $\boldsymbol{q}_j$ for $j \geqslant 1$ denotes its images in the two walls.

The potential $\varphi(\boldsymbol{r}, t)$ in (3.2.7) can be rewritten as

$$\varphi(\boldsymbol{r}, t) = \frac{-m(t)}{4\pi|\boldsymbol{r} - \boldsymbol{q}_0|} + \Phi(\boldsymbol{r}, t), \quad \Phi(\boldsymbol{r}, t) = \frac{-m(t)}{4\pi} \sum_{j=1}^{2k-1} \frac{1}{|\boldsymbol{r} - \boldsymbol{q}_j|}. \tag{3.2.8}$$

Utilising this notation, the Kelvin impulse can be calculated following (Best and Blake, 1994) as follows

$$\boldsymbol{I} = \int_0^t \boldsymbol{F}(t) dt, \tag{3.2.9}$$

where

$$\begin{aligned}\boldsymbol{F}(t) = -m(t)\nabla\Phi(\boldsymbol{r}_s,t) &= \frac{m^2(t)}{4\pi}\sum_{j=1}^{2k-1}\nabla\left(\frac{1}{|\boldsymbol{r}-\boldsymbol{q}_j|}\right)\Bigg|_{\boldsymbol{r}=\boldsymbol{q}_0} \\ &= -\frac{m^2(t)}{4\pi}\sum_{j=1}^{2k-1}\left(\frac{\boldsymbol{q}_0-\boldsymbol{q}_j}{|\boldsymbol{q}_0-\boldsymbol{q}_j|^3}\right).\end{aligned} \tag{3.2.10}$$

Substituting (3.2.10) into (3.2.9), we have

$$\boldsymbol{I}(t) = \frac{-1}{4\pi}\sum_{j=1}^{2k-1}\left(\frac{\boldsymbol{q}_0-\boldsymbol{q}_j}{|\boldsymbol{q}_0-\boldsymbol{q}_j|^3}\right)\int_0^t m^2(t)dt. \tag{3.2.11}$$

The Kelvin impulse is determined by the positions of the initial bubble and its images in the two walls (or the corner angle α). Tagawa and Peters (2018) obtained the induced velocity at the bubble centroid using the method of images and complex functions via a two-dimensional analysis, which is in the same direction as the Kelvin impulse (3.2.11). The Rayleigh bubble solution for m(t) is (Blake, Taib and Doherty, 1986),

$$m^2(t) = \frac{32\pi^2}{2}R(t)\big(1-R^3(t)\big). \tag{3.2.12}$$

For a Rayleigh bubble, we can calculate the Kelvin impulse at the end of collapse $T_c \approx 1.83$ as follows

$$\boldsymbol{I}(T_c) = -\frac{4\sqrt{6}\pi}{9}B\Big(\frac{7}{6},\frac{3}{2}\Big)\sum_{j=1}^{2k-1}\left(\frac{\boldsymbol{q}_0-\boldsymbol{q}_j}{|\boldsymbol{q}_0-\boldsymbol{q}_j|^3}\right), \tag{3.2.13}$$

where $B(z,w)$ is the beta function (see Abramowitz and Stegun (1965)). A procedure can be found in appendix B to calculate equation (3.2.13).

3.2.3 Calculation of velocity and pressure in the flow domain

The velocity $\nabla\varphi$ can be calculated using the finite difference method with the potential calculated from the BIM (3.2.1).The pressure distribution can be calculated using the

Bernoulli equation,

$$p = 1 - \dot{\varphi} - \frac{1}{2}\nabla\left|\varphi\right|^2 - \delta^2 z. \tag{3.2.14}$$

However, to calculate $\dot{\varphi} = \partial\varphi/\partial t$ using the finite difference method often results in unacceptable errors, due to the very small time-steps usually used for simulating a violent collapsing bubble. We calculate $\dot{\varphi}$ using the BIM model following Tanizawa (1995) and Wu (1998).

The boundary volume problem for $\dot{\varphi}$ can be obtained from (3.1.4, 3.1.5a, and 3.1.5c) as follows

$$\begin{aligned} &\nabla^2\dot{\varphi} = 0, \\ &\frac{\partial\dot{\varphi}}{\partial n} = 0 \text{ on wall}_1, \text{ wall}_2, \\ &\nabla\dot{\varphi} \to 0 \text{ as } r \to \infty. \end{aligned} \tag{3.2.15}$$

Therefore, $\dot{\varphi}$ satisfies the same boundary integral equation on the bubble surface as φ as follows

$$c(\boldsymbol{r},t)\dot{\varphi}(\boldsymbol{r},t) = \int_{S_B}\Big[\dot{\psi}(\boldsymbol{q},t)G(\boldsymbol{r},\boldsymbol{q}) - \dot{\varphi}(\boldsymbol{q},t)\frac{\partial G(\boldsymbol{r},\boldsymbol{q})}{\partial n}\Big]dS(\boldsymbol{q}), \tag{3.2.16}$$

where $\dot{\psi}(\boldsymbol{q},t) = \partial\dot{\varphi}/\partial n$, $G(\boldsymbol{r},\boldsymbol{q})$ is the same Green's function given in (3.2.2). Moreover, $\dot{\varphi}$ on S_B is obtained from the dynamic boundary condition

$$\dot{\varphi} = 1 - \frac{1}{2}\big|\nabla\varphi\big|^2 - \delta^2 z - \varepsilon\Big(\frac{V_0}{V}\Big)^{\kappa} + 2\frac{r_c}{We} \text{ on } S_B. \tag{3.2.17}$$

On the bubble surface S_B, $\partial\dot{\varphi}/\partial n$ can thus be calculated using the BIM (3.2.1). In the flow field, $\dot{\varphi}(\boldsymbol{r},t)$ is then calculated using (3.2.16).

3.3 Validation of the numerical model

3.3.1 Comparison with experiment

To evaluate the BIM model, we compare the computational results with experimental images. The first case is for a laser beam generated bubble having a maximum radius $R_m = 0.85$ mm at a right-angled corner for $\alpha = \pi/2,\ \beta = 0.1$ and $\gamma_c = 1.4$ (Brujan et al., 2018). The corresponding dimensionless distance of the bubble centre at the inception form the near and far walls are $\gamma_F = 0.88$ and $\gamma_N = 1.08$. As shown in figure 3.3, during the early stages of the expansion (frame 1), the bubble remains spherical except its surface facing the near wall is retarded by the wall. At the end of the expansion (frame 3), the parts of the bubble surface facing two walls are flattened by the walls, with the greater flattening by the near wall, while the distal part opposite to the corner remains spherical. The bubble collapses from the distal side, with the near wall sides kept in contact with the wall (frames 3-6). Towards the end of the collapse, a wide jet forms on the distal side which points to the corner (frames 5-6). All the features are reproduced by the computations and the bubble shapes obtained from the computations are in very good agreement with the experiments, except that the bubble jet is not visible in the experiments due to the opaqueness of the bubble. The second case is for a bubble initiated at the bisector

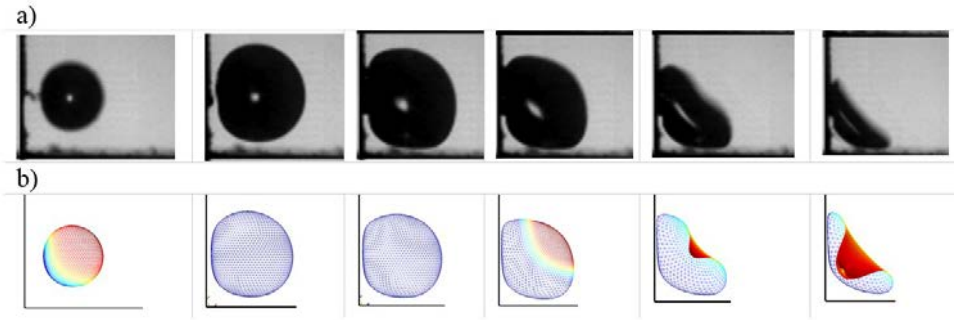

Figure 3.3: Comparison between (a) experimental (Brujan et al., 2018) and (b) BIM results characterized by $\alpha = \pi/2$, $\beta = 0.1$, $\gamma_F = 0.88$, $\gamma_N = 1.08$, $R_m = 0.85$ mm, $\varepsilon = 100$, $\delta = 0.009$, $\kappa = 1.4$, and $We = 1152$. The dimensionless times are $t = 0.2, 0.91, 1.37, 2.1, 2.52$, and 2.68, respectively.

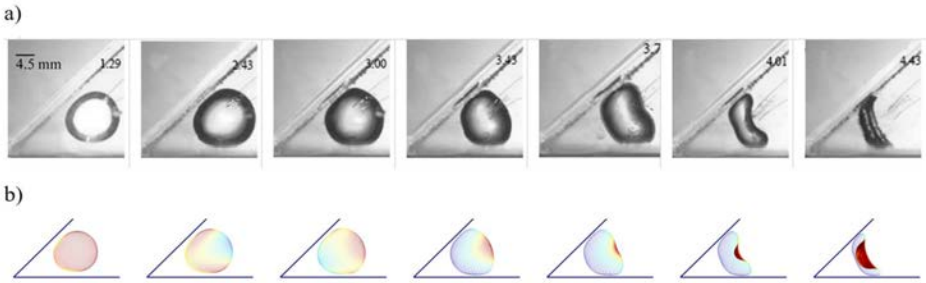

Figure 3.4: Comparison between (a) experimental and (b) BIM results characterized by $\alpha = \pi/4$, $\beta = 0$, $\gamma_N = 1.03$, $\gamma_F = 1.03$, $R_m = 13.5$ mm, $\varepsilon = 100$, $\delta = 0.036$, $\kappa = 1.4$, and $We = 1886$. The dimensionless times are t =0.96, 1.813, 2.23, 2.55, 2.76, 2.99, and 3.305, respectively.

of an acute corner for $\alpha = \pi/4$, $\beta = 0$, and $\gamma_c = 2.69$. The experiments were carried out with a spark-generated bubble in water and recorded by a high-speed camera (Cui et al., 2019). Experiments are performed in a cubic glass tank with 0.5 m side length filled with tap water to a depth of 0.4 m. Two transparent rectangular fiberglass walls form a corner with a thickness of 4.5 mm. The two walls are inserted from the top of the glass tank using adjustable positioners. A 2 kW spot light opposite illuminates the water tank to the camera through a diffuser (matte glass). Images of bubbles are recorded by a VRI-Phantom V611 high-speed camera working at 20,000 frames per second with an exposure time of 140,000 ns. The interval between two image frames is 144.93 μs, which is small compared to the period of bubble oscillation (about 6 ms)(Cui et al., 2019).

The maximum bubble radius is about $R_m = 13.5$mm. This is associated with $\gamma_N = \gamma_F = 1.03$. Large parts of the bubble surface facing two walls are flattened by the walls at the end of the expansion (frame 2) as shown in figure 3.4. During collapse (frames 3-7), the parts of the bubble surface facing the two walls are kept in contact with the walls, the distal side opposite to the corner collapses faster than the side facing the corner, a jet forms pointing towards the corner in the late stage of the collapse (frames 6 and 7). Again, the computations agree well with the experiment for this case.

3.3.2 Convergence tests

To analyze the convergence of the BIM modelling, convergence tests were performed for the case for $\alpha = \pi/2$, $\beta = 0.1$, $\gamma_c = 2.12$ and $R_m = 0.80$ mm. Various numbers of the elements were used on the bubble surface, $M = 720, 980, 1280$ and 2000. Figures 3.5(a) and 3.5(b) show the results of the time histories for the jet velocity v_{jet} and the equivalent bubble radius $R_{eq} = (3V/4\pi)^{1/3}$. Both results converge well with the surface element number M as $M = 980$. Figure 3.5(c) compares the bubble shapes immediately before jet impacting on the opposite bubble surface for various values of M. It shows that the bubble shape for M = 1280 agrees well with that for $M = 2000$. All the remaining calculations in this study were performed for $M = 1280$.

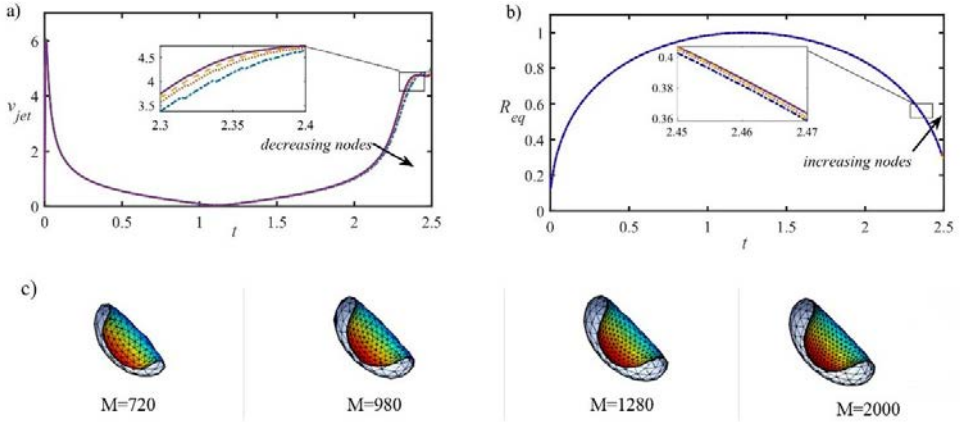

Figure 3.5: Convergence tests for the BIM modelling in terms of (a) time history of the jet velocity, (b) equivalent bubble radius, and (c) bubble shapes immediately before jet impact for $\alpha = \pi/2$, $\beta = 0$, $\gamma_c = 2.12$, $We = 1084$, $\kappa = 1.4$, $\delta = 0.0089$, and $R_m = 0.8$ mm for various bubble surface elements $M = 720, 980, 1280$ and 2000.

3.4 Numerical results

3.4.1 Symmetric cases ($\beta = 0$)

We firstly consider symmetric cases for bubbles initiated at the bisector of the corner for $\beta = 0$. Figure 3.6 displays bubble dynamics near a right-angled corner $\alpha = \pi/2$ at

various standoff distances from the two walls for $\gamma = \gamma_N = \gamma_F = 1, 2, ..., 6$. Each row in figure 3.6(a) illustrates the bubble shapes at the inception of the bubble, the maximum volume, jet formation, and jet impact on the opposite bubble surface. The bubble expands approximately spherically (frame 1), except for $\gamma = 1$ for which the bubble surfaces facing the two walls are compressed by the walls (frame 1).

During the latter stages of the collapse, the bubble becomes oblate along the bisector direction, the far side of the bubble opposite to the corner becomes noticeably flattened and a high-speed liquid jet forms pointing to the corner (frames 2 and 3). As the bubble is initiated closer to the corner, the bubble volumes at the start of jet formation and jet impact and the width of the jet increase. The start of jet formation is at the moment when the far side becoming flattened.

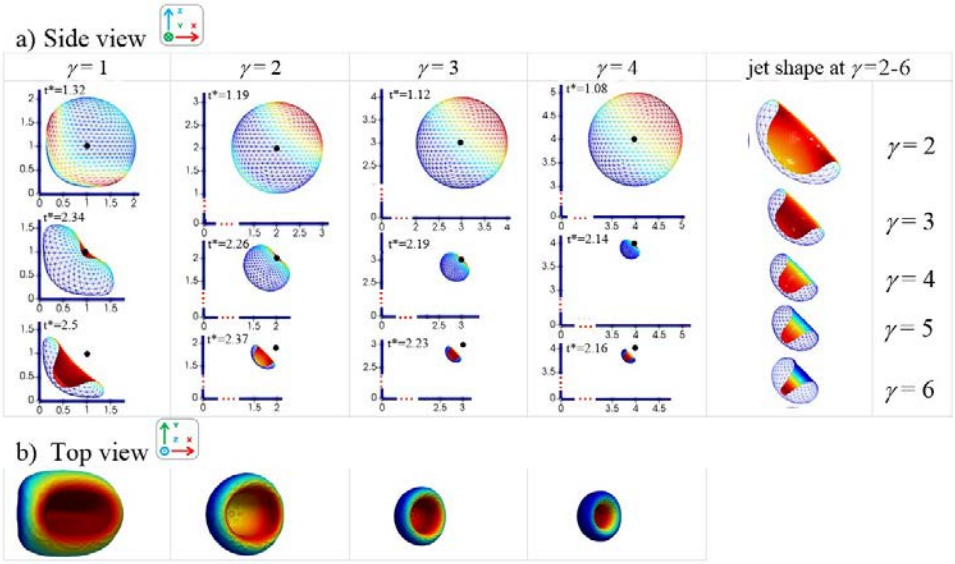

Figure 3.6: Bubble dynamics near a right-angled corner $\alpha = \pi/2$ at various standoff distances from the two walls $\gamma = \gamma_F = \gamma_N = 1, 2, 3, 4, 5$, and 6: (a) Side view of the bubble shapes at inception (dot point), maximum volume, jet formation and jet impact, enlarged bubble shapes before jet impact, and (b) Top views of the enlarged bubble shape before impact. The remaining parameters are set as $\beta = 0$, $R_m = 0.85$ mm, $\varepsilon = 200$, $\delta = 0.009$ κ= 1.4,and $We = 1152$.

The Bjerknes forces are forces on bubbles due to pressure. The primary Bjerknes forces are due to an external pressure field, and the secondary Bjerknes forces are caused

by a neighbouring bubbles or boundaries. The bubble becomes oblate along the bisector during collapsing, as the second Bjerknes forces are stronger for the parts of the bubble surfaces near the walls. The jet pointing towards the corner, due to the combined effects of the two second Bjerknes forces.

Figure 3.7 shows the bubble shapes in a smaller corner angle for $\alpha = \pi/4$. The bubble remains spherical during the expansion except for $\gamma \leqslant 1$ for which it becomes elongated along the bisector direction. A jet forms towards the end of the collapse pointing to the corner (frame 3). The bubble volumes at jet formation and jet impact and the jet width increase inversely with γ. These features are analogous to a bubble oscillating near a flat wall (Blake, Taib and Doherty, 1986). Also, comparing figures 3.6 and 3.7, one can see that the bubble volumes at jet formation and jet impact and the jet width increase inversely with α. Note that the jet for $\gamma = 6$ is slightly asymmetric due to the numerical errors associated with the asymmetric mesh.

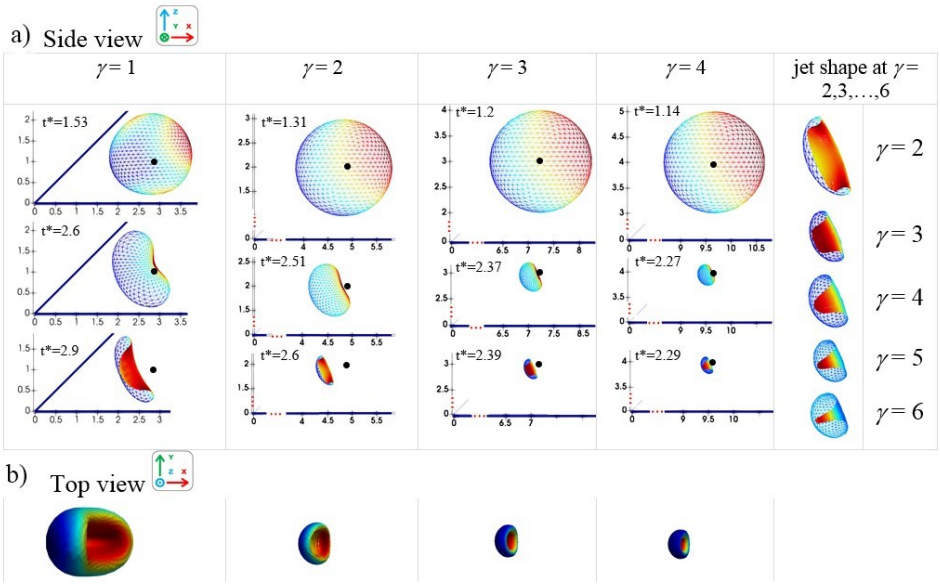

Figure 3.7: Bubble dynamics near a corner angled at $\alpha = \pi/4$ at various standoff distances from the two walls $\gamma = 1, 2, ..., 6$: (a) Side view of the bubble shapes at inception (dot point), maximum volume, jet formation and jet impact, enlarged bubble shapes before jet impact, and (b) Top views of the enlarged bubble shape before impact. The remaining parameters are the same as in figure 3.6.

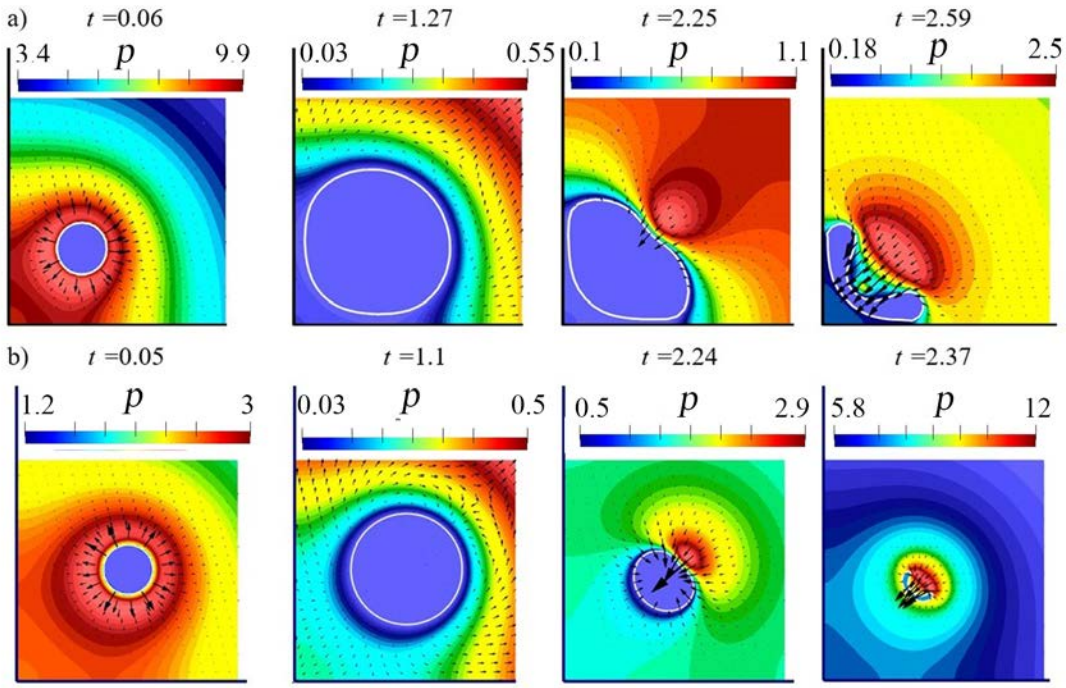

Figure 3.8: Pressure contours and velocity fields in the flow domain and normal velocity on the bubble surface for a bubble in a corner with $\alpha = \pi/2$ and at (a) γ =1.0, (b) $\gamma = 2.0$, for the case shown in figure 3.6.

Figure 3.8 shows the pressure contours and velocity fields in the flow domain for $\alpha = \pi/2$ and $\gamma = 1, 2$, with the remaining parameters being the same as figure 3.6.The pressure field loses spherical symmetry at the start of the expansion, even though the bubble is approximately spherical (frames a1, a2, b1 and b2). The pressure decreases radially and is relatively high near the corner (frames a1 and b1). The velocity decreases radially too and decreases faster on the wall sides. At the start of the collapse (frames a2 and b2), the pressure increases radially and is small in the corner and the flow becomes almost motionless there, stagnation points occurring on the bisector of the corner. The liquid far away from the bubble moves away and the liquid near the bubble surface opposite to the corner moves back, where the bubble first collapses. A stagnation point is formed on the bisector. During the later stages of the collapse, a high-pressure zone develops on the opposite side of the bubble to the corner (frames a3 and b3), which subsequently generates the jet and pushes the bubble towards the corner (frames a4 and b4). Similar

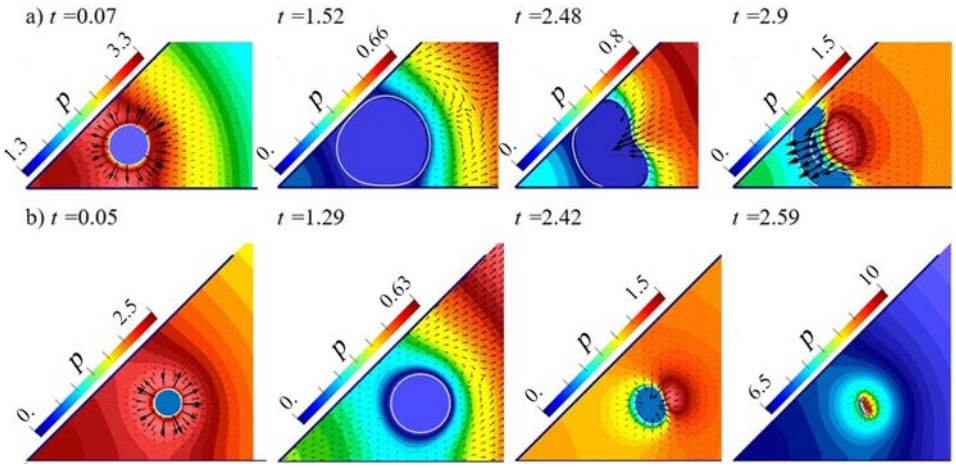

Figure 3.9: Pressure contours and velocity fields in the flow domain and normal velocity on the bubble surface for a bubble in a corner with $\alpha = \pi/4$ and at (a) γ =1.0, (b) $\gamma = 2.0$, for the case shown in figure 3.6.

features were observed for a bubble oscillating near a flat wall (Li et al., 2016). As the bubble is initiated closer to the corner, the pressure near the corner is larger during the early stages of the expansion and lower towards the end of the collapse.

Figure 3.9 displays the similar features of the pressure contours and velocity fields in the flow domain for $\alpha = \pi/4$, with other parameters being the same as in figure 3.8. However, a larger zone of higher pressure at the corner during the early stage of the expansion and a larger zone of lower pressure towards the end of the collapse are observed for $\alpha = \pi/4$. The high pressure zone near the base of the jet forms later, since the flow following the receding bubble surface along the walls are closer to the bisector than that for $\alpha = \pi/2$.

In this and some other cases, the bubble surface tends to keep in contact with walls once started. This did not cause any singularity problem in the computations as the normal velocity and normal derivative of the Green function are small in this region. Wang, Shi and Zhang (2015) discussed the following mechanism on this phenomenon. The pressure in the thin layer of liquid between the bubble and the boundary is approximately constant and equal to the pressure of the bubble gas. The flow velocity within the thin layer is close to zero. In addition, the surface tension effects tend to keep this part of the bubble

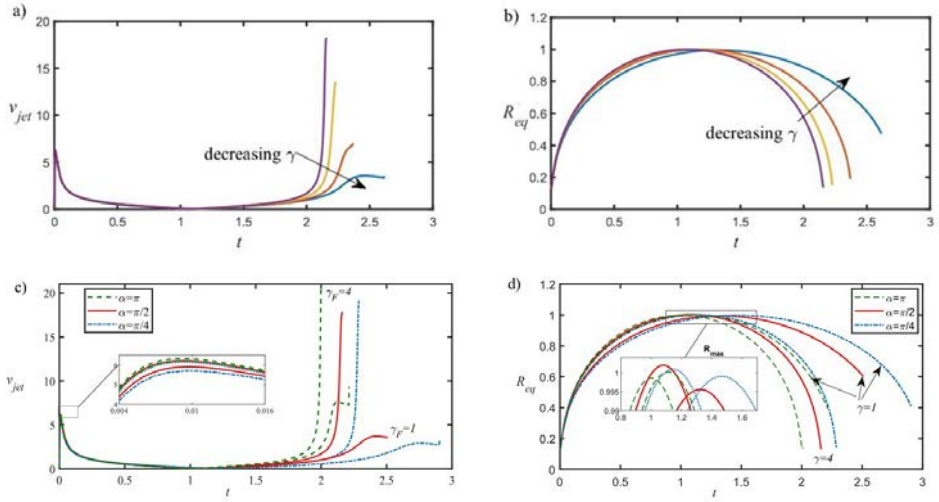

Figure 3.10: Time histories of the jet velocity v_{jet} and the equivalent bubble radius R_{eq} for the cases shown in figures 3.6 and 3.7.

surface, as the pressure is constant and equal at its two sides. Reuter and Kaiser (2019) measured the time evolution of the liquid-film thickness of a single cavitation bubble in water collapsing onto a solid surface. They found that during the first cycle of oscillation, the bubble does not come in direct contact with the solid surface.

Figures 3.10(a) and 3.10(b) show the time histories of the jet velocity v_{jet} and equivalent bubble radius R_{eq} for $\alpha = \pi/2$ and $\gamma = 1$, 2, 3, 4. As the bubble is initiated nearer the corner, the oscillation period increases and the jet velocity decreases. From γ= 4 to 1, the oscillation period increases by 12% and the dimensionless maximum jet velocity decreases from 17.8 to 3.5. Figures 3.10(c) and 3.10(d) show the time histories for $\alpha = \pi/2$, $\alpha = \pi/4$, γ= 1, 4. For comparison, we also display the results for a bubble near a rigid flat boundary ($\alpha = \pi$) For a smaller corner angle, the oscillation period increases and the jet velocity decreases. For $\gamma = 1$, the oscillation period increases by 10% and the maximum jet velocity decreases by 21% as α decreases from π/n to $\pi/2n$ for $n = 1$, and 2.

Figure 3.11 displays the time history of the displacement of the bubble centroid $d_c(t)$ and the kelvin impulse I for cases shown in figures 3.6 and 3.7. For the case of a bubble near a rigid flat boundary, $dc(t)$ is the distance history from the bubble centroid to the boundary. The bubble moves away from the corner during expansion along the bisector

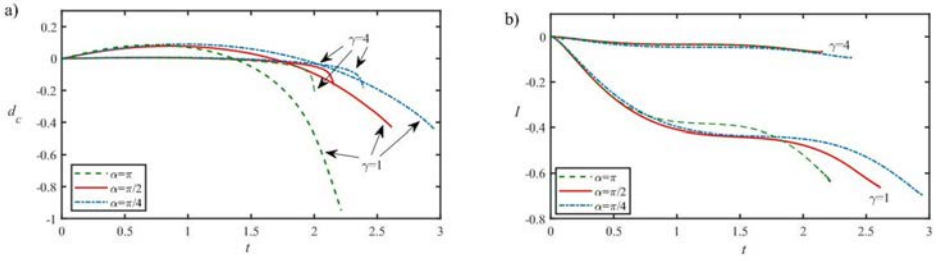

Figure 3.11: Time history of the (a) displacement of the bubble centroid, and (b) Kelvin impulse, for the cases in figures 3.6 and 3.7.

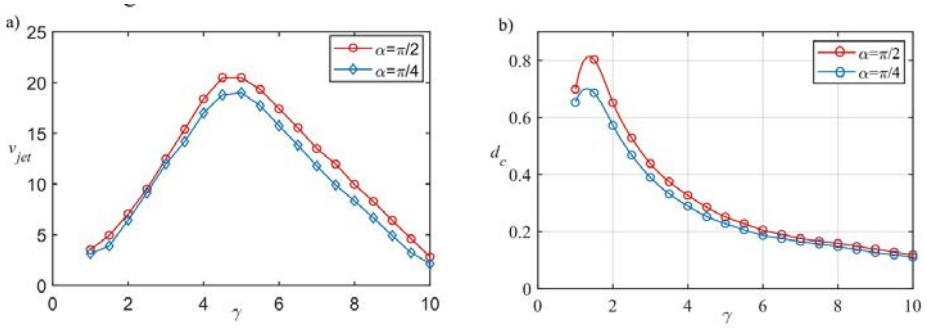

Figure 3.12: Comparison of the (a) jet velocity, and (b) bubble centroid displacement versus γ for $\alpha = \pi/2$ (red-line) , and $\alpha = \pi/4$ (blue-line), for the cases in figures 3.6 and 3.7.

and moves back at much higher amplitude during the collapse as shown in figure 3.11(a). The migration amplitude decreases with γ and increases with α (see figure 3.12). These trends have been verified in our calculations for $1 \leqslant \gamma \leqslant 20$.Figure 3.11(b) shows the effects of α on the bubble dynamics. The magnitude of the of the Kelvin impulse increases with both γ and α. Also the bubble life time increases with α but decreases with γ.

Figure 3.12 displays the jet velocity and displacement amplitude of the bubble centroid $dc(t)$ before jet impacting on the opposite bubble wall. The jet velocity firstly increases with the standoff distance from the corner, reaches the maximum around $\gamma = 5$ and after that decreases. The displacement amplitude dc(t) firstly increases and then decreases with γ too, but reaching the maximum much earlier around $\gamma = 1.5$. Both the jet velocity and displacement amplitude increases with the corner angle α.

3.4.2 The asymmetric case ($\beta \neq 0$)

Figure 3.13 shows the bubble shapes for the asymmetric cases ($\beta \neq 0$), for $\alpha = \pi/2$, $\gamma_N = 1$ and $\gamma_F = 2, 3, 6$, and 15. Each row in figure 3.13(a) illustrates the bubble shapes at the inception, maximum bubble volume, jet formation and immediately before the jet impact. The bubble expands spherically for all of the cases, except for the near bubble surface which is flattened by the near wall. The bubble is symmetric to the vertical plane to the near wall passing through its geometrical centre for $\gamma_F \geqslant 2$.

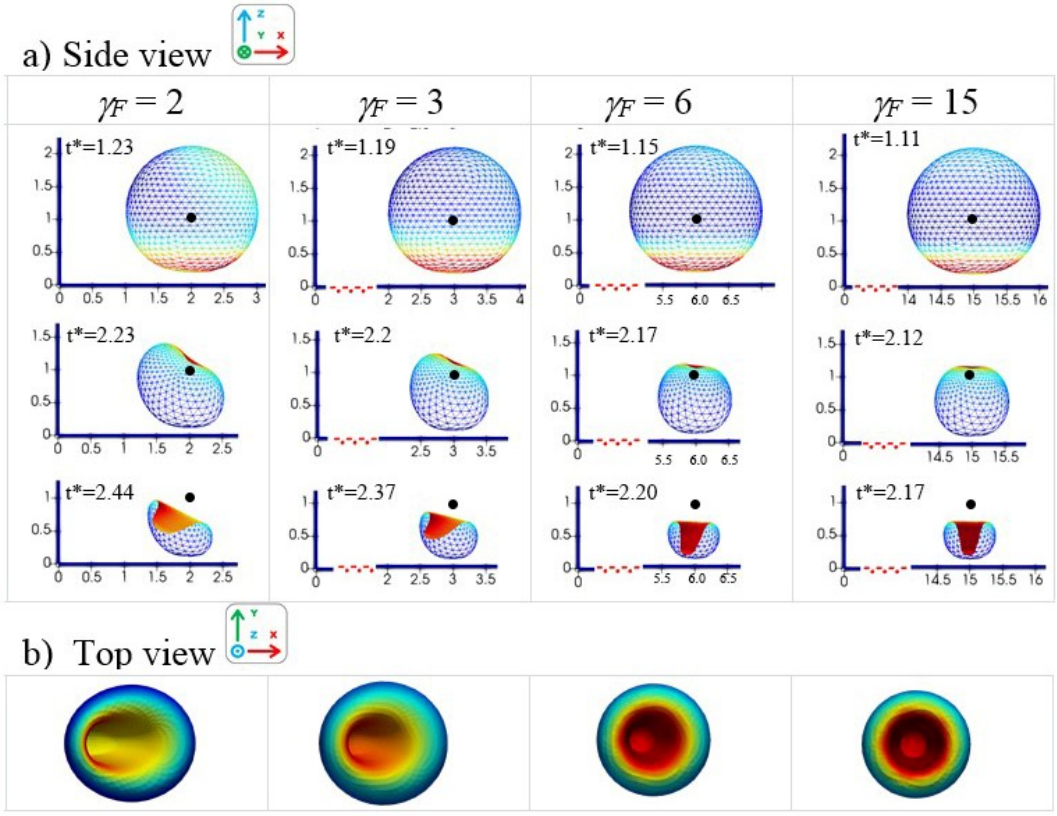

Figure 3.13: Bubble shapes at different views for $\gamma_N = 1$, various values of γ_F, and $\alpha = \pi/2$, (a) xz-coordinate view, and (b) xy-coordinate view. The remaining parameters are the same as in figure 3.6.

During the later stages of the collapse (the third row), the bubble develops a non-spherical, asymmetry for $\gamma_F \leqslant 3$ but approximately symmetric to the plane vertical to the near wall for $\gamma_F \geqslant 6$. The jet starts to form on the part of the bubble surface opposite to the near wall and further away from the far wall. Towards the end of the collapse, the

jet is approximately pointing to the wall, but inclined to the further wall as γ_F decreases. The bubble volumes at jet formation and jet impact and the jet width decrease with γ_F.

Figure 3.14(a) shows the corresponding bubble shapes for $\alpha = \pi/4$. The jet is approximately pointing vertically to the near wall for $\gamma_F = 15$ but inclined to the further wall as γ_F decreases. Here, the jet is more inclined to the further wall, and it is wider compared with the case for $\alpha = \pi/2$.

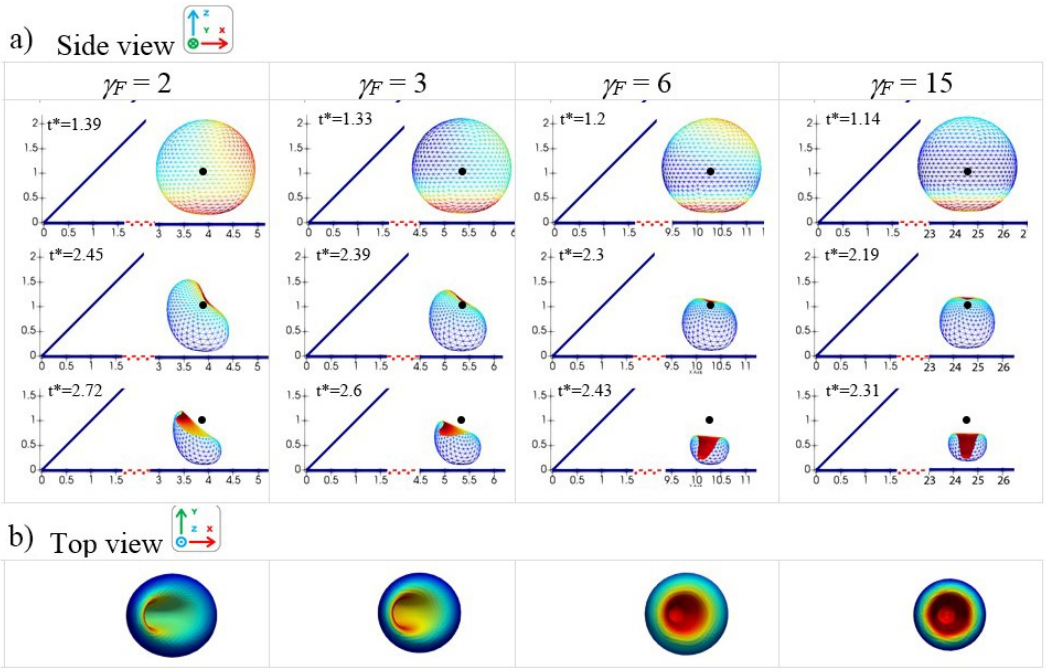

Figure 3.14: Bubble shapes at different views for $\gamma_N = 1$, various values of γ_F, and $\alpha = \pi/4$, (a) xz-coordinate view, and (b) xy-coordinate view. The remaining parameters are the same as in figure 3.6.

Figures 3.13(b) and 3.14(b) show the top view, (xy plane), of the bubble shape immediately before the jet impact. It is observed that the bubble is elongated along the symmetrical plane of the configuration. This effect reduces with increasing γ_F and the top view of the bubble and jet shapes become axisymmetric for $\gamma_F > 6$.

Figure 3.15 presents the pressure contours and velocity vectors for a bubble in a corner with $\alpha = \pi/2$, $\gamma_N = 1$, $\gamma_F = 2$ in figure 3.15(a), $\gamma_F = 3$ in figure 3.15(b) and the remaining parameters are the same as in figure 3.13. During the early stages of the expansion, the pressure decreases radially from the bubble and is relatively high between the bubble and

the near wall (frames a1 and b1). The velocity decreases radially too but decreases faster on the wall sides. At the start of the collapse, the pressure increases further away and is relatively low between the bubble and the near wall (frames a2 and b2). The liquid in the

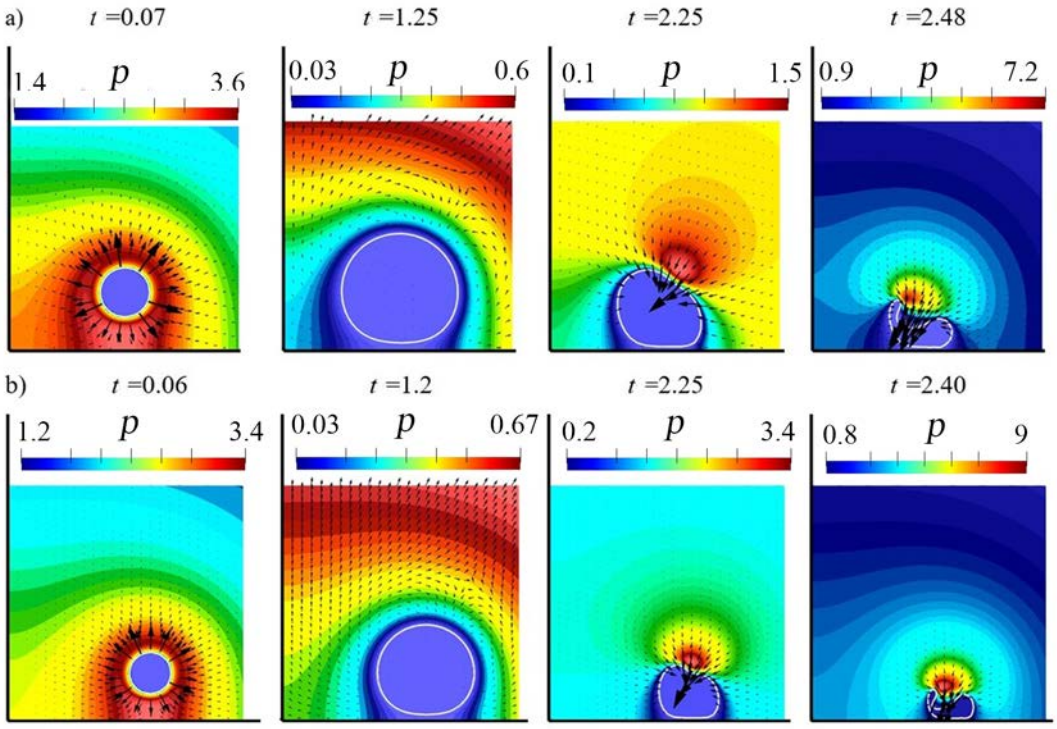

Figure 3.15: Pressure contours and velocity vectors for a bubble in a corner for $\alpha = \pi/2$, $\gamma_N = 1$ and (a) $\gamma_F = 2$, (b) $\gamma_F = 3$, for the cases in figure 3.13.

far field flows outwards and the liquid near the part of the surface opposite to the near wall and further away from the far wall recedes, where the bubble first collapses, resulting in a stagnation point between the bubble and the far field. In the late stages of collapse (frames a3 and b3), a high-pressure zone develops above the bubble and away from the far wall, which subsequently generates the jet towards the near wall, but inclined to the far wall (frames a4 and b4). During the period of jet development, the high-pressure zone moves towards the far wall. As the bubble is initiated nearer to the corner, the pressure field displays stronger asymmetry in the vertical plane to the near wall passing through the bubble centroid, and the high-pressure zone is more inclined away from the vertical plane.

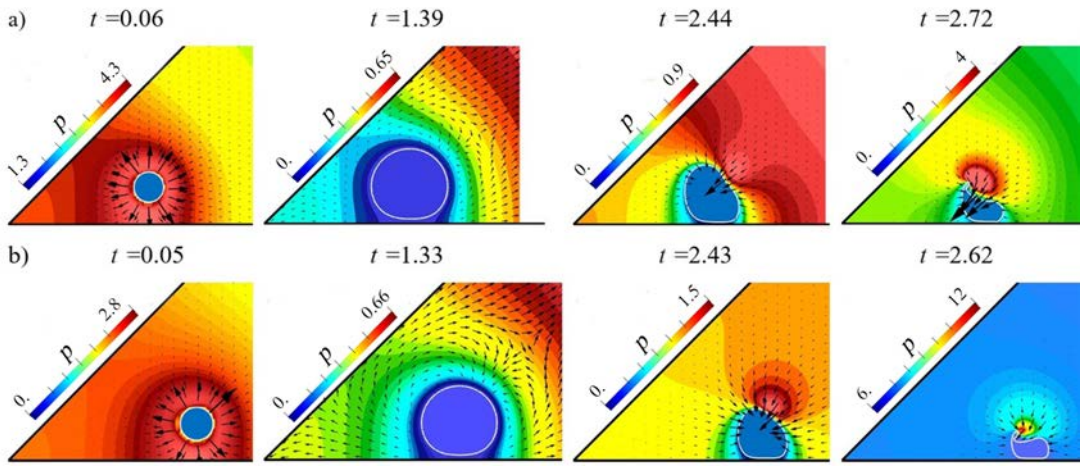

Figure 3.16: Pressure contours and velocity vectors for a bubble in a corner for $\alpha = \pi/4$, $\gamma_N = 1$ and (a) $\gamma_F = 2$, (b) $\gamma_F = 3$, for the cases in figure 3.14.

Figure 3.16 displays similar features of the pressure contours and velocity vectors in the domain for a bubble in a corner with $\alpha = \pi/4$. During the early stages of the expansion (collapse), the pressure decreases (increases) radially, quickly in the open side but slowly towards the near wall. A velocity stagnation point forms at the start of the collapse and high pressure zone forms during the late stages of the collapse above the bubble and away from the far wall. The asymmetry of the pressure field to the plane vertical to the near wall passing through the bubble centre is stronger than that for $\alpha = \pi/2$.

Figures 3.17(a) and 3.17(b) show the time histories of the jet velocity v_{jet} and the equivalent bubble radius R_{eq}, respectively, for $\alpha = \pi/2$, $\gamma_N = 1$ and $\gamma_F = 1, 2, 3, 4$. The period of bubble oscillation decreases with γ_F but the jet velocity increases with γ_F. Figure 3.17(c) and Figure 3.17(d) show the time histories of the jet velocity v_{jet} and the equivalent bubble radius R_{eq}, for $\alpha = \pi/2$, $\alpha = \pi/4$ and $\gamma_F = 1, 4$. The period decreases with α but the jet velocity increases with α. The maximum bubble volume does not change significantly with α and γ_F.

Figures 3.18(a) and 3.18(b) shows the displacements of the bubble centred (x_c, z_c) versus time. The bubble migrates away from the near wall and corner during expansion and moves back to the near wall and corner during collapse at much larger speed and

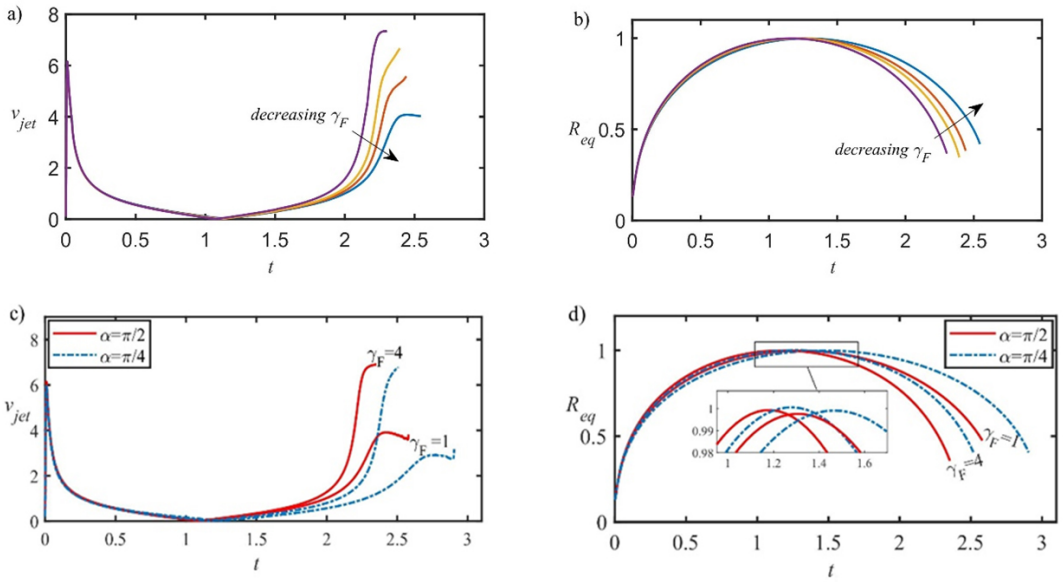

Figure 3.17: Time histories of (a) the jet velocity v_{jet} and (b) the equivalent bubble radius R_{eq} for $\alpha = \pi/2$, $\gamma_N = 1$ and $\gamma_F = 1, 2, 3, 4$; (c) jet velocity v_{jet} and (d) the equivalent bubble radius R_{eq} for $\alpha = \pi/2$, $\alpha = \pi/4$, $\gamma_N = 1$ and $\gamma_F = 1, 4$ for the cases in figures 3.13 and 3.14.

amplitude. This is analogous to a bubble oscillating near a wall, migrating away from the wall during expansion and moves back during collapse (Blake, Taib and Doherty, 1986). The amplitude of migration towards the corner, x_c, decreases with γ_F but increases with α. The amplitude of migration perpendicular to the near wall, z_c, increases both with γ_F and α. These trends are consistent to the time histories of the Kelvin impulse shown in figure 3.19. The x-component of the Kelvin impulse decreases with γ_F but increases with α, whereas the z-component of the Kelvin impulse increases with both γ_F and α.

Figure 3.20 compares the directions of the Kelvin impulse and the jet direction. The directions of the Kelvin impulse are obtained using both the analytic result (3.2.11), θ_I, and the BIM result, θ_F . The jet is not symmetric as $\beta \neq 0$, so its direction θ_{jet} is defined in terms of its basement direction as shown in figure 3.20(a) . The jet angle θ_{jet} to the near wall increases with γ_F and approaches $\alpha = \pi/2$ as $\gamma_F \geqslant 10$. The directions of the Kelvin impulse and the jet have excellent agreement.

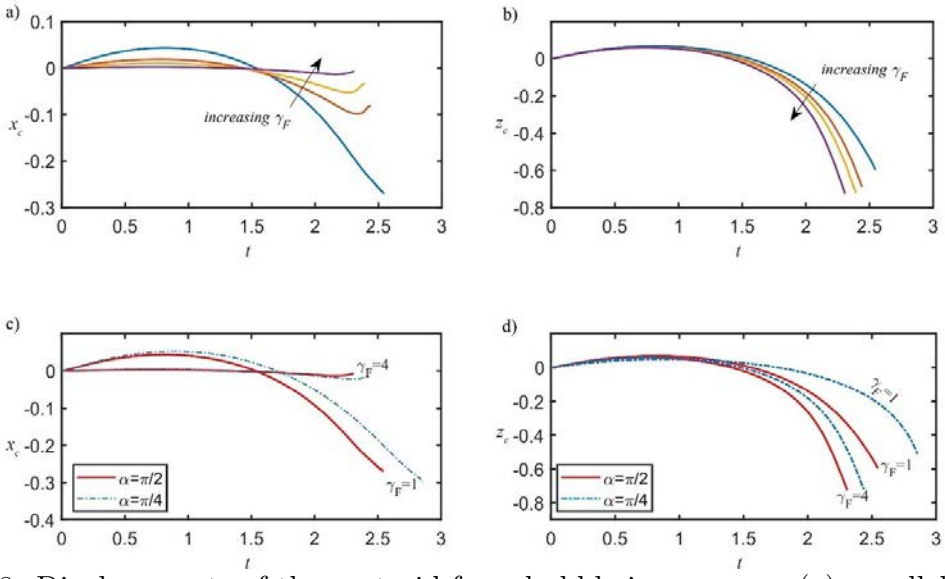

Figure 3.18: Displacements of the centroid for a bubble in a corner: (a) parallel to the near wall, x_c, (b) perpendicular to the near wall, z_c, for $\alpha = \pi/2$,$\gamma_N = 1$ and γ_F =1, 2, 3, 4 respectively; (c) parallel to the near wall, x_c, (d) perpendicular to the near wall, z_c, for $\gamma_N = 1$ and $\gamma_F = 1$, 4, $\alpha = \pi/2$, $\alpha = \pi/4$, for the cases in figures 3.13 and 3.14.

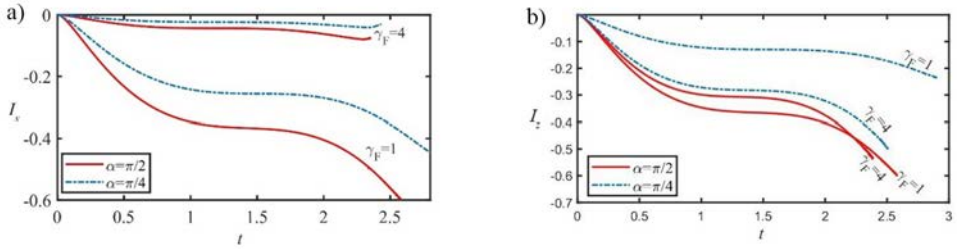

Figure 3.19: Time histories of the Kelvin impulse for the angles $\alpha = \pi/2$, $\alpha = \pi/4$, (a) I_x and (b) I_z , for γ_F =1, 4 for the cases in figures 3.13 and 3.14.

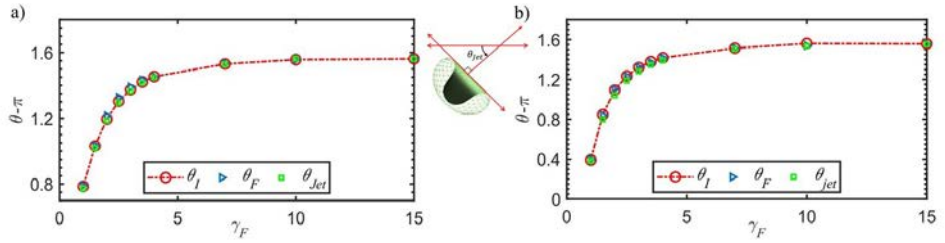

Figure 3.20: Comparison of the directions of the Kelvin impulse θ_F and θ_I, the displacement of the geometrical centre just before the jet impact θ_{jet} , (a) $\alpha = \pi/2$ and (b) $\alpha = \pi/4$ for $\gamma_N = 1$ and $\gamma_F \in [1, 15]$. The remaining parameters are the same as figure 3.14.

3.5 The dynamics of microbubble in a corner

In this section, we consider the simulation for microbubbles having the maximum bubble radius of the size $R_m = 5, 10, 15, 20$, and 25 μm with the corresponding Reynolds number $Re = 49, 99, 149, 199$, and 249 respectively. Rm denotes the maximum bubble radius that the bubble achieves in an infinite domain without viscous and surface tension effects. Here, we consider the viscous pressure correction model which described in chapter 2. Thus, the dynamic boundary condition (3.2.17) on the bubble surface S_B reads as follows

$$\frac{D\varphi}{Dt} = 1 + \frac{1}{2}\big|\nabla\varphi\big|^2 - \varepsilon\Big(\frac{V_0}{V}\Big)^{\kappa} + 2\frac{r_c}{W_e} - 2\frac{(1+C)}{R_e}\psi_n, \tag{3.5.1}$$

where $R_e = R_m\sqrt{\rho\Delta p/\mu}$ is Reynolds number and $W_e = \Delta p R_m/\sigma$ is the Weber number. $\varepsilon = p_0/\Delta p$ is the dimensionless initial pressure of the bubble gas.

For a smaller Reynolds number Re, the maximum bubble radius is achieved and the oscillation period decreases. This is due to the fact that its energy is lost because of viscous effects and surface tension. The energy of a bubble system is lost due to the viscous effects and the acoustic radiation associated with the emission of shockwaves. Shock-waves are emitted at the minimum bubble volumes after bubble jets penetrate bubbles Wang (2016), which are not considered in this work. As the maximum bubble radius decreases, the effectively dimensionless standoff distance from the walls increases and the associated wall effects decreases too. This results in stronger collapse, smaller bubble volume before jet impact, higher jet velocity, less migration of the bubble centroid to the walls and weaker Kelvin impulse.

Each row in figure 3.21 illustrates the bubble shapes at the expansion stage, the maximum volume, jet formation, and jet impact on the opposite bubble surface . The bubble placed at a stand-off distance $\gamma = 1$ in a corner with angle $\alpha = \pi/2$ and for various bubble sizes. The bubble expands approximately spherically (frame 1), until it reaches its maximum volume. Comparing with larger bubbles, which discussed in the previous

sections, there are less effects of the walls on the bubble surface in this stage. The bubble surface is not flattened here due to the effect of the viscosity (frame 2). During the collapse stage, smaller sized bubbles are less attracted to the walls (frame 3). During the latter stages of the collapse, the bubble becomes oblate along the bisector direction, the far side of the bubble opposite to the corner becomes noticeably flattened and a high-speed liquid jet forms pointing to the corner (frames 2 and 3). As the bubble is smaller in size, the bubble volumes at the start of jet formation and jet impact and the width of the jet decrease. The start of jet formation is at the moment when the far side becoming flattened.

Figures 3.22 (a) and 3.22(b) show the time histories of the jet velocity v_{jet} and equivalent bubble radius R_{eq} for the previous cases. For smaller bubbles, the oscillation period decreases and the jet velocity increases as shown in figure 3.22(a). Also, the equivalent radius of the bubble R_{eq} decreases with the bubble size as shown in figure 3.22(b). Moreover, the bubble moves away from the corner during the expansion along the bisector and moves back at a much higher amplitude during the collapse. The migration amplitude decreases with R_m, see figure 3.22(d). These trends are consistent to the time histories of the Kelvin impulse shown in figure 3.22(c). The Kelvin impulse decreases with R_m.

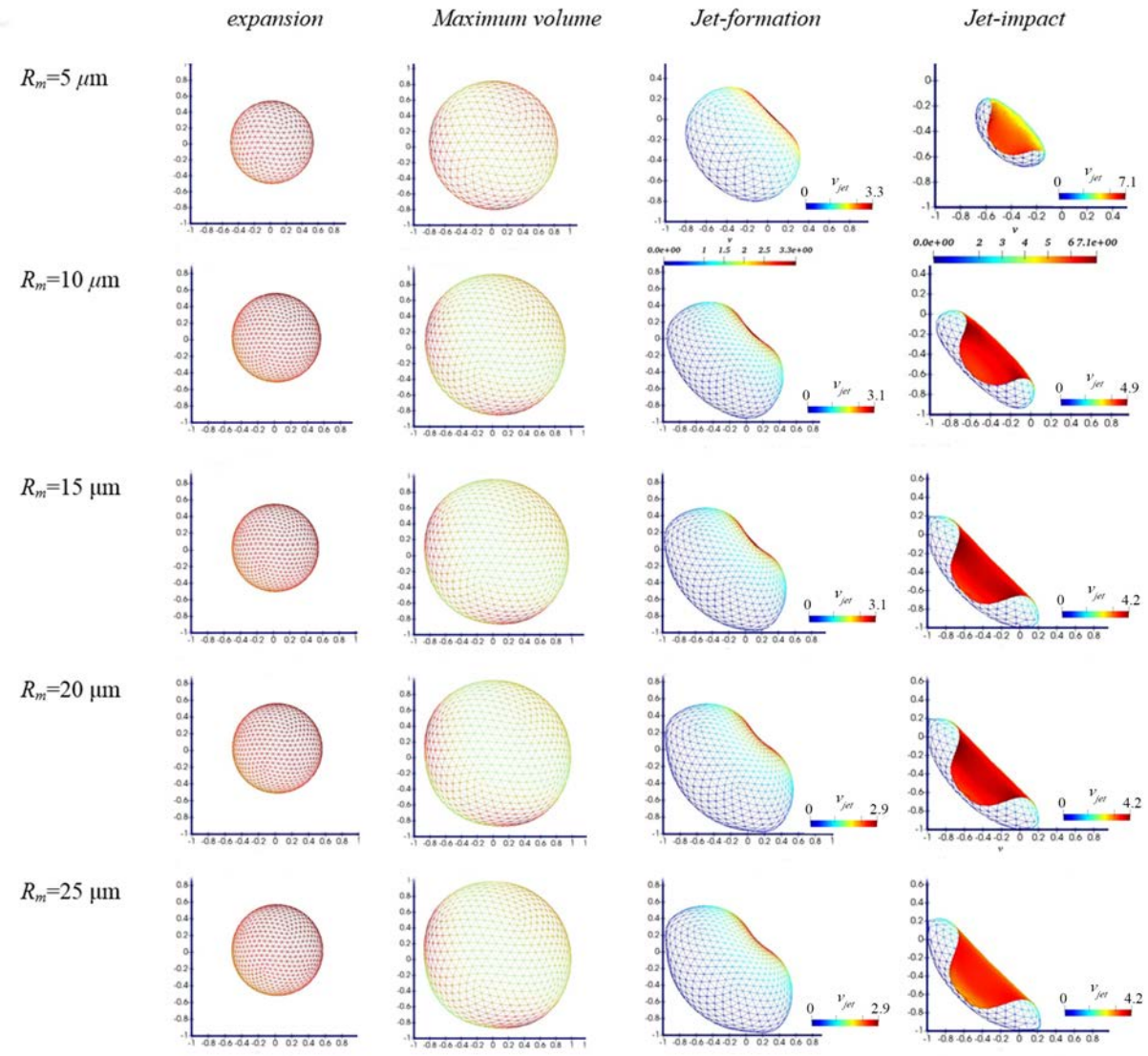

Figure 3.21: Bubble dynamics near a right-angled corner $\alpha = \pi/2$ for various bubble size at $R_m = 5, 10, 15, 20$ and 25μm with the corresponding Reynolds's numbers Re =49, 99, 149, 199, and 249, and Weber numbers $We = 6.8$, 13.5, 20.3, 27.1, and 33.8 respectively. The remaining parameters are set as $\gamma = \gamma_F = \gamma_N = 1$, $\beta = 0$, $\varepsilon = 200$, κ= 1.4.

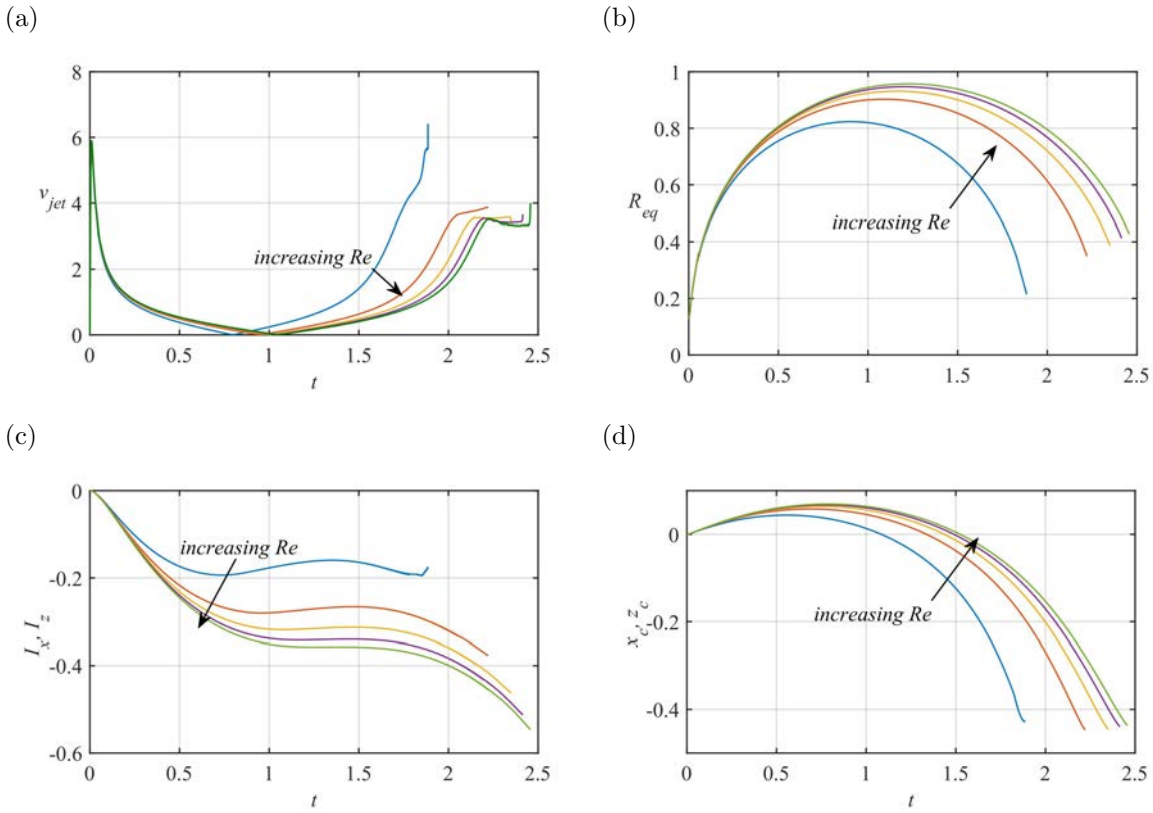

Figure 3.22: Time histories of the (a) jet velocity v_{jet}, (b) the equivalent bubble radius R_{eq}, (c) Kelvin impulse I_x, I_z and (d) displacements of the bubble centroid x_c, z_c for the cases shown in figure 3.21

.

Chapter 4

The interaction between a microbubble and a suspended rigid particle with viscous effects

In this chapter, we will study the microbubble dynamics near a suspended spherical particle based on the potential flow theory coupled with the BIM. The viscous effects in bubble dynamics are not always negligible, for instance, micron-size bubbles and flows with low Reynolds number. Thus, the modified Bernoulli equation including the viscous correction is adopted in this model. Both the bubble and particle surface have meshed into triangular elements. The model is validated by comparing the results with experiment images. Computations and convergence analysis are carried out to demonstrate the robustness of the model.

4.1 Physical, Mathematical and Numerical Modelling

Consider the dynamics of a microbubble near a spherical particle of radius R_p and mass m_p. The particle has an eccentricity E from the axis of the symmetry ($x = 0$). Initially, a spherical bubble is at an equilibrium radius R_0 with its centre positioned at the centre of the configuration (see figure 4.1). A Cartesian coordinate system $O - xyz$ is adopted with the origin at the centre of the bubble.

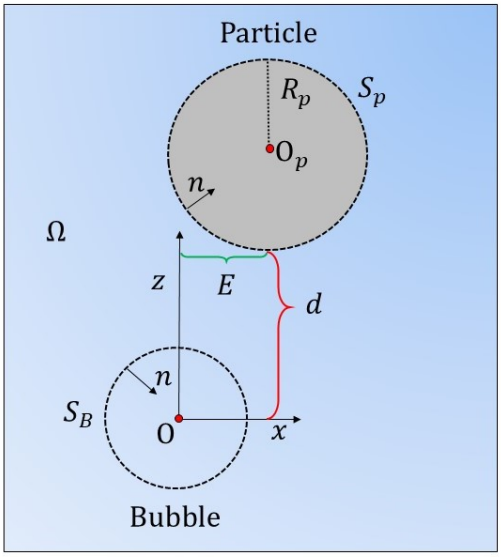

Figure 4.1: Configuration and coordinate system for bubble-particle interaction.

The fluid is assumed to be incompressible and inviscid, and the flow is irrotational. The fluid velocity $\boldsymbol{v}$ thus has a potential of φ ($\boldsymbol{v} = \nabla\varphi$) that satisfies Laplace's equation ($\nabla^2\varphi = 0$) which has an integral form as follows

$$c(\boldsymbol{r}, t)\varphi(\boldsymbol{r}, t) = \int_S \left[\psi(\boldsymbol{q}, t)G(\boldsymbol{r}, \boldsymbol{q}) - \varphi(\boldsymbol{q}, t)\frac{\partial G(\boldsymbol{r}, \boldsymbol{q})}{\partial n}\right] dS(\boldsymbol{q}), \tag{4.1.1}$$

where $\boldsymbol{r}$ is the control point and $\boldsymbol{q}$ is the source point, c is the solid and angle, S is the flow boundary which consists of the bubble surface S_B and the particle surface S_p. The infinite-space Green's function $G(\boldsymbol{r}, \boldsymbol{q})$ for Laplace's equation is defined as follows

$$G(\boldsymbol{r}, \boldsymbol{q}) = \frac{1}{|\boldsymbol{r} - \boldsymbol{q}|}. \tag{4.1.2}$$

The non-dimensionalisation is performed using R_m as the length scale, ρ_L as the density scale, and $\Delta p = p_\infty - p_v$ as the pressure scale, where p_∞, p_v are the ambient pressure and the vapour pressure, respectively. Other quantities are scaled with the

above parameters, asterisk represent the dimensionless variables, as follows

$$\begin{aligned}
\boldsymbol{r^*} &= \boldsymbol{r}/R_m, \quad t^* = t/(R_m\sqrt{\rho_L/\Delta p}), \\
dS^* &= R_m^2 dS, \quad \varphi^* = \varphi/(R_m\sqrt{\rho_L/\Delta p}), \\
\boldsymbol{a}_p^* &= R_m\Delta p/\rho_L \boldsymbol{a}_p, \quad \rho_p^* = \rho_p/\rho_L, \\
\boldsymbol{u}_p^* &= \boldsymbol{u}_p/\sqrt{\Delta p/\rho_L}, \quad R_p^* = R_p/R_m, \\
m_p^* &= m_p/(R_m^3\rho_L), \text{ for } \; m_p = 4\pi/3\rho_p R_p^3, \\
W_e &= \sigma/(R_m\Delta p), R_e = R_m\rho_L\sqrt{\Delta p/\rho_L}/\mu,
\end{aligned} \tag{4.1.3}$$

where ρ_L is the liquid density, $m_p, \boldsymbol{a}_p, \rho_p$, and $\boldsymbol{u}_p$ are the mass, acceleration, density and the velocity of the particle. The scaling values are taken as $p_\infty = 101$ kPa, $p_v = 2.3$ kPa and $\rho_L = 1000$ kg m^{-3}. Dimensionless variables are used without stars in the remaining text unless stated otherwise. The dimensionless eccentricity of the particle is $\xi = E/R_m$, and the standoff distance γ is calculated from the centre of the initial bubble to the surface of the particle, and it is given by

$$\gamma = \frac{d}{R_m}. \tag{4.1.4}$$

The cases considered correspond to microbubbles, therefore the buoyancy effects are negligible, i.e. $\delta = 0$, unless explicitly stated otherwise. Also, the eccentricity has no effect on the dynamics of the microbubbles, i.e $\xi = 0$.

By using the modified Bernoulli equation (2.3.51) as described in Chapter 2, the dimensionless dynamic boundary condition on the bubble surface S_B can be expressed as

$$\frac{D\varphi}{Dt} = 1 + \frac{1}{2}\big|\nabla\varphi\big|^2 - \delta^2 z - \varepsilon\Big(\frac{V_0}{V}\Big)^\kappa + 2\frac{r_c}{W_e} - 2\frac{(1+C)}{R_e}\psi_n. \tag{4.1.5}$$

The kinematic boundary conditions on the particle surface S_p, bubble surface S_B, and at

infinity are as follows

$$\frac{\partial \varphi}{\partial n} = \boldsymbol{u}_p \cdot \boldsymbol{n} \text{ on } S_p, \tag{4.1.6a}$$

$$\frac{D\boldsymbol{r}}{Dt} = \nabla\varphi \text{ on } S_B, \tag{4.1.6b}$$

$$\nabla\varphi \to 0, \text{as } r \to \infty, \tag{4.1.6c}$$

where $\boldsymbol{r}$ is the position vector of the boundary, $\boldsymbol{n}$ is normal on the boundary surface, D/Dt denotes the material derivative, and r is the radial distance. Equations (4.1.6a) and (4.1.6b) refer to the impermeable boundary condition on the rigid boundaries and that the material points on the bubble surface remain there, respectively.

The non-uniform time steps have been chosen sensibly in each iteration for the procedure to avoid any instability as below

$$\Delta t = \frac{\Delta\varphi}{\max\limits_i \left(D\varphi_i/Dt \right)}, \tag{4.1.7}$$

where $\Delta\varphi$ is a constant and it chosen as 0.001 in this work, φ_i is the potential of the vertex i on the bubble surface.

4.2 Modelling the bubble dynamics on a suspended particle

To simulate this model, a bubble and a spherical particle are placed along the z-axis (see figure 4.1). Newton's second law governs the motion of the particle as follows

$$\boldsymbol{F} = \boldsymbol{F}_g + \boldsymbol{F}_h = m_p \boldsymbol{a}_p, \tag{4.2.1}$$

where the quantities m_p and $\boldsymbol{a}_p$ are mass and acceleration of the particle, $\boldsymbol{F}_g$ is an external force (e.g., the force due to gravity) and $\boldsymbol{F}_h$ is a hydrodynamic force which acts on the

particle and can be obtained by integrating the pressure over its wetted surface S_p. The non-dimensional forms of $\boldsymbol{F}_h$ is as follows

$$\boldsymbol{F}_h = -\iint_{S_p} \Big(\dot{\varphi} + \frac{1}{2}|\nabla\varphi|^2 + \delta^2 z - 1\Big)\boldsymbol{n}\; dS(\boldsymbol{q}). \tag{4.2.2}$$

The term $\dot{\varphi} = \partial\varphi/\partial t$ in the above equation is unknown even if the velocity potentials on all the boundaries of the flow domain are obtained. The backward finite difference approximation is often adopted to calculate $\dot{\varphi}$. However, it may result in unacceptable errors, due to very small time-steps which are usually used in simulating a violent collapsing bubble. The boundary value problem of $\dot{\varphi}$ can be obtained as follows $\Delta\dot{\varphi} = 0$ with

$$\begin{aligned}
\dot{\varphi} &= 1 - \frac{1}{2}\big|\nabla\varphi\big|^2 - \delta^2 z - \varepsilon\Big(\frac{V_0}{V}\Big)^{\kappa} && \text{(4.2.3a)}\\
&\quad + 2\frac{r_c}{W_e} - 2\frac{(1+C)}{R_e}\psi_n \quad \text{on } S_B,\\
\dot{\psi} &= -\boldsymbol{u}_p \cdot \frac{\partial}{\partial n}\nabla\varphi + \boldsymbol{a}_p \cdot \boldsymbol{n} \quad \text{on } S_p, && \text{(4.2.3b)}\\
\nabla\dot{\varphi} &\to 0 \text{ as } r \to \infty. && \text{(4.2.3c)}
\end{aligned}$$

$\dot{\varphi}$ can be obtained once the velocity potential of the flow domain is solved. However, $\dot{\psi}$ cannot be determined in a straightforward manner. Wu and Hu (2004) used auxiliary functions to simulate the interaction between water waves and a floating body. Following them, Li, Han and Zhang (2016); Li et al. (2019) used the same method to simulate the nonlinear interaction of a bubble and spherical particle. This can be achieved by introducing several auxiliary functions, which satisfy the Laplace's equation $\Delta\varphi = 0$.

Noticing the closed problem (4.2.3a-c) is linear and by setting $\dot{\varphi} = \Phi + \Psi$, we have

$\Delta\Phi = 0$, and

$$\Phi = 1 - \frac{1}{2}\left|\nabla\varphi\right|^2 - \delta^2 z - \varepsilon\left(\frac{V_0}{V}\right)^{\kappa} + 2\frac{r_c}{W_e} - 2\frac{(1+C)}{R_e}\psi_n \text{ on } S_B, \tag{4.2.4a}$$

$$\frac{\partial\Phi}{\partial n} = -\boldsymbol{u}_p \cdot \frac{\partial}{\partial n}\nabla\varphi \text{ on } S_p \tag{4.2.4b}$$

$$\nabla\Phi \to 0 \text{ as } r \to \infty. \tag{4.2.4c}$$

Furthermore, Ψ satisfies the Laplace's equation, $\Delta\Psi = 0$ and

$$\Psi = 0 \text{ on } S_B, \tag{4.2.5a}$$

$$\frac{\partial\Psi}{\partial n} = \boldsymbol{a}_p \cdot \boldsymbol{n} \text{ on } S_p, \tag{4.2.5b}$$

$$\nabla\Psi \to 0 \text{ as } r \to \infty. \tag{4.2.5c}$$

With this information, Φ is solvable using BIM (4.1.1) after replacing φ by Φ. However, it is not necessary to solve the system (4.2.5) for Ψ. Furthermore, another auxiliary function Υ is introduced that also satisfies the Laplace's equation, $\Delta\Upsilon = 0$ as follows

$$\Upsilon = \Phi + \nabla\varphi \cdot \boldsymbol{u}_p, \tag{4.2.6}$$

with the following boundary conditions

$$\Upsilon = \nabla\varphi \cdot \boldsymbol{u}_p + \dot{\varphi} \text{ on } S_B,$$

$$\frac{\partial\Upsilon}{\partial n} = 0 \text{ on } S_p, \tag{4.2.7a}$$

$$\nabla\Upsilon \to 0 \text{ as } r \to \infty. \tag{4.2.7b}$$

Similarly, Υ is solvable using BIM (4.1.1) after replacing φ by Υ. Substituting (4.2.6) in

to (4.2.2) yields

$$\boldsymbol{F}_h = -\iint_{S_p} \Big(\Upsilon - \nabla\varphi \cdot \boldsymbol{u}_p + \frac{1}{2}|\nabla\varphi|^2 + \delta^2 z - 1\Big)\boldsymbol{n}\; dS - \iint_{S_p} \Psi \boldsymbol{n}\; dS. \tag{4.2.8}$$

There are an additional three auxiliary functions that are needed in order to deal with the last term of equation (4.2.8). Thus, Λ_x, Λ_y, and Λ_z are defined such that $\Psi = a_x\Lambda_x + a_y\Lambda_y + a_z\Lambda_z$. The introduced functions can be solved in the same manner as φ using the following boundary conditions

$$\Lambda_x = 0, \quad \Lambda_y = 0, \quad \Lambda_z = 0 \;\text{ on } S_B, \tag{4.2.9a}$$

$$\frac{\partial \Lambda_x}{\partial n} = n_x, \quad \frac{\partial \Lambda_y}{\partial n} = n_y, \quad \frac{\partial \Lambda_z}{\partial n} = n_z \;\text{ on } S_P. \tag{4.2.9b}$$

Finally, the non-dimensional form of (4.2.1) reads

$$m_p \boldsymbol{a}_p = \tag{4.2.10}$$
$$-\iint_{S_P} \Big(\Upsilon - \nabla\varphi \cdot \boldsymbol{u}_p + \frac{1}{2}|\nabla\varphi|^2 + \delta^2 z - 1\Big)\boldsymbol{n}\; dS - \iint_{S_P} \Psi \boldsymbol{n}\; dS - \delta^2 m_p \boldsymbol{k}.$$

In this stage, the value of all the quantities are obtained and thus the sphere acceleration $\boldsymbol{a}_p$ can be solved directly. The closed problem (4.2.3a-c) can then be updated in a straightforward manner.

4.3 Validation of the numerical model and Convergence study

4.3.1 Comparison with experiments

To evaluate the BIM model, firstly, we compare the computational results with experimental images of an interaction of a bubble with a fixed solid sphere. The bubble is generated in a 300 mm cubic glass water tank by a discharge of a capacitor and the par-

ticle has a radius of $R_p = 14$ mm. The maximum radius of the bubble, R_m, is determined by the discharge voltage, which varied between 16±0.5 mm in the experiments. Images of bubbles are recorded by a VRI-Phantom V611 high-speed camera at 180 kfps.

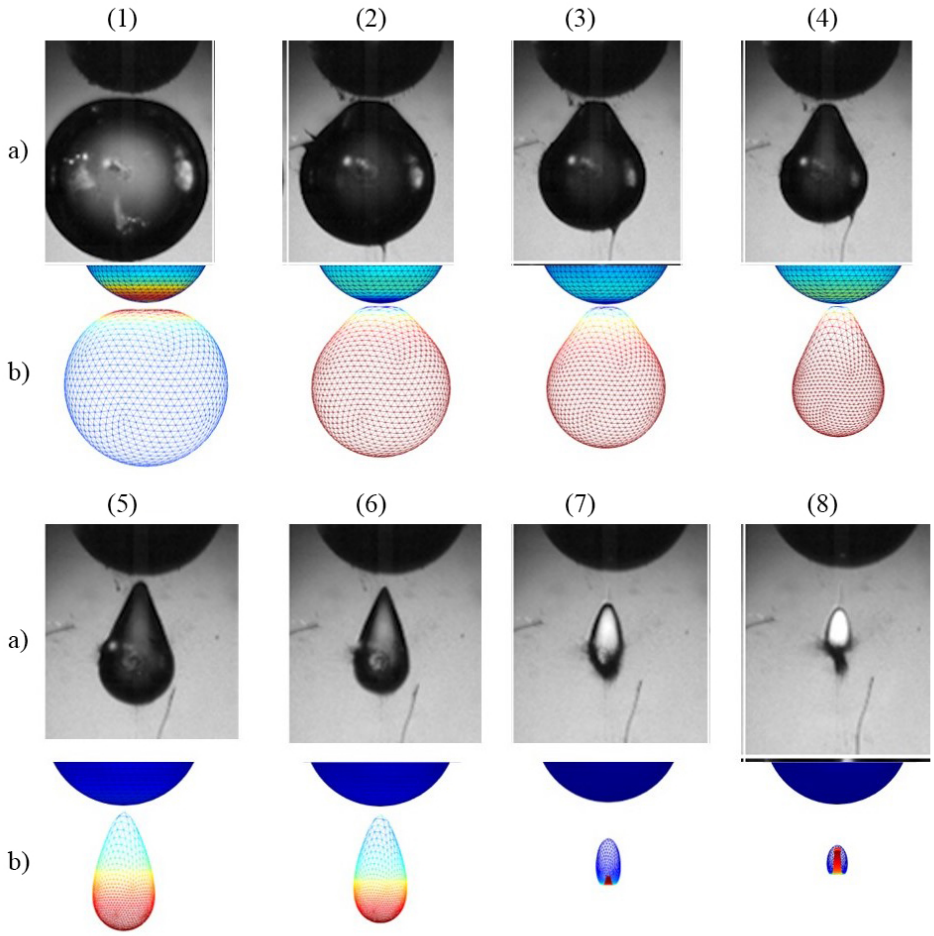

Figure 4.2: Bubble behaviour near a fixed solid sphere (a) experiment and (b) current study, $\gamma = 0.94$, $R_m = 16$ mm, $R_p = 0.87R_m$, $\delta = 0.04$, $\kappa = 1.4$, $W_e = 21000$, $R_e = 1.5e6$. The dimensionless times are as follows;
$t = 1.0369, 1.62, 1.77, 1.87, 1.93, 1.98, 2.0, 2.023$, respectively.

Figure 4.2 shows a case with $\gamma = 0.94$ for a bubble with maximum size $R_m = 16$ mm placed under a sphere with a radius of $R_p = 0.87$. The bubble is approximately spherical during the expansion stage until it reaches to its maximum volume. In this stage, the bubble's top surface is flattened by the particle (frame 1). Next, at the early stage of the contraction, the bubble becomes non-spherical and the top surface of the bubble is

drawn in by the spherical solid surface (frame 2-3). The bubble then starts to elongate along the z-axis due to lower velocity in that area (frame 4-5). The far side of the bubble starts to protrude towards the particle (frame 5-6). Subsequently, a high-speed jet starts to form in that area and pierces through the bubble, similar to the bubble collapse near a flat wall (frame 7-8).

The second case is for a suspended particle with radius $R_p = 1.045$, $\rho_p = 1.2$ initiated above a bubble with maximum radius $R_m = 19.1$ mm, i.e. the particle has a higher density compared with the water. The remaining parameters are $\delta = 0.043, \kappa = 1.4, \varepsilon = 200$, $W_e = 25900$, $R_e = 1.8e5$. Figure 4.3 shows the comparison between the bubble shape obtained from experimental images and axisymmetric results by (Liu, Wang and Zhang, 2016) with the current 3D model. The bubble shape during its expansion, maximum volume, collapse stage, jet formation and just before the jet impacts are presented in figure 4.3, frames (1-5), respectively. The bubble remains spherical at the early expansion stage (frame 1). Meanwhile, due to the bubble expansion, the particle is pushed upward as seen in figure 4.4. When the bubble reaches its maximum volume, the upper surface of the bubble gets flattened by the particle (frame 2) and the particle becomes motionless. The particle then starts moving downward as the pressure above the particle is higher than the pressure under and above the bubble. Therefore, the collapsing bubble will pull the particle downward and as the bubble is retarded by the particle, the bubble collapses faster in the x-direction than the z-direction. Consequently, the bubble becomes elongated and a high velocity zone starts to form on the far side of the bubble from the particle (frame 3-4). Finally, that high-pressure zone forms a thin jet towards the particle and penetrates the opposite side of the bubble (frame 4). Moreover, the bubble moves away in the early stage of the expansion and then starts moving towards the particle in the expansion stage as shown in figure 4.4.

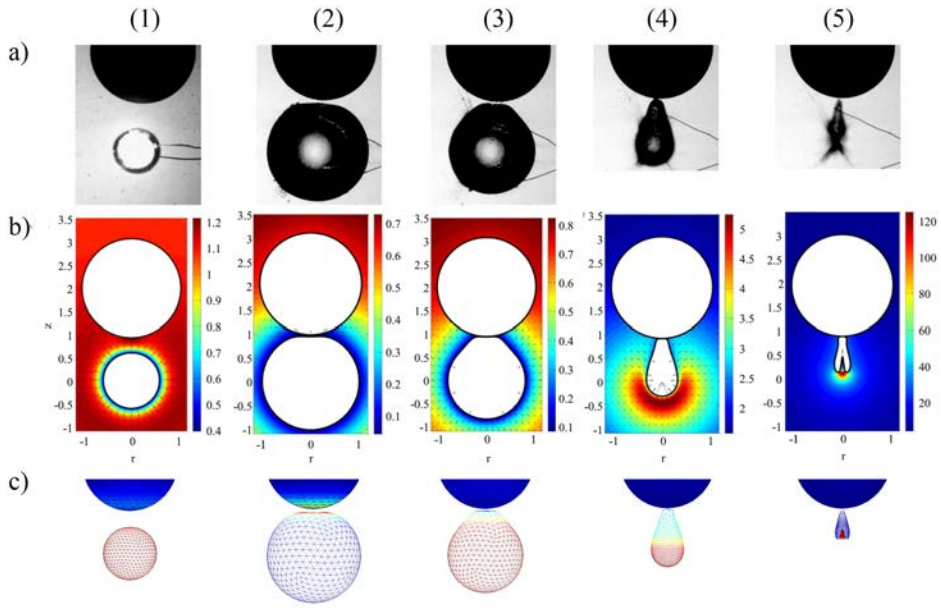

Figure 4.3: A comparison between of bubble behaviour near a suspended solid sphere (a) experiment, (b) axisymmetric results by (Liu, Wang and Zhang, 2016), and (c) current study, 3D BIM. The non-dimensional times are $t = 0.161$, 0.989, 1.519, 1.88, and 1.93, respectively. $\gamma = 0.92$, $R_m = 19.1$ mm, particle radius $R_p = 1.045$, $\rho_p = 1.2\rho_L$ $\delta = 0.043$, $\kappa = 1.4$, $W_e = 25900$, $R_e = 1.8e5$.

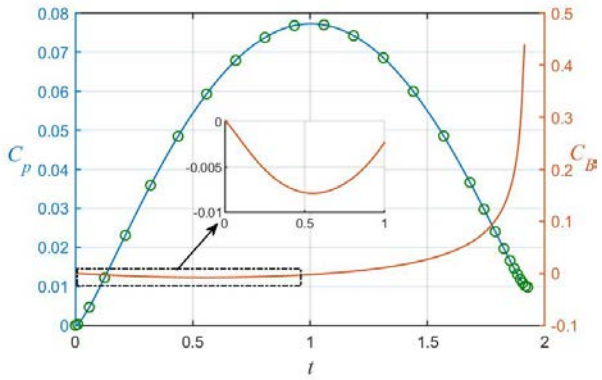

Figure 4.4: The time history of the particle centroid displacement, in $z-$direction, C_p (blue-solid line), and the bubble centroid movement C_B (red-solid line) in $z-$direction, compared with the results obtained by (Liu, Wang and Zhang, 2016) (green circles), for the case in figure 4.3.

4.3.2 Convergence study

In this section, to analyse the convergence of our 3D-BIM for bubble-particle interaction, convergence tests are performed considering bubble and particle element sizes. Firstly,

the bubble surface is fixed at $M_B = 1280$ elements and we perform convergence tests to pack a suitable element numbers on the particle surface. Different element numbers on the particle surface are taken as, $M_p = 500, 980$ and 1620. Figure 4.5 depicts a comparison between the particle centroid C_P displacement (blue-line) and the bubble centroid movement C_B for different particle elements. The result emphasises that the particle element size does not affect the dynamics of the bubble or the particle movement. This may result from the calculation of the mass of the particle in equation (4.2.1) which is performed using the physical radius R_p and not the particle geometry. The particle element size may effect the results only when the bubble is attached to the particle during the expansion stage (Li et al., 2019). Therefore, we perform the rest of the calculations with particles of element size $M_p \in [980, 1620]$.

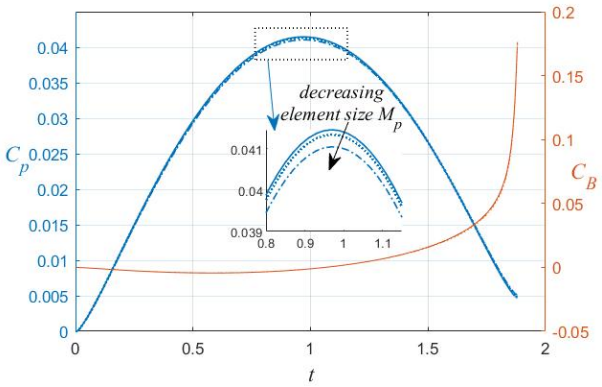

Figure 4.5: A comparison of the particle centroid movement C_p (blue lines), and the bubble centroid movement C_B (red lines) in the $z-$direction. Bubble surface element size is fixed at 1280, and various particle elements are taken as $M_p = 500, 980$, and 1620. The remaining parameters are $\gamma = 1.2$, $\rho_p = 2$, $R_m = 50\mu$m, $R_p = 1$, $\delta = 0.04$, $\varepsilon = 200$, $W_e = 68$, $R_e = 496$, $\kappa = 1.4$.

To verify the effect of the bubble element size on the dynamics of the 3D-BIM bubble-particle interaction, we perform the simulations by fixing the particle element size at $M_P = 980$, and perform the calculations with different bubble element sizes at $M_B = 1280, 2000, 2880$, and 3920. Figure 4.6 shows a comparison between bubble shapes at time $t = 1.91$ just before the jet impact. At the bubble bottom, a sharp upward liquid jet forms with high-mesh density around the jet. The results of the 3D model become

identical with increasing the element size on the bubble surface M_B.

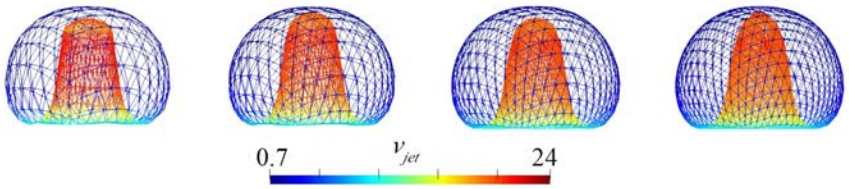

Figure 4.6: A comparison of bubble shapes just before the jet impact t = 1.91. The particle surface element size is fixed at 980, and various bubble elements are taken as $M_p = 1280, 2000, 2880$ and 3920. The remaining parameters are $\gamma = 1.5$, $\rho_p = 4$, $R_m = 50\mu$m, $R_p = 3$, $\delta = 0.04$, $\varepsilon = 200$, $W_e = 68$, $R_e = 496$, $\kappa = 1.4$.

More investigation is undertaken in order to choose a suitable bubble element size by comparing the bubble jet velocity v_{jet}, equivalent bubble radius R_{eq}, bubble centroid movement C_B and particle displacement C_p. Figure 4.7(a) shows the time histories of the jet velocity for the same case in figure 4.6. There is insignificant change in the jet velocity pick while we increase the bubble mesh size. Also, the effect of the mesh size on the bubble maximum radius and the bubble life time is increase slightly with increasing M_B (see figure 4.7(b)). The same effects are observed in the bubble and particle movement as shown in figures 4.7(c) and (d). As a result, for the rest of calculations and for accuracy, the bubble element size is chosen as $M_B \in [2000, 2880]$.

4.4 Numerical results

4.4.1 The effects of stand-off distance γ

Similar to the bubble dynamics near a rigid wall, the stand-off parameter γ plays an important role in the dynamics of the bubble-particle model. To investigate the effect of γ, the particle size and its density are fixed at radius $R_p = 1$, and $\rho_p = 2$, respectively. Various values of γ are taken as $\gamma = 1, 1.5, 2$, and 2.5. The remaining parameters are $R_m = 50\mu$m, $\delta = 0.04$, $\varepsilon = 200$, $W_e = 68$, $R_e = 496$, $\kappa = 1.4$. Figure 4.8 shows the bubble shape just before the jet impact for the case $\gamma = 1$ and 1.5. The bubble is almost

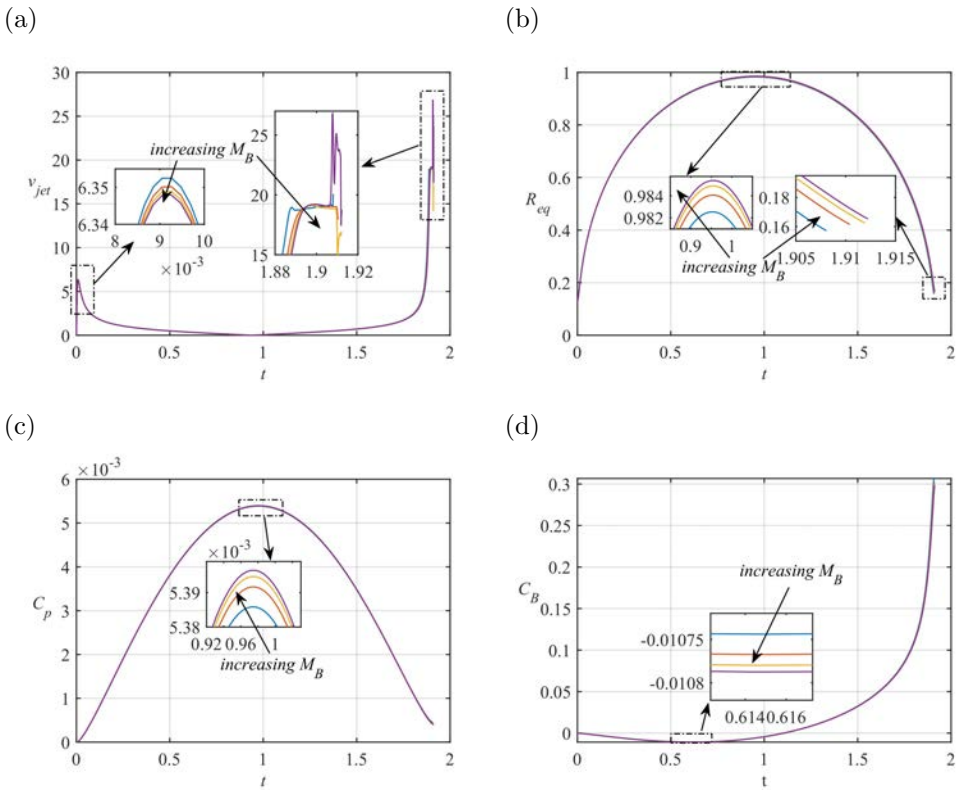

Figure 4.7: A convergent study for the time history of the (a) jet velocity v_{jet}, (b) equivalent bubble radius R_{eq}, (c) particle centroid movement C_p, and (d) bubble centroid movement C_B. Particle surface element size is fixed at 1280, and various bubble elements are taken as $M_p = 500, 980$, and 1620. The remaining parameters are the same as figure 4.6.

spherical during its expansion when the bubble placed at a distance $\gamma \geqslant 1.5$. When the bubble reaches the maximum volume, the bubble surface near the particle gets flattened for the case $\gamma = 1$ otherwise it is almost spherical. During the collapse stage, the near bubble surface to the particle is almost motionless as it is retarded by the particle (see figures 4.8a and b). As a result, the bottom part of the bubble moves faster and the bubble becomes elongated for the case $\gamma = 1$ (see figure 4.8c). Finally, that high-pressure zone forms a thin jet towards the particle and penetrates the opposite side of the bubble (see figure 4.8d).

Figure 4.9 compares the displacement of the particle centroid C_p and bubble centroid C_B in the $z-$direction for the same case in figure 4.8. Here, for the particle, $C_p(t) =$

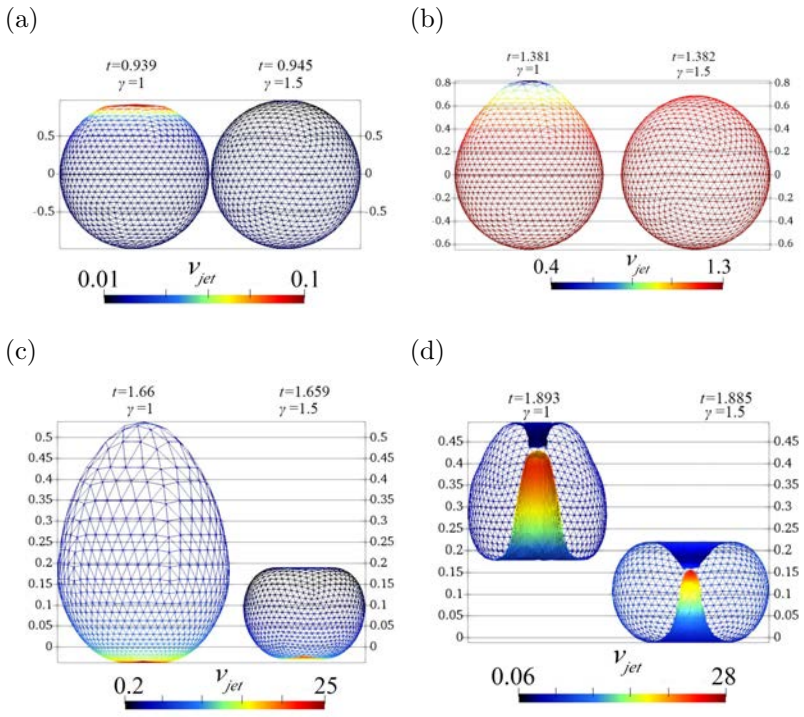

Figure 4.8: The bubble shapes at (a) maximum volume, (b) early stage of collapse, (c) jet formation, and (d) just before the jet impact, for stand-off distances $\gamma = 1, 1.5$ respectively. The remaining parameters are $\rho_p = 2$, $R_m = 50\mu$m, $R_p = 1$, $\delta = 0.04$, $\varepsilon = 200$, $W_e = 68$, $R_e = 496$, $\kappa = 1.4$.

$C_p(0) - \gamma - R_p$, where $C_p(0)$ is the initial location of the particle. As expected, the bubble and the particle depart further during the expansion stage and retract toward each other in the collapse stage. The displacement as well as the bubble lifetime are reduced with increasing γ. The stand-off distance γ also has an impact on the bubble centroid motion. The bubble moves more towards a particle having a distance of the maximum bubble radius. The bubble moves away from the particle in the expansion stage when the bubble is placed closer to the particle as shown in figure 4.8. Also, when $\gamma \geqslant 1.5$ the bubble starts to rebound as the jet velocity decreases. Subsequently, the jet penetrates the far side of the bubble in the second or even higher oscillation cycles. Figure 4.10 illustrates the effect of γ on the equivalent bubble radius R_{eq} and the jet velocity v_{jet}. The maximum volume decreases with decreasing γ as well as the jet velocity. The results were also compared with the RPE for a bubble at infinity and they agreed well.

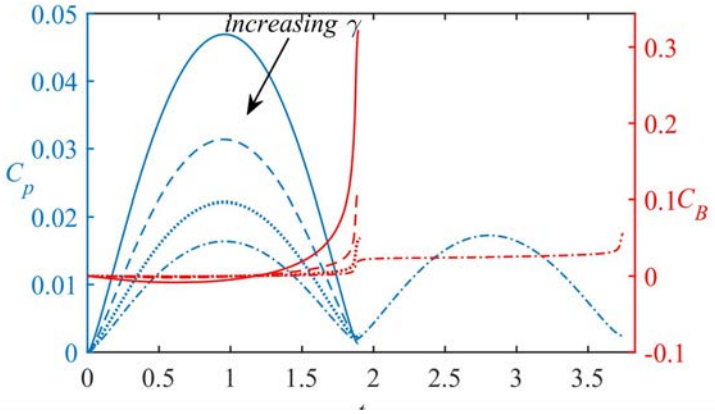

Figure 4.9: The time history of the particle centroid displacement C_p (blue lines), and the bubble centroid movement C_B (red lines) in $z-$direction for the same case in figure 4.8.

Further analysis can be seen in figure 4.11(a) and (b). Figure 4.11(a) shows the time histories of the Kelvin impulse. The z-component of the Kelvin impulse I_z of the bubble decreases rapidly with increasing γ. Also, the particle velocity u_p, in the z-direction, decreases with γ and has different patterns during the bubble life time. It increases in the early stage of the expansion and starts reducing to zero when the bubble reaches its maximum volume. The particle velocity reduces more during the collapse stage and obtains a negative value. By the end stage of the collapse stage, at the time of the jet formation, the particle velocity starts to increase again as shown in figure 4.11(b).

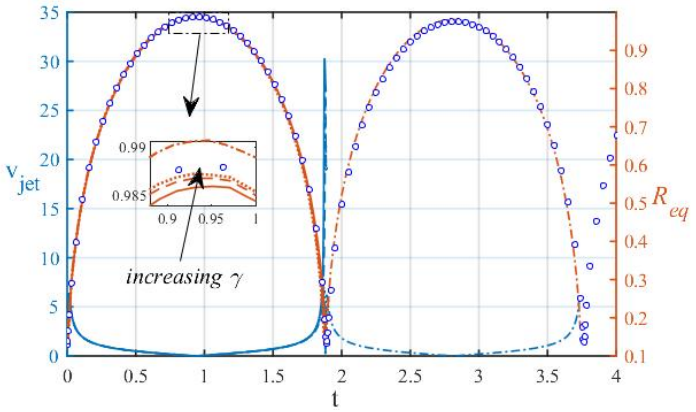

Figure 4.10: A comparison between Rayleigh-Plesset equation (RPE, circles), and the time history of the equivalent bubble radius R_{eq} (red lines), and the jet velocity v_{jet} (blue lines) for same simulations as in figure 4.8.

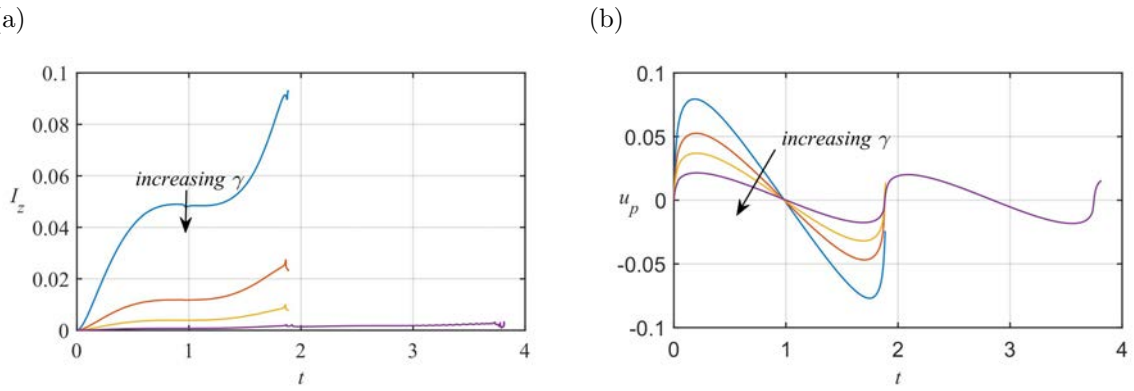

Figure 4.11: The time history of the (a) Kelvin impulse in the $z-$direction, and (b) particle velocity, for same simulations as in figure 4.8.

4.4.2 The effects of the particle density ρ_p

In this section the effect of the particle density ρ_p is considered. The particle placed at $O_p = (0, 0, 1.2)$ is situated on the top of a bubble. The particle size is fixed at $R_p = 1$ and the bubble has it is maximum radius of $R_m = 50\mu$m. Particle densities are chosen as $\rho_p = 0.5, 1, 3, 5$, and 7. The remaining parameters are $\gamma = 1.2$ $R_m = 50\mu$m, $R_p = 1$, $\delta = 0.002$, $\varepsilon = 200$, $W_e = 68$, and $R_e = 496$.

Figure 4.12 illustrates the bubble shape at inception, maximum volume, jet formation and the shape just before the jet impact. The bubble is almost spherical during its expansion in all the cases and no contact occurs between the bubble and the particle. Consequently, a higher curvature region occurs on the top of the bubble surface and it becomes flattened due to the effect of the particle being held back. During its collapse, the top surface of the bubble is held back by the particle and the bubble has an egg shape afterwards as shown in figure 4.12(a). However, the highest local curvature occurs on the bubble's bottom surface which leads to the formation of an upward jet making a collision with the weak downward jet from the top surface as shown in figure 4.12(b). The upward jet velocity reaches $v_{jet} \approx 32$ while the downward jet has its maximum value at $v_{jet} \approx 6.3$, which is about 5 times less than the upward jet. For $\rho_p < 1$, the bubble start to rebound at the end of the collapse stage and the downward jet has a greater impact

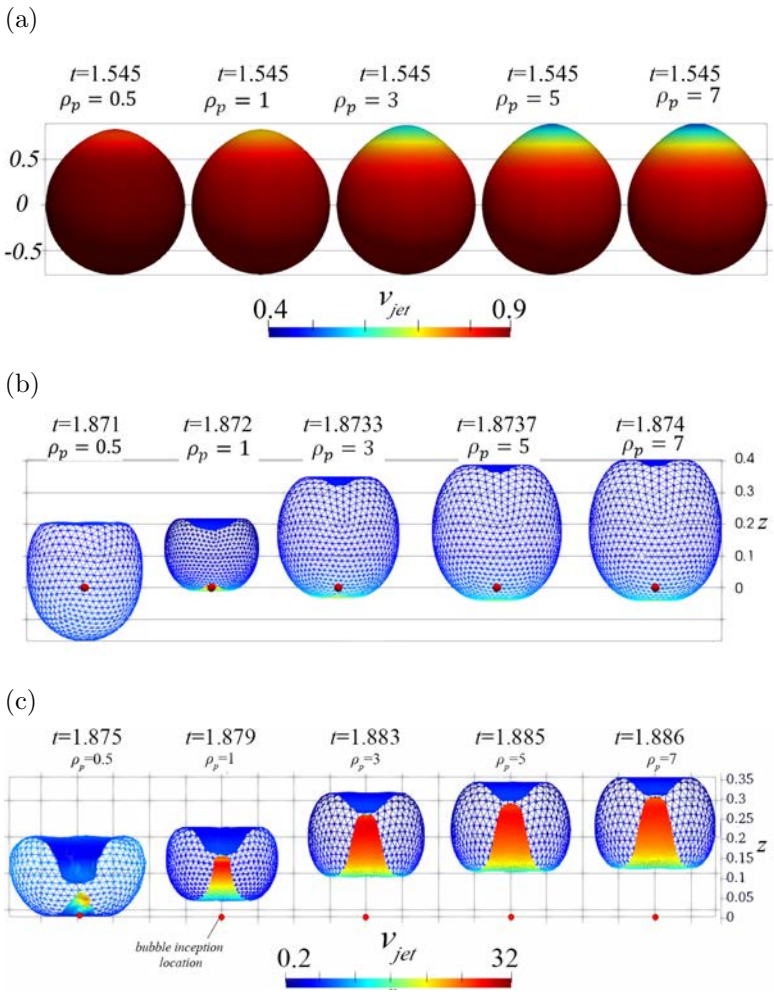

Figure 4.12: Bubble shapes at (a) early stage of the collapse stage (b) bubble shape at the jet formation, and (c) just before the jet impact, for various values of particle densities, $\rho_p = 0.5, 1, 3, 5$, and 7. The remaining parameters are $R_m = 50\mu$m, $\gamma = 1.2$, $R_p = 1$, $\delta = 0.002$, $\varepsilon = 200$, $W_e = 68$, $R_e = 496$, and $\kappa = 1.4$.

than the upward jet on the bubble shape. Figure 4.13 compares the displacement of the particle centroid C_p and bubble centroid C_B in the $z-$direction. As expected, the bubble and the particle depart further during the expansion stage and retract toward each other in the collapse stage. The movement decreases with increasing ρ_p. The particle density also has an impact on the bubble centroid motion. The bubble is attracted towards a particle having greater density. The bubble moves further away from the particle in the expansion stage due to the particle having a higher density.

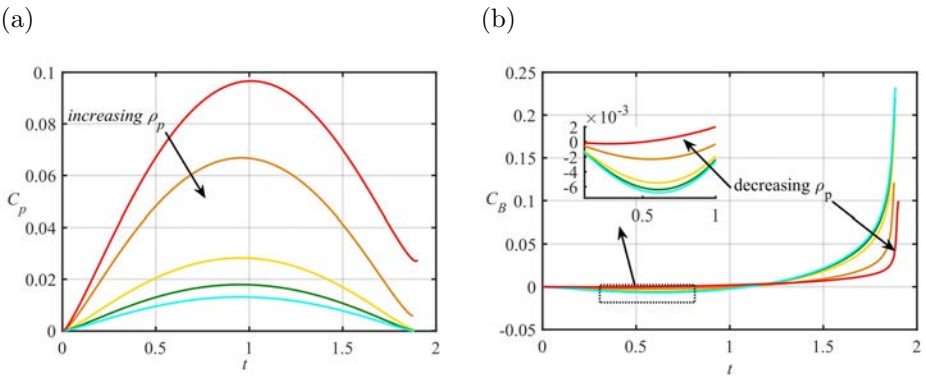

Figure 4.13: The time history of the (a)particle centroid displacement C_p, and (b) the bubble centroid displacement C_B in the $z-$direction for various values of particle densities, $\rho_p = 0.5, 1, 3, 5$, and 7. The remaining parameters are the same as figure 4.12.

Figures 4.14(a) and (b) show the time histories of the equivalent bubble radius R_{eq} and the bubble upward jet velocity v_{jet}, respectively. Another consequence of the particle density is on the bubble size at the jet impact as well as the impact time. The bubble size at jet impact R_{imp} and the impact time t_{imp} increase with increasing ρ_p as shown in figures 4.13 and 4.14(a). Also, the jet velocity v_{jet} at the impact time increase inversely with increasing ρ_p as shown in figure 4.14(b).

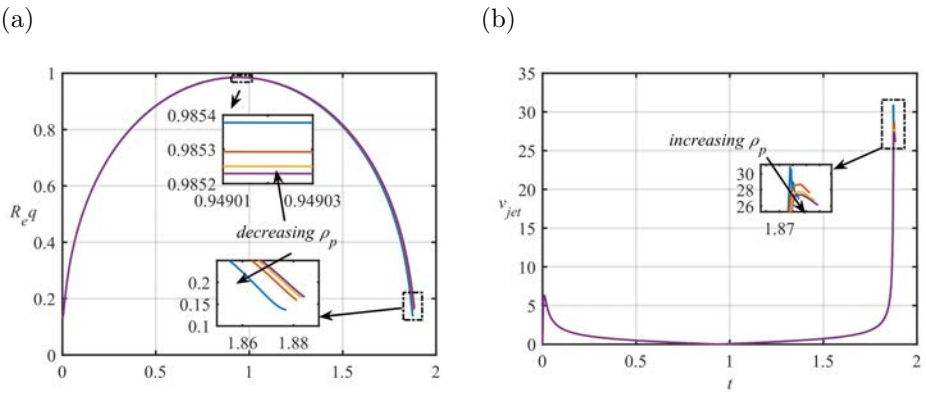

Figure 4.14: The time history of the (a) equivalent bubble radius R_{eq}, and (b) jet velocity v_{jet}, for the cases in figure 4.12.

Figure 4.15(a) illustrates the time history of the particle velocity u_p in the $z-$direction for various values of particle densities, $\rho_p = 0.5, 1, 2, 3$, and 4. The particle has a positive

velocity during the expansion stage and negative velocity during the collapse. This reiterates the previously mentioned outcomes which suggested that the particle moves away and retracts during these two stages. At the early stage of expansion, the particle velocity gets to its peak in about 20% of its expansion time due to the violent expansion of the bubble at that time. Figure 4.15(b) shows the time history of the Kelvin impulse I_z for the aforementioned cases. The amplitude of bubble migrations is consistent with the time histories of the Kelvin impulse. The bubble movement and the Kelvin impulse having the same direction by the end of the collapse stage. Moreover, the Kelvin impulse gets larger in amplitude when the particle has a higher density. This again emphasises that a particle with high density attracts the bubble more than a particle with low density.

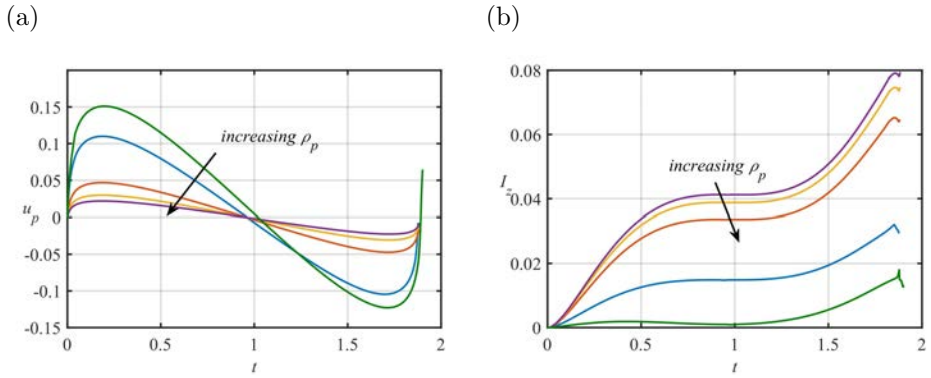

Figure 4.15: The time history of the (a) the particle velocity u_p in the $z-$direction, and (b) Kelvin impulse I_z in $z-$direction, for the cases in figure 4.12.

4.4.3 The effects of the particle radius R_p

In this section, we investigate the effects of the particle radius R_p on the bubble dynamics. The case in figure 4.16 considered with $R_p = 0.5, 2.5, 4.5$,and 6.5 respectively. The bubbles expand spherically during the expansion stage until they get to their maximum volume. Figure 4.16(a) depicts the bubble shapes at maximum volume. The expansion time T_e increases with increasing R_p and the volume decreases with increasing R_p. The top part of the bubbles near the particle have flattened more by the particle surface with a higher radius. Figure 4.16(b) represents the jet formation moment. For a particle having a radius

$R_p < R_m$, the bubble collapses faster and two jets form directed to the bubble centre.

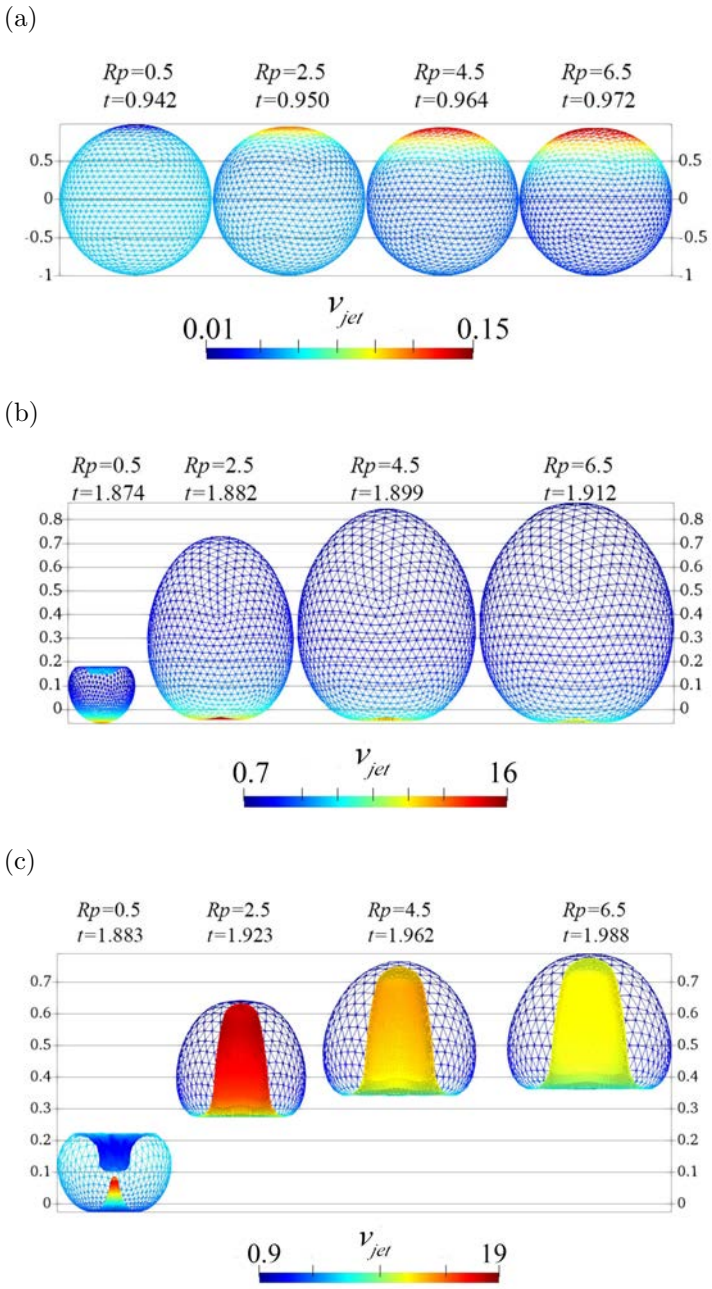

Figure 4.16: Bubble shapes at (a) maximum volume, (b) jet formation, and (c) just before the jet impact, for various values of particle radius $R_p = 0.5, 2.5, 4.5, 6.5$, $\gamma = 1.2$, and $\rho_p = 3$. The remaining parameters are are $R_m = 50\mu$m, $\delta = 0.002$, $\varepsilon = 200$, $W_e = 68$, $R_e = 496$, $\kappa = 1.4$.

The upper jet close to the particle is a weaker jet and the upward one has a higher velocity and it is thinner. The bubbles, for $R_p > R_m$, taking egg shapes with flattened

bottom far from the particles. In all of the cases mentioned, an upward jet forms directed towards the particle surface. The upward jet velocity decreases in magnitude with increasing R_p in this stage. Subsequently, the jets penetrate the apposite side of the bubble as shown in figure 4.16(c). By the end of the collapse stage, bubbles move in larger amplitudes towards the particles having a larger radius and this amplitude decreases with increasing R_p. The bubble volume at the jet impact increases with R_p while the jet velocity decreases.

Figures 4.17(a) and 4.17(b) present the pressure contours and velocity vectors for a bubble with $R_m = 50\mu m$ placed under a particle at a stand-off distance $\gamma = 1.2$, and with particle radii $R_p = 1$ and $R_p = 2.5$, respectively. The remaining parameters are the same as in figure 4.16. During the early stages of the expansion, the pressure contours depict that the pressure is almost symmetrically distributed around the bubble, except in the neighbourhood of the particle. The pressure decreases radially from the bubble and appears relatively high between the bubble and the particle (frames a1 and b1). When the bubble reaches its maximum volume, the upper surface of the bubble gets flattened by the particle. Up to this stage, the particle moves away as the pressure under the particle is higher than the pressure above the particle. Moreover, the pressure increases with increasing R_p.

During the collapse stage, the particle starts moving downward as the pressure above the particle is higher than the pressure under and above the bubble. Therefore, the collapsing bubble will pull the particle downward and as the bubble is retarded by the particle, the bubble collapses faster in the x-direction than the z-direction. Consequently, the bubble becomes elongated and a high-pressure zone starts to form on the far side of the bubble from the particle (frame 3-4). Finally, that high-pressure zone forms a thin jet towards the particle and penetrates the opposite side of the bubble (frame 4a-c). Moreover, the bubble moves away in the early stage of the expansion and then starts moving towards the particle in the expansion stage as shown in figure 4.4. The liquid in

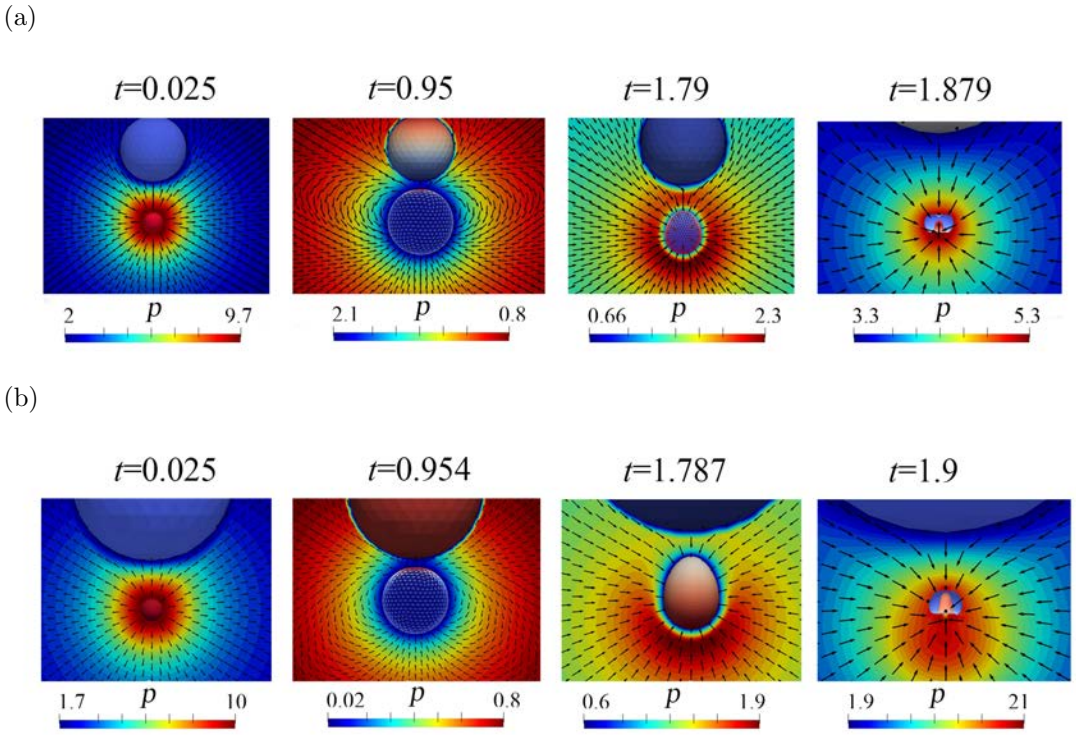

Figure 4.17: Pressure contours and velocity fields in the flow domain and normal velocity on the bubble surface for a bubble beneath a particle with radius (a) $R_p = 1$ and (b) $R_p = 2.5$. The rest of parameters are $\gamma = 1.2$, and $\rho_p = 3$, $R_m = 50\mu$m, $\delta = 0.002$, $\varepsilon = 200$, $W_e = 68$, $R_e = 496$, $\kappa = 1.4$.

the far-field flows outwards and the liquid near the part of the surface opposite to the near wall and further away from the far wall recedes, where the bubble first collapses, resulting in a stagnation point between the bubble and the far-field. In the late stages of collapse (frames a3 and b3), a high-pressure zone develops above the bubble and away from the far wall, which subsequently generates the jet towards the near wall, but inclined to the far wall (frames a4 and b4). During the period of jet development, the high-pressure zone moves towards the far wall. As the bubble is initiated nearer to the corner, the pressure field displays stronger asymmetry in the vertical plane to the near wall passing through the bubble centroid, and the high-pressure zone is more inclined away from the vertical plane.

Figure 4.18 shows the displacement of the particle centroid C_p, and the bubble centroid C_B. The particle with a smaller radius compared with the maximum bubble radius R_m

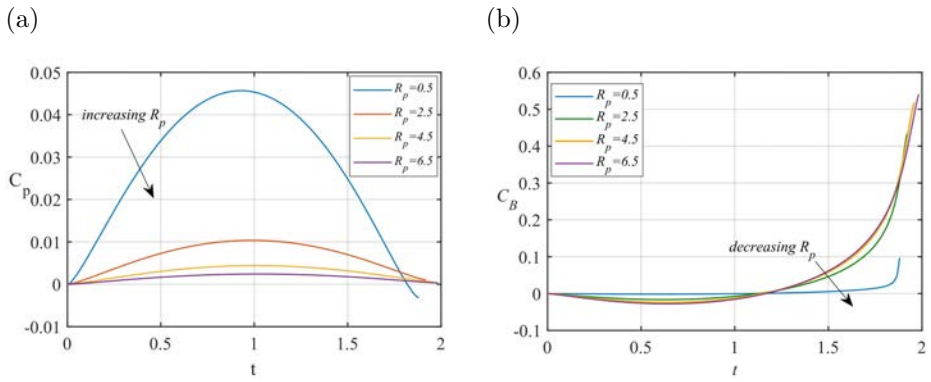

Figure 4.18: The time history of the (a) particle centroid movement C_p, and the bubble centroid movement C_B in $z-$direction, for various values of particle radius $R_p = 0.5, 2.5, 4.5, 6.5$, $\gamma = 1.2$, and $\rho_p = 3$. The remaining parameters are the same as figure 4.16.

displaces more compared with those having larger radius. The displacement decreases with increasing R_p as shown in figure 4.18(a). However, the bubble centroid C_B displaces more towards the particle with increasing R_p. Also, the bubble life time increases with increasing R_p as shown in figure 4.18(b). These trends are consistent to the time histories of the Kelvin impulse shown and the particle velocity in figures 4.19(a) and 4.19(b), respectively. Figure 4.19(a) shows the time histories of the z-component of Kelvin impulse. The Kelvin impulse I_z increases with increasing R_p. However, the particle velocity u_p in the $z-$direction decreases with increasing R_p. During the expansion stage, the particle has positive velocity (moving away from the bubble) which increases in a short time (at the time when the bubble velocity picks its maximum in the expansion stage). The particle velocity becomes negative (moving towards the bubble) during the collapse stage and by the end of the collapse it starts to increase in magnitude as shown in figure 4.19(b).

Figure 4.20(a) and 4.20(b) show the time histories of the jet velocity v_{jet} and equivalent bubble radius R_{eq} for the cases discussed in figure 4.16. As the bubble is initiated nearer the particle with a smaller radius R_p, the oscillation period and the jet velocity increase. From R_p= 6.5 to 0.5, the oscillation period increases by 5% and the dimensionless maximum jet velocity increases from 11 to 15. Also, the bubble equivalent radius R_{eq} at

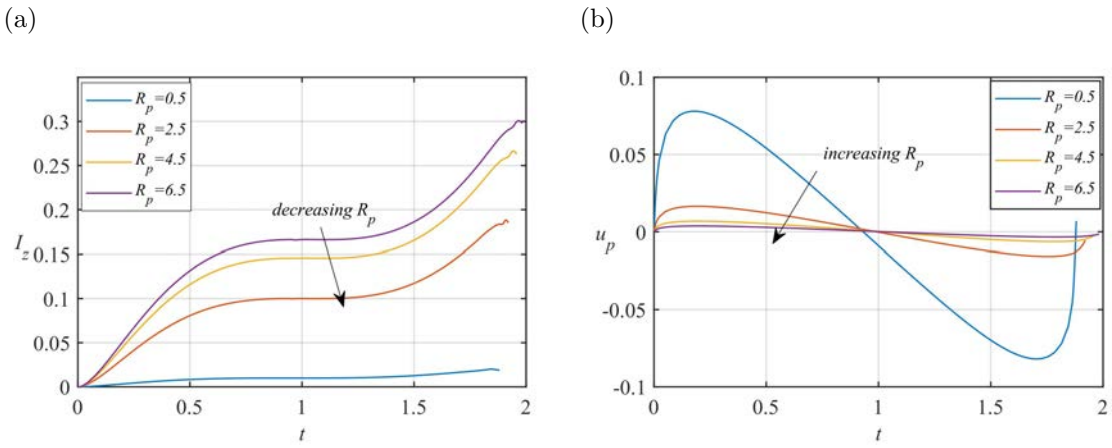

Figure 4.19: The time history of the (a) Kelvin impulse I_z, and the particle velocity u_p, for various values of particle radius $R_p = 0.5, 2.5, 4.5, 6.5$, $\gamma = 1.2$, and $\rho_p = 3$. The remaining parameters are the same as figure 4.16.

the impact time decreases from 0.22 to 0.16.

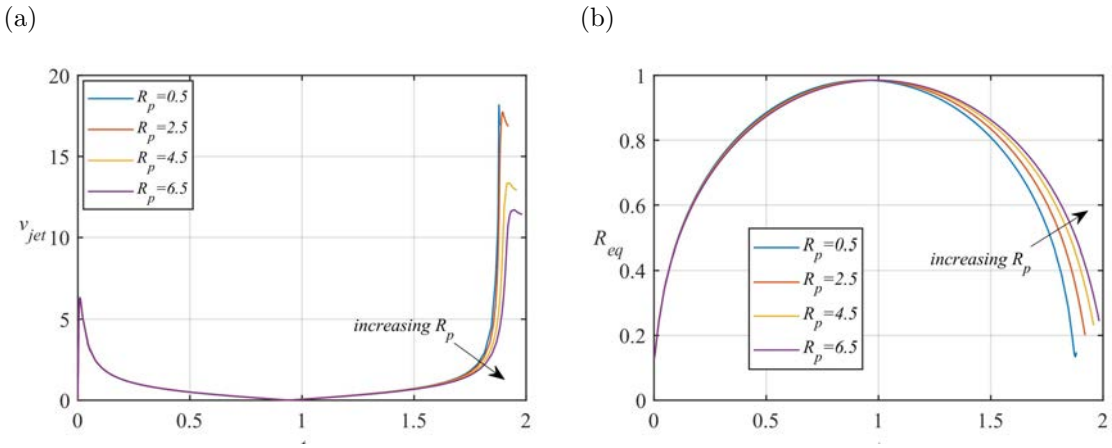

Figure 4.20: The time history of the (a) jet velocity v_{jet}, and (b) the bubble equivalent radius R_{eq}, for various values of particle radius $R_p = 0.5, 2.5, 4.5, 6.5$, $\gamma = 1.2$, and $\rho_p = 3$. The remaining parameters are the same as figure 4.16.

Figure 4.21 shows a comparison between the bubble dynamics near two spherical particles having the same mass at $m_p = 32.5$g obtained from setting different values of the particle density ρ_p and particle radius R_p using the relation $m_p = 4\pi/3\rho_p R_p^3$. The first particle had a mass of $m_p = 32.5$g, $R_p = 2$, and $\rho_p = 1$ while the second one has a $m_p = 32.5$g, $R_p = 1$, and $\rho_p = 8$. Figure 4.21(a) depicts the particle displacements having

the same mass but differing in size and density. The results showed that the effect of the particle density is dominant over the particle size. However, there is an insignificant effect on the bubble motion as shown in figure 4.21(a). Figure 4.21(b) emphasises the same effect on the particle velocity in the z-direction. The particle's velocity increases rapidly in the early stage of the expansion and then decreases gradually until the bubble reaches its maximum volume. In that stage, the particle velocity becomes zero and then during the collapse stage it continues decreasing and having a negative value. The particle's velocity change can be described as symmetrical but with an opposite sign during the expansion and collapse stage, respectively.

(a) (b)

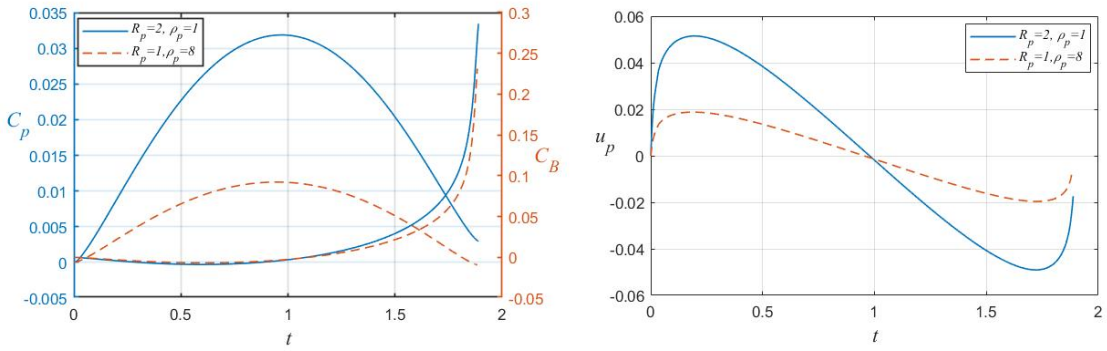

Figure 4.21: A comparison between the time history of (a) particle centroid movement C_p (blue solid-lines), and the bubble centroid movement C_B (red dash-lines) in $z-$direction, and (b) particle velocity u_p in $z-$direction, for two particles having the same mass $m_p = 32.5g$ but having different size and density. The remaining parameters are the same as figure 4.8.

Chapter 5

Numerical analysis of microbubble dynamics inside a circular rigid tube with viscous effect

5.1 Physical and mathematical modelling

Consider the dynamics of a gas bubble in a circular cylinder. The bubble at inception is placed with eccentricity E from the axis of the symmetry. The tube has radius R_T, length L_T and the two caps S_c as shown in figure 5.1. The Cartesian coordinate system Oxyz is set, with the Oxy plane being on the central line of the tube, the Ozx plane being the symmetry plane of the configuration and the origin is placed in the centroid of the tube. The length scale is chosen as the maximum bubble radius R_m and the time is scaled with

$$T = R_m \sqrt{\frac{\rho}{\Delta p}}, \tag{5.1.1}$$

where $\Delta p = p_\infty - p_v$, p_∞, p_v and ρ are the ambient pressure, saturated vapour pressure and liquid density, respectively. These values are taken as $p_\infty = 101$ kPa, $p_v = 2.3$ kPa and $\rho = 1000\text{kg m}^{-3}$. Dimensionless variables are used in the remaining text unless stated otherwise.

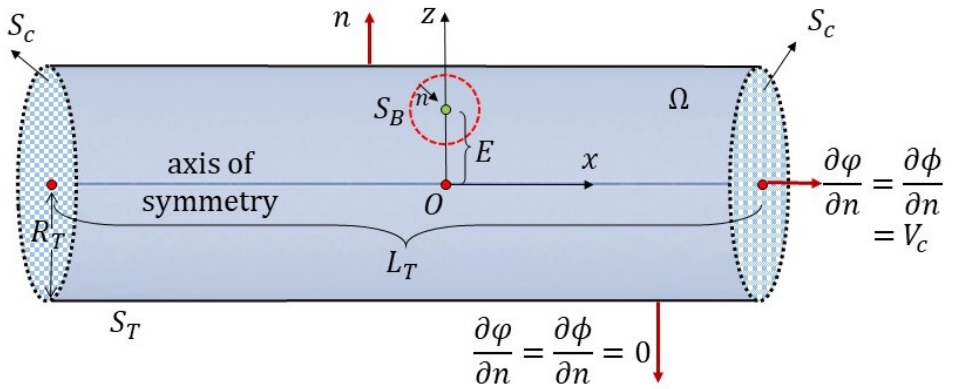

Figure 5.1: Configuration and coordinate system for bubble dynamics in a circular cylinder having a radius R_T, length L_T and the eccentricity of the bubble centre at inception from the axis of symmetry E. The boundary conditions for the tube surface and on the two ends are illustrated, where V_c is the normal velocity on the caps, $\phi = \varphi - \varphi_c$, and the subscript c refers to the caps.

There are three significant parameters in this analysis: the dimensionless tube radius $\mathfrak{R} = R_T/R_m$, the dimensionless tube length $\ell = L_T/R_m$, and the dimensionless eccentricity $\xi = E/R_m$. The flow is assumed to be incompressible, inviscid and irrotational. The fluid velocity $\boldsymbol{v}$ thus has a potential φ, $\boldsymbol{v} = \nabla\varphi$, satisfying Laplace's equation $\Delta\varphi = 0$.

Little research has been undertaken for bubble dynamics in a circular cylinder which considers the limitation on the boundary. Chen et al. (2016) investigated the dynamics of a coated microbubble oscillating in an elastic micro-vessel. They claimed that the tube length should be long enough to simulate a vessel of infinite length, so that the effects of the two end caps can be ignored on the microbubble following Hosseinkhah and Hynynen (2012) and Hosseinkhah et al. (2013). They considered the length of the tube to be 100 times the initial bubble radius. Wang et al. (2018) considered bubble dynamics in a vessel with the same limitation.

In this work, we are following (Ishida et al., 2001) for the bubble dynamics between two parallel rigid walls which, due to experiments, have features similar to the bubble dynamics in a circular tube. A new boundary condition is developed on the tube end

caps to consider the effect of the caps on the dynamics of the bubble. Here we modify their boundary condition for bubble dynamic in a circular cylinder using 3D-BIM.

The dimensionless continuity equation and the equation of motion can be described as follows

$$\nabla^2\varphi = 0, \tag{5.1.2a}$$

$$\frac{\partial\varphi}{\partial t} + \frac{1}{2}\left|\nabla\varphi\right|^2 + P = f(t) = \frac{\partial\varphi_c}{\partial t} + \frac{V_c^2}{2}, \tag{5.1.2b}$$

in which

$$P = \frac{(p - p_\infty)}{\Delta p}, \quad \text{and} \quad V_c = \nabla\varphi_c\Big|_c = \frac{\partial\varphi}{\partial n}\Big|_c,$$

where the subscript c denotes the values on the caps. Here, we define $\phi = \varphi - \varphi_c$, then the equations (5.1.2) can be expressed as follows

$$\nabla^2\phi = 0, \tag{5.1.3a}$$

$$\frac{\partial\phi}{\partial t} + \frac{1}{2}\left|\nabla\phi\right|^2 + P = \frac{V_c^2}{2}, \tag{5.1.3b}$$

where $\phi\big|_c = 0$ vanishes on the caps. The kinematic boundary conditions on the surface of the cylinder S_T, on the bubble surface S_B, and on the caps S_c are as follows

$$\frac{\partial\varphi}{\partial n} = \frac{\partial\phi}{\partial n} = 0 \quad \text{on } S_T, \tag{5.1.4a}$$

$$\frac{D\boldsymbol{r}}{Dt} = \nabla\phi \text{ on } S_B, \tag{5.1.4b}$$

$$V_c(t) = \frac{\partial\phi}{\partial n} = -\frac{1}{2A_c}\iint_{S_B}\frac{\partial\phi(\boldsymbol{q},t)}{\partial n}dS(\boldsymbol{q}) \quad \text{on } S_c, \tag{5.1.4c}$$

where $\boldsymbol{r}$ is the position vector of the boundary, $\boldsymbol{n}$ is normal on the boundary surface, and D/Dt denotes the material derivative, r is the radial distance, $A_c = \pi\mathfrak{R}^2$ is the surface area of the caps. The condition (5.1.4a) is the impermeable boundary condition on the rigid boundaries and (5.1.4b) requires a material point on the bubble surface remains

there.

The dynamic boundary condition on the bubble surface, S_B requires that the pressure difference across the surface is equal to the Laplace pressure. Using the modified Bernoulli equation, after implementing the viscous correction p_{vc}, which was described in chapter 2, and the boundary conditions (5.1.4), the dimensionless Bernoulli equation can be expressed as

$$\frac{D\phi}{Dt} = 1 + \frac{1}{2}\big|\nabla\phi\big|^2 - \varepsilon\Big(\frac{V_0}{V}\Big)^{\kappa} + 2\frac{r_c}{W_e} - 2\frac{(1+C)}{R_e}\frac{\partial^2\phi}{\partial n^2} + \frac{1}{2}V_c^2(t), \tag{5.1.5}$$

where $W_e = R_m\Delta p/\sigma$ is the Weber number, $R_e = \sqrt{\rho\Delta p}R_m/\mu$ is Reynolds number, $\varepsilon = p_{g0}/\Delta p$ is dimensionless initial pressure inside the bubble and r_c is the radius of mean curvature of the bubble surface. Considering the boundary conditions (5.1.4), the boundary integral expression of (5.1.3) becomes

$$\begin{aligned} c(\boldsymbol{r},t)\phi(\boldsymbol{r},t) = &\iint_{S_B}\Big[\frac{\partial\phi(\boldsymbol{q},t)}{\partial n}G(\boldsymbol{r},\boldsymbol{q}) - \phi(\boldsymbol{q},t)\frac{\partial G(\boldsymbol{r},\boldsymbol{q})}{\partial n}\Big]dS(\boldsymbol{q}) \\ &- \iint_{S_T}\Big[\phi(\boldsymbol{q},t)\frac{\partial G(\boldsymbol{r},\boldsymbol{q})}{\partial n}\Big]dS(\boldsymbol{q}) + V_c\iint_{S_c}G(\boldsymbol{r},\boldsymbol{q})dS(\boldsymbol{q}), \end{aligned} \tag{5.1.6}$$

where S includes all the boundaries: the bubble surface S_B, the tube surface S_T and the cap surfaces S_c as shown in figure 5.1. The Green function $G(\boldsymbol{r},\boldsymbol{q})$, due to a unit source in an infinite fluid domain is given by

$$G(\boldsymbol{r},\boldsymbol{q}) = \frac{1}{|\boldsymbol{r}-\boldsymbol{q}|}. \tag{5.1.7}$$

Non-uniform time steps have been chosen sensibly in each iteration for the procedure to avoid any instability as below

$$\Delta t = \frac{\Delta\varphi}{\max\limits_i\Big(D\phi_i/Dt\Big)}, \tag{5.1.8}$$

where $\Delta\varphi$ is a constant and it is chosen as 0.001 in this work, ϕ_i is the potential of the i^{th} vertex on the bubble surface.

5.2 Validation of the numerical model

5.2.1 Comparison with experiments

To evaluate the BIM model, we compare the computational results with experimental images by (Wang et al., 2019). The bubble surface and the tube surface are discretized with 2000 and 12894 elements, respectively. The mesh density on the tube surface is increased gradually from the centre to improve the accuracy of the results. Initially, the bubble is placed at the centre of the tube having a length of $\ell = 20$.

The first case is for a laser beam generated bubble having a maximum radius $R_m = 14.6$ mm, placed inside a cylindrical tube with radius $\mathfrak{R} = 1.19$, close to the centre line with a small eccentricity given by $\xi = 0.1$. As shown in figure 5.2, during the early stages of the expansion, (frames a, b), the bubble becomes increasingly elongated along the centre line. From the expansion stage until the start of the collapse stage, the bubble is relatively symmetrical (frames a-c), but afterwards becoming asymmetric along the centre line (frames d, e), due to the greater effect from the upper face of the tube. The upper face of the bubble is then flattened to the tube surface (frame c). Two counter-propagating jets are formed along the centre line of the tube (frames d-e), meeting at the end of the collapse stage (frames d, e). The phenomenon of two propagating jets was already observed during the collapse of strongly elongated bubbles in free liquid (Tsiglifis and Pelekasis, 2007).

For the second case, the bubble is located far from the centre line. The bubble having a maximum radius $R_m = 11.6$ mm placed inside a cylindrical tube with radius $\mathfrak{R} = 1.72$, with eccentricity $\xi = 0.74$. As shown in figure 5.3, as with the previous case, the bubble becomes increasingly elongated along the centre line and the upper face close to the upper side of the tube is flattened during the early stages of the expansion (frames a,b). The

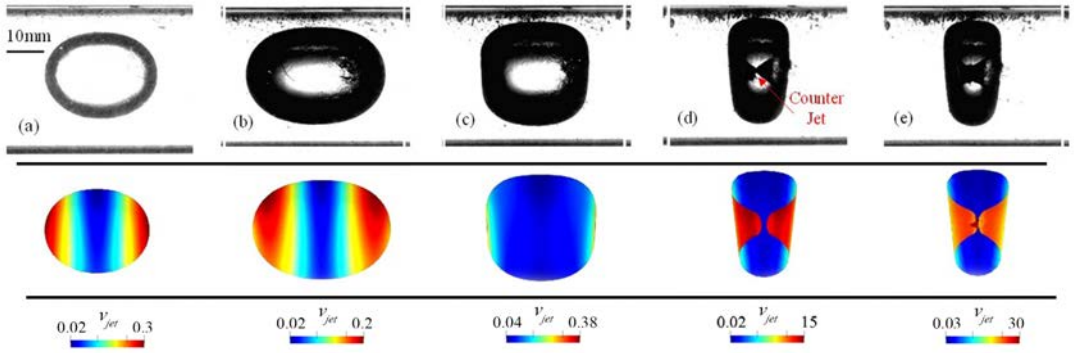

Figure 5.2: Bubble dynamics in a circular tube with eccentricity $\xi = 0.1$, for $R_m = 14.6$ mm, $\mathfrak{R} = 1.19$, and $\ell = 20$, at dimensionless time $t = 1.14, 2.87, 3.357, 4.68,$ and 4.7, corresponding to frames (a-e), respectively. The remaining parameters are given by $\delta = 0.038$, $\kappa = 1.4$, and W_e=19794

bubble in this case however, is no longer symmetrical along the centre line of the tube (frames a-e), but similar to the previous case, becomes symmetric along the z-axis. Two counter propagating jets are formed again facing upwards and they meet at the end of the collapse (frames d, e). Figure 5.4 shows the time histories of the equivalent bubble

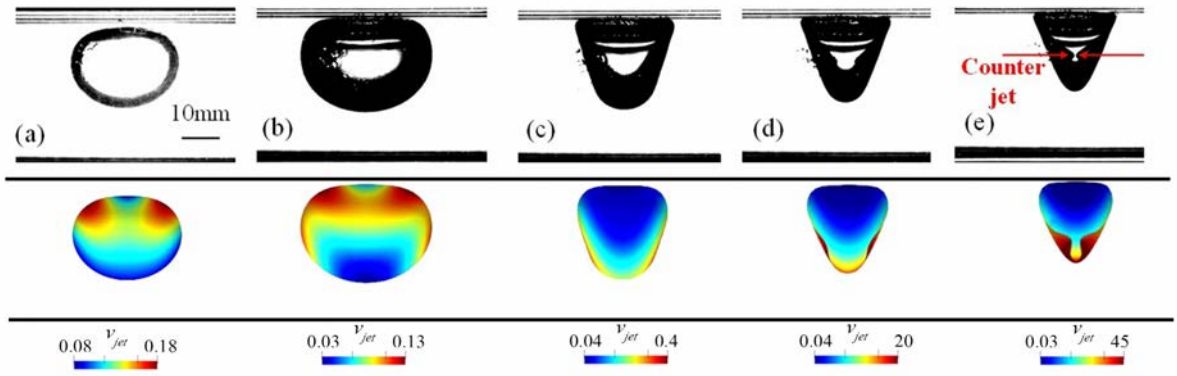

Figure 5.3: Bubble dynamics in a circular tube with eccentricity $\xi = 0.74$, for $R_m = 11.6$ mm, $\mathfrak{R} = 1.72$, and $\ell = 20$, at dimensionless time $t = 0.98, 2.53, 3.75, 4.2,$ and 4.49, corresponding to frames (a-e), respectively. The remaining parameters are given by $\delta = 0.034$, $\kappa = 1.4$, and W_e=15726

radius R_{eq} for the cases in figures 5.2 and 5.3. For the second experiment, as the bubble is closer to the tube surface, the bubble takes a longer time to reach its maximum volume. However, the maximum equivalent radius in the first experiment is less than in the second

experiment as the bubble surface is retarded by the surface of tube equally in all directions except along the tube centre line.

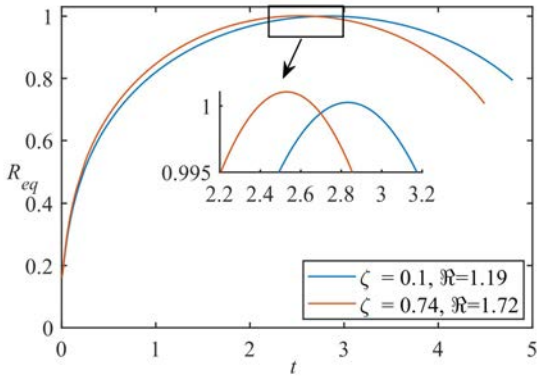

Figure 5.4: Time histories of the equivalent bubble radius R_{eq}, for the cases shown in figures 5.2 and 5.3

5.3 Numerical results

5.3.1 Effect of the tube length ℓ and convergent test

To analyse the effect of the tube length and the convergence of the BIM, a convergence test is performed for the case $R_m = 14.6$ mm, $\mathfrak{R} = 1.5$, $\xi = 0$. Various tube lengths were chosen: $\ell = 10, 20, ..., 70$ having surface elements $M = 9624, 9792, 14314, 18738, 18966, 19367,$ and 21698, respectively. The remaining parameters are $\delta = 0.038$, $\kappa = 1.4$, and $W_e = 19794$. Figure 5.5 illustrates the effect of the tube length, ℓ, on the simulation. There were no significant differences when the length ℓ was greater than 40. Shorter length results in a reduction in the bubble lifetime as well as the bubble migration as shown in figures 5.6(a) and 5.6(b), respectively.

The simulation converges with ℓ and the difference for $\ell \geq 40$ is about 0.3% which is considered to be insignificant. The circle-dash line in figure 5.6 represent the simulation using $\ell = 30$ including the boundary condition (5.1.4c) on the caps. There is a significant change in the convergence in terms of the bubble lifetime and the movement by 4.8% compared with the one without the boundary condition (5.1.4c). The remaining calculations

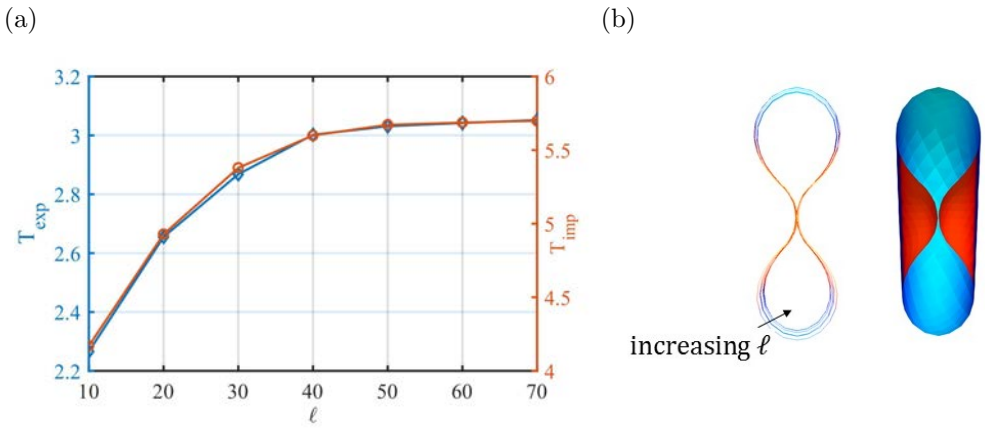

Figure 5.5: A comparison of the results in figure 5.6 (a) between bubble expansion lifetime T_{exp}, and the bubble impact lifetime T_{imp}, and (b) bubble shapes just before the jet impact, for the different values of tube lengths $\ell = 10, 20, \ldots, 70$.

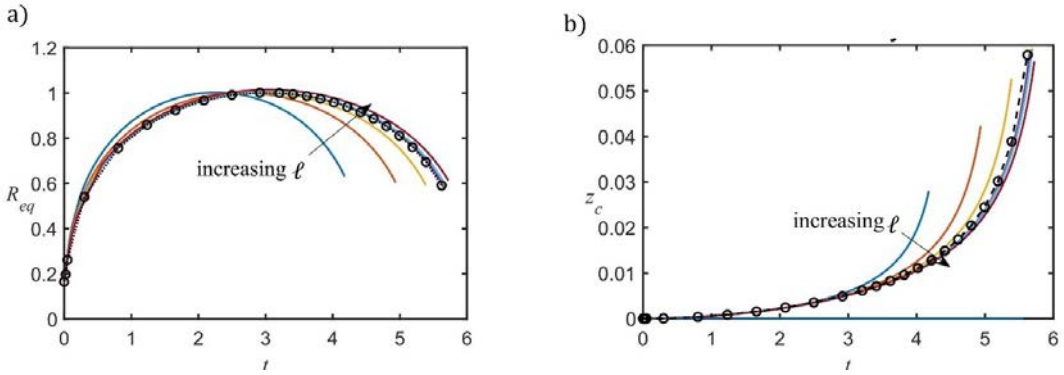

Figure 5.6: A convergent test applied by choosing different tube lengths $\ell = 10, 20, \ldots, 60$ without the boundary condition (5.1.4c) (solid lines), and using the boundary condition (5.1.4c) (circle-dash line when $\ell = 30$). The comparison is for the time histories of the (a) equivalent bubble radius R_{eq}, and (b) bubble centroid motion in the z-direction. The parameters are given by $\mathfrak{R} = 1.5$, $R_m = 14.6$ mm, $\delta = 0.038$, $\kappa = 1.4$, and $W_e = 19794$.

in this study were performed for $\ell = 30$, considering the boundary condition (5.1.4c) and the elements on the tube surface is set to 18758 elements.

5.3.2 Bubbles initiated at the symmetric axis ($\xi = 0$) for different tube radius

In this section, we analyse the effect of the tube radius $\mathfrak{R}$ on the dynamics of the bubble in a tube. Here, we perform the calculations for various tube radius $\mathfrak{R} = 1, 2$ and 3. The remaining parameters are $R_m = 14.6$mm, $\ell = 30$, $\delta = 0.038$, $\varepsilon = 100$, $W_e = 19794$, $R_e = 1.4e5$, $\kappa = 1.4$. Figure 5.7 shows the corresponding bubble shapes at the expansion stage, maximum volume, jet formation and at the jet impact. The bubble expands spherically for the cases when $\mathfrak{R} \geq 2$, but for $\mathfrak{R} < 2$ the bubble is elongated along the axis of the symmetry (frame 1). When the bubble attains its maximum volume, it is flattened by the tube surfaces for the cases when $\mathfrak{R} \geq 2$ as shown in figure 5.7 (frame 2). During the expansion stage, two jets form along the axis of the symmetry for $\mathfrak{R} \leq 2$ as shown in (frame 3) and for a larger radius, there is only one upward jet, due to the small effect of the gravity and the effects of the Bjerknes force, which is directed towards the tube surface (frame 4).

Figure 5.8 shows the time histories of the equivalent bubble radius and the jet velocity v_{jet} just before the impact versus $\mathfrak{R}$. The oscillation period decreases conversely with $\mathfrak{R}$ as shown in figure 5.8(a). From $\mathfrak{R}$= 1 to 3, the oscillation period decreases by 35%. Also, the jet velocity v_{jet} increases linearly with $\mathfrak{R}$ as shown in figure 5.8(b).

Figure 5.9(a) displays the time history of the displacement of the bubble centroid in z-direction $z_c(t)$ for the above cases. The bubble is almost motionless during the expansion stage and moves towards the upper face of the tube opposite the gravitational forces at a much higher amplitude during the collapse. The migration amplitude decreases with increasing $\mathfrak{R}$. These trends are consistent to the time histories of the Kelvin impulse shown in figure 5.9(b). The z-component of the Kelvin impulse decreases with $\mathfrak{R}$ and it is increasing with time.

This phenomenon is different when a smaller bubble of micron size is considered. The

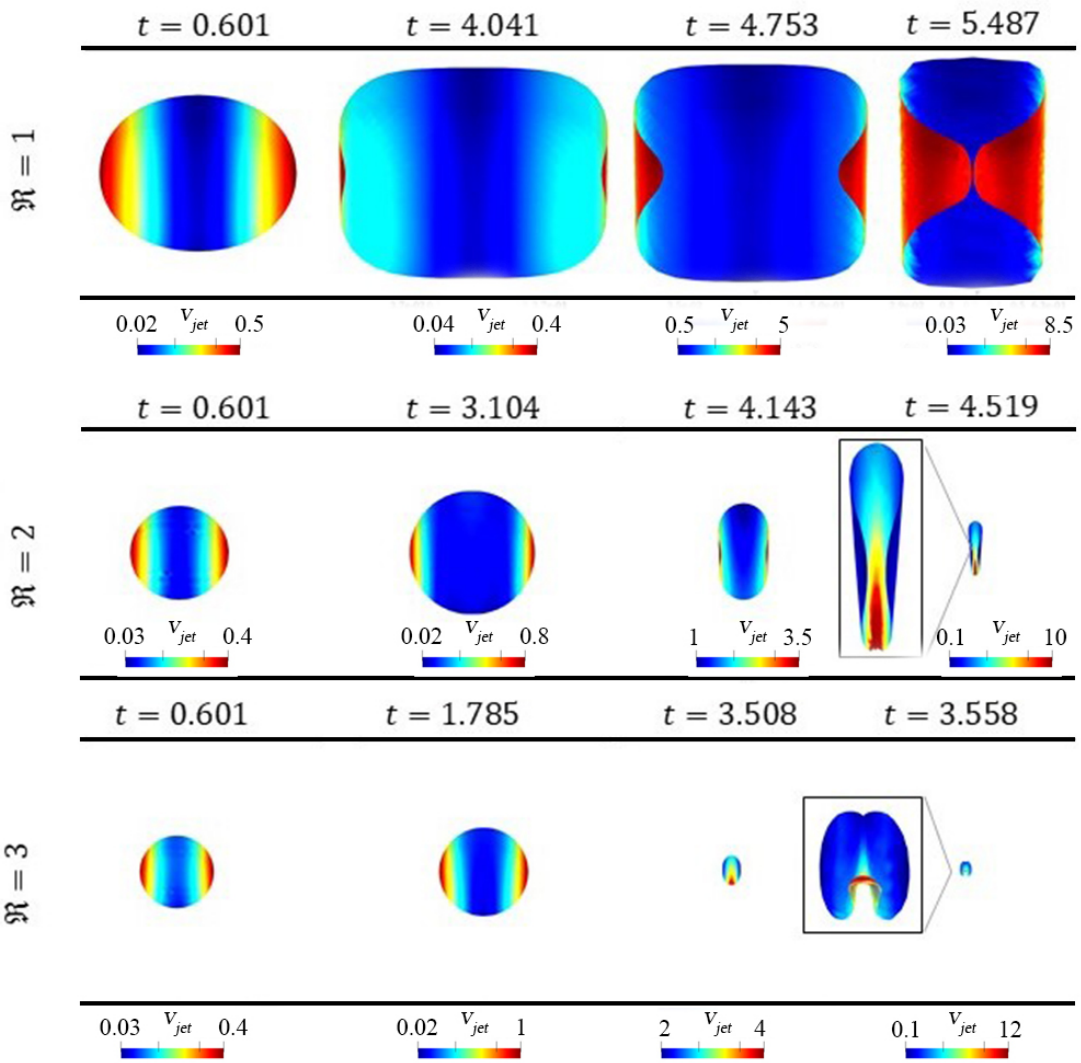

Figure 5.7: Bubble shapes at expansion, maximum volume, jet formation, and just before the jet impact, for $\mathfrak{R} = 1, 2$, and 3, eccentricity $\xi = 0$. The remaining parameters are $R_m = 14.6$mm, $\ell = 30$, $\delta = 0.038$, $\varepsilon = 100$, $W_e = 19794$, $R_e = 1.4e5$, $\kappa = 1.4$.

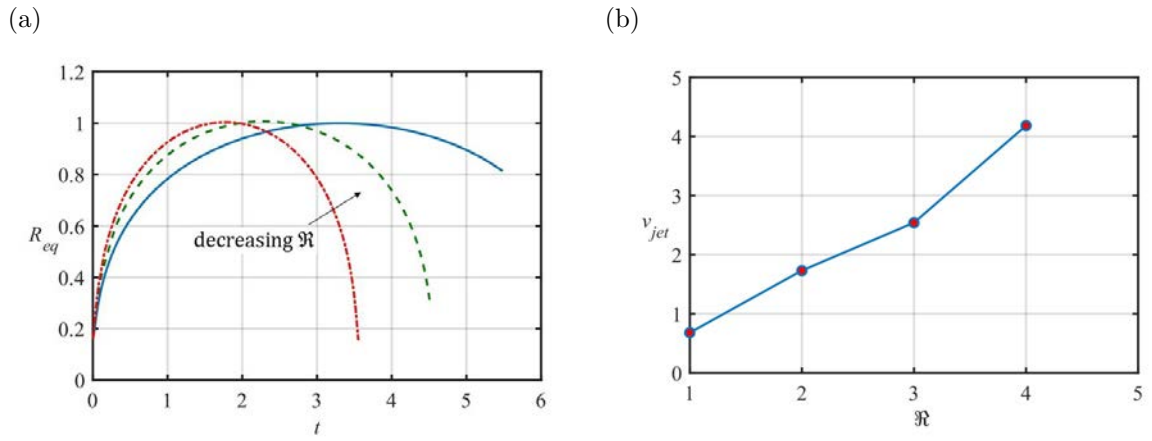

Figure 5.8: BIM results of (a) time history of the equivalent bubble radius R_{eq}, and (b) jet velocity just before impact versus $\mathfrak{R} = 1, \cdots, 4$, for the cases in figures 5.7.

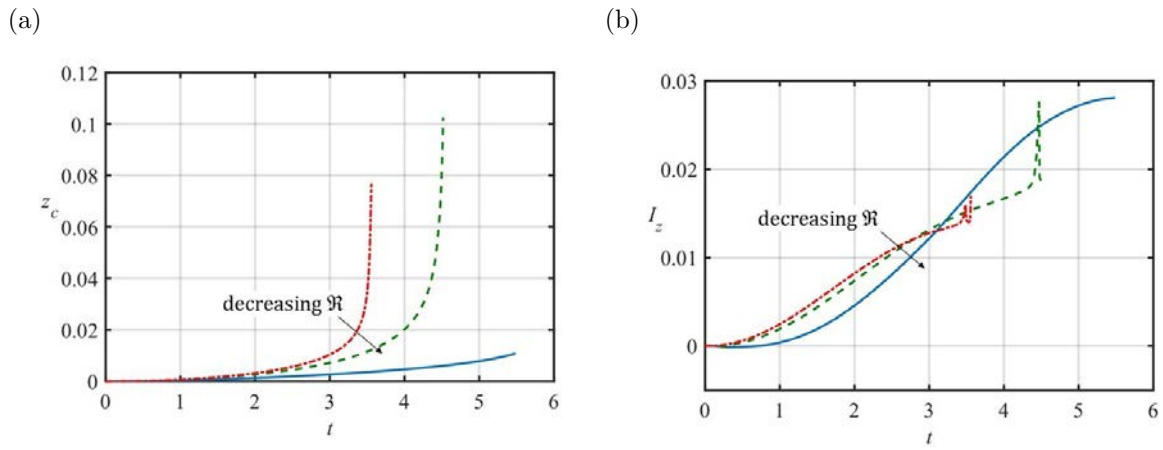

Figure 5.9: Time history of the (a) displacement of the bubble centroid, and (b) Kelvin impulse, for the cases in figures 5.7.

bubble is less flattened when the $\mathfrak{R} < 1.5$ and by the end of the collapse stage the bubble becomes more elongated (figure 5.10, frame 4). For $\mathfrak{R} \geq 2$ the bubble obtains a disc shape during the collapse stage as shown in figure 5.10.

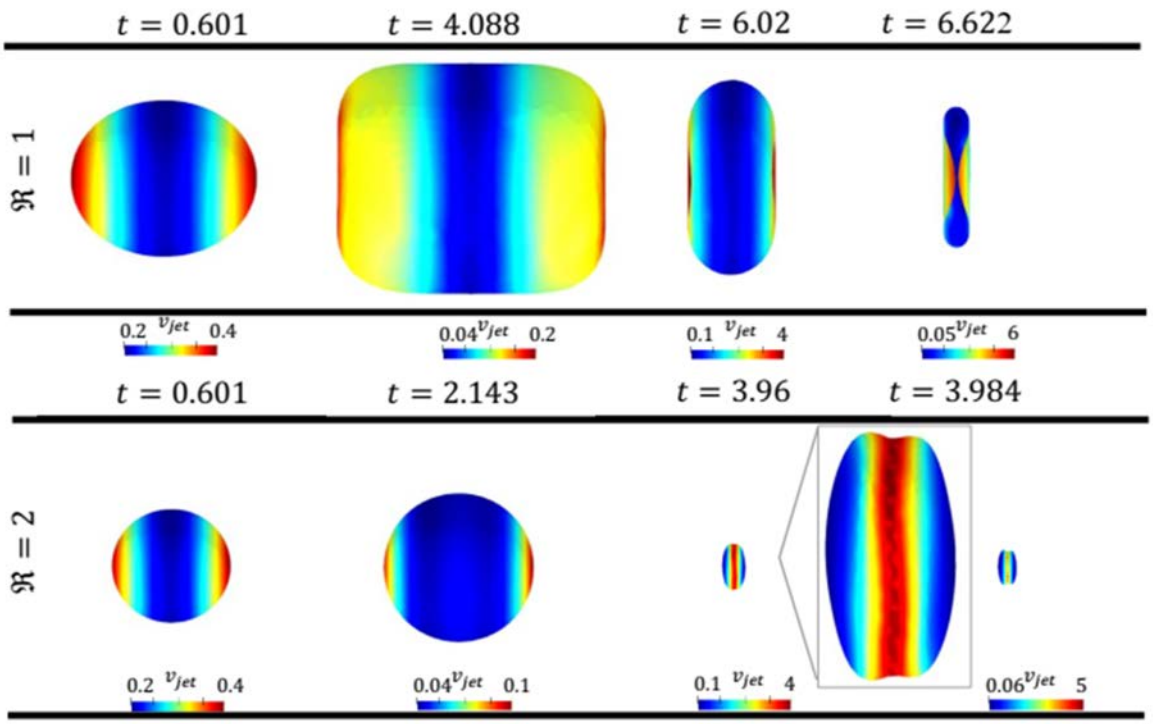

Figure 5.10: Bubble shapes at expansion,maximum volume, jet formation, and just before the jet impact, for $\mathfrak{R} = 1, 2$, eccentricity $\xi = 0$. The remaining parameters are $R_m = 50$ μm, $\ell = 30$, $\delta = 0.038$, $\varepsilon = 200$, $W_e = 67.7$, $R_e = 496$, $\kappa = 1.4$.

5.3.3 Bubbles initiated not at the symmetric axis ($\xi \neq 0$) for different tube radius

In this section, we analyse the effect of the eccentricity ξ on the dynamics of the bubble in a tube. Here, the tube radius is fixed at $\mathfrak{R} = 4$, and the simulations are carried out for various eccentricities $\xi = 0.5, 1$, and 2.5. Figure 5.11 shows the corresponding bubble shapes at inception, maximum volume, jet formation and at the jet impact. The bubble expands spherically for all of the cases, except for the near bubble surface which is flattened by the tube surface when the bubble is close to it as shown in figure 5.11(b). Due to a small effect of the gravity, jets form during the early stage of the collapse pointing upwards to the tube surface. At this stage, the bubble has a greater volume when it is closer to the surface, i.e by increasing ξ as shown in figure 5.11(c). Figure 5.11(d) shows

the bubble shapes at the end of the collapse stage. As ξ increases, the bubble moves more towards the tube surface and jet shapes vary for different ξ. This phenomenon differs when a smaller tube radius is considered or when a bubble of a micron size is considered. For a tube radius of $\mathfrak{R} < 2$, there are usually two inclined jets towards the tube surface and meet at the bottom part of the bubble far from the tube surfaces as shown in figure 5.3.

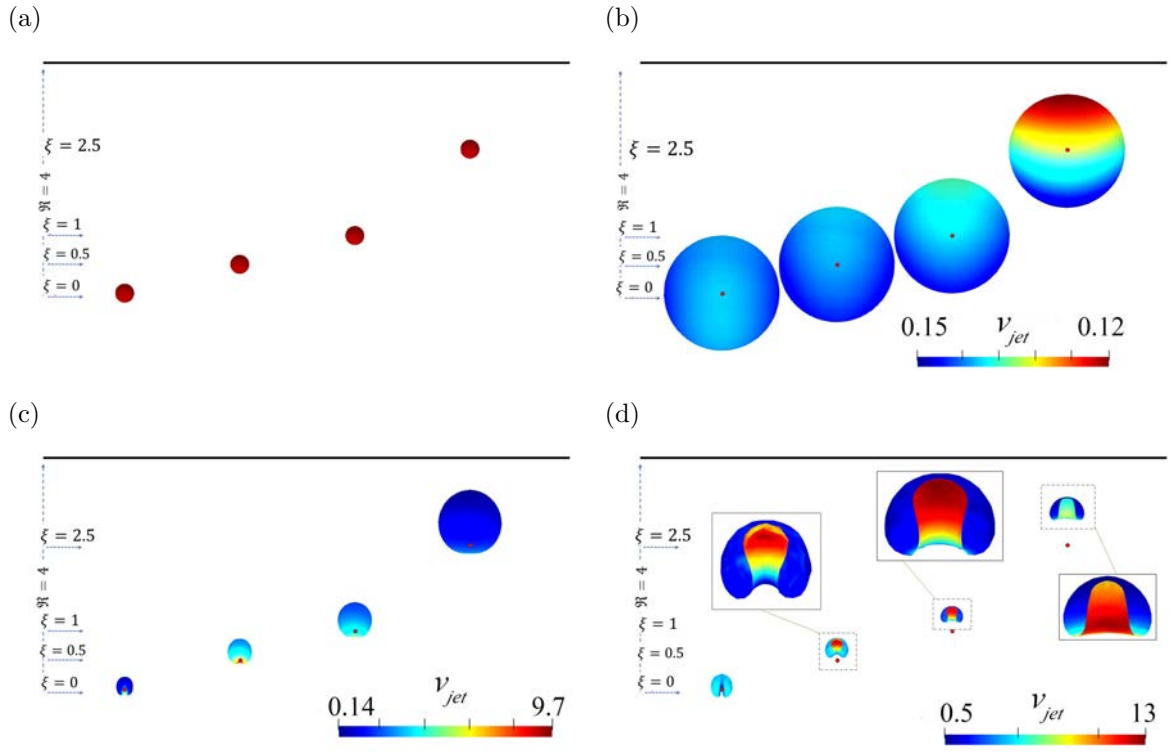

Figure 5.11: Bubble shapes at (a) inception, (b) maximum volume, (c) jet formation (b) starting the collapse stage, (c) jet formation, and (d) just before the jet impact, for $\mathfrak{R} = 4$ and eccentricity $\xi = 0, 0.5, 1$, and 2.5. The remaining parameters are the same as figure 5.7.

Figure 5.12 shows the time histories of the equivalent bubble radius and the jet velocities versus ξ for the cases in figure 5.11. The oscillation period increases with increasing ξ. From $\xi = 0.5$ to 2.5, the period increases by 3%. However, the jet velocity increases with ξ for $\xi \leq 1.5$ and then decreases for $\xi > 1.5$ as shown in figure 5.12(b). Figure 5.13(a) displays the time history of the displacement of the bubble centroid in z-direction $z_c(t)$

for the above cases. The bubble is almost motionless during the expansion stage except for the cases with a higher eccentricity in which the bubble moves away during expansion and moves back towards the upper face of the tube at a much higher amplitude during the collapse. The migration amplitude increases with increasing ξ. The time histories of the Kelvin impulse are shown in figure 5.13(b). The z-component of the Kelvin impulse increases with ξ when the bubble is closer to the tube surfaces.

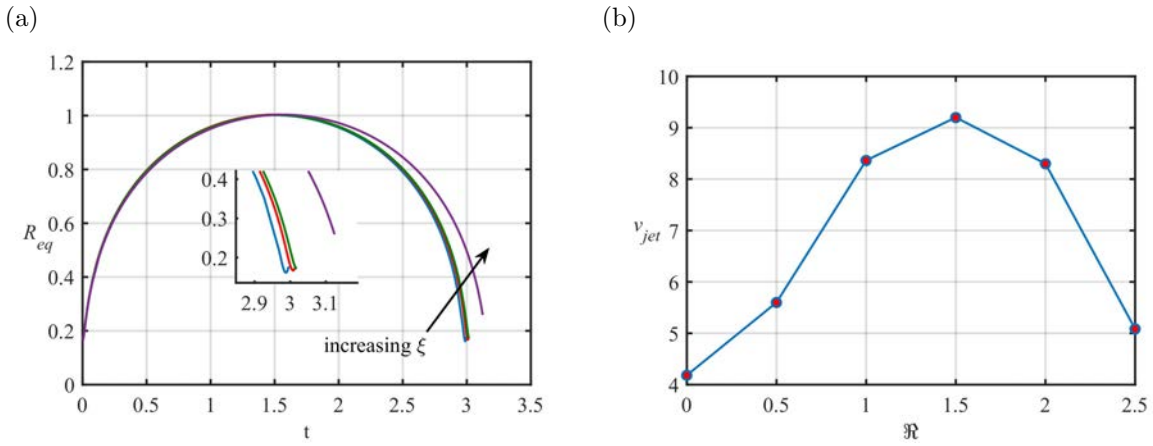

Figure 5.12: BIM results of (a) time history of the equivalent bubble radius R_{eq}, and (b) jet velocity just before impact versus $\xi = 0, \cdot, 2.5$, for the cases in figures 5.11.

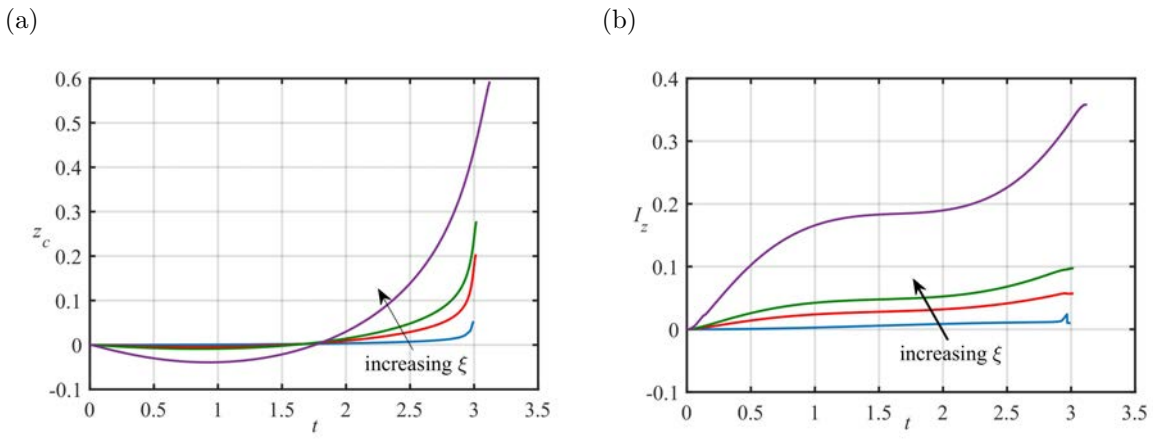

Figure 5.13: Time history of the (a) displacement of the bubble centroid, and (b) Kelvin impulse, for the cases in figures 5.11.

Chapter 6

Conclusions and possible future development

6.1 Conclusions

In this thesis, we studied and described the physical, mathematical and numerical model for bubble dynamics near a rigid surface. A few techniques are implemented to simulate the associated bubble dynamics models. An interpolation scheme is implemented for the bubble surface for the potential distribution. The moving least square method is used to calculate the curvature and the tangential velocity on the surface. We implemented a modified elastic mesh technique together with the volume preserve smoothing technique, which provide a stable and excellent mesh during the computation while maintaining the accuracy of the numerical model. A new post-processor has been implemented for displaying the bubble motion, velocity field and pressure contour, using the Visualization Toolkit (VTK)/Paraview. Computations and comparisons with experiment images are carried out to demonstrate the robustness of the model.

The above numerical techniques are implemented for simulating bubble dynamics at a corner, a spherical suspended particle with viscous effects and bubble dynamics in a circular tube.

(I) **Numerical investigation of bubble dynamics at a corner**

The growth and collapse of a bubble in a corner subject to the secondary Bjerknes forces due to the walls. The bubble expands approximately spherically, except for the bubble surfaces near walls which are compressed by the walls. Physically the sides of the bubble nearer the walls will move into a region of higher relative impedance than other sides. During the latter stages of the collapse, the bubble initiated at the bisector of the corner becomes oblate along the bisector, as the secondary Bjerknes forces are stronger for the parts of the bubble surfaces near the walls. A high-speed liquid jet then forms pointing towards the corner, due to the combined effects of the two secondary Bjerknes forces. For a bubble initiated away from the bisector, the jet is approximately pointing to the near wall but inclined to the corner, when the Bjerknes force due to the near wall is dominant.

The pressure field loses spherical symmetry during the early stages of the expansion long before the bubble becomes non-spherical. A velocity stagnation point forms at the start of the collapse and a high pressure zone forms during the latter stages of the collapse at the base of the jet, which subsequently drives the jet. As the bubble is initiated near the corner, the pressure field displays strong asymmetry to the vertical plane to the near wall passing through the bubble centroid. The asymmetry is stronger for a smaller corner angle.

For a smaller standoff distance to the corner or for a smaller corner angle, the oscillation period, the bubble volumes at the start of the jet formation and jet impact, and the width of the jet increase, whereas the jet velocity decreases.

The bubble migrates away from the near wall and corner during its expansion and moves back to the near wall and corner during its collapse, but at much larger speed and amplitude. The amplitude of migration towards the corner decreases with the standoff distance to the corner but increases with corner angle. The amplitude of migration per-

pendicular to the near wall increases with both of them, as the second Bjerknes force due to the far wall decreases. These trends are consistent with the time histories of the Kelvin impulse. The Kelvin impulse theory is shown to accurately predict the jet direction.

The bubble migration and jetting towards the near wall and the corner show that there are no blind spots in the cavitation cleaning of a corner in terms of the jetting, the acoustic micro-streaming and the associated shear stress. However, the combined effect of the decrease in jet velocity and the increase of jet width for smaller corner angles is worthy of further investigation for the cleaning of the vertex in these corners.

(II) **The interaction between a micro-bubble and a suspended rigid spherical particle**

Under the potential flow assumptions, fully nonlinear interaction between a microbubble and a spherical particle is simulated using the boundary integral method. The auxiliary function method under various boundary conditions is used to deal with the mutual dependence between the acceleration of the sphere and the hydrodynamic force. Additionally, the pressure and velocity fields in three-dimensional cases are calculated by the direct boundary integral method to gain insight into the basic mechanisms of bubble dynamic behaviours. The predicted bubble shapes and particle motion have excellent agreement with the experiments. A parametric study is carried out in terms of the particle density ρ_P, particle radius R_p, and the dimensionless standoff distances γ of the bubble centre at inception from the surface of the particle. Some interesting results were observed as follows:

In the study of convergence, simulations were performed considering bubble and particle element sizes. The results emphasise that the particle element size does not affect the dynamics of the bubble or the particle movement. The particle element size may affect the results only when the bubble is attached to the particle. Also, the results of the three-dimensional model become identical with increasing the element size on the bubble surface.

During the expansion stage, the sphere and the bubble are separated and get attracted to each other during the collapse stage. Bubble and the particle motion vary with initial parameters. Moreover, these parameters have effects on the bubble jetting towards the sphere, collision of two axial jets, and bubble shapes.

The standoff distance γ has an impact on the bubble shapes, bubble motion, particle motion and the jet velocity. With decreasing γ, the bubble becomes more elongated along the $z-$ direction and has an egg shape. two counter jets form along the $z-$direction. The jet velocity of the downward jet (a weak jet from the surface of the bubble close to the sphere) decreases in magnitude and size with increasing γ. Also, the velocity of the upwards jet (the jet directed to the sphere from the far side of the bubble) increases. The particle motion is more affected by γ compared with the bubble motion. Their motion decreases with increasing γ.

The particle density ρ_p has a great impact on the bubble-particle coupling process. During the collapse stage until the jet formation and with increasing ρ_p, the bubble is more elongated and has a larger volume. The bubble moves away more with increasing ρ_p during the bubble lifetime. At the early stage of the expansion, the bubble departs further from the particle when we increase the particle density ρ_p. The particle motion during the expansion stage decreases with ρ_p and its velocity u_p decreases with increasing ρ_p and γ. Compared with a fixed sphere, the bubble jet gains higher velocity in the suspended sphere case, but the Kelvin impulse associated with bubble motion is much lower.

The particle size R_p, also, has effects on bubble shapes, jet velocities, bubble motion and on the particle movement. The downward jet (the weak jet close to the particle surface) vanishes earlier with increasing R_p, especially when the particle has a larger radius compared with the maximum bubble radius. The jet velocity of the bubble decreases with increasing R_p and bubble lifetime increases with increasing R_p. Also, the bubble centroid motion and the Kelvin impulse increase with increasing the particle size.

(III) **Numerical analysis of a microbubble dynamics inside a circular rigid tube**

with viscous effect

In chapter 5, the dynamics of a bubble inside a rigid circular tube is studied numerically using the boundary integral method. The results are analysed in terms of three geometrical parameters: the dimensionless tube radius $\mathfrak{R}$, the dimensionless tube length ℓ, and the dimensionless eccentricity ξ is the distance of the bubble centre at inception from the centre line of the tube. Some new phenomena are observed and may be summarized as follows:

If a bubble is initiated on the centre line of the tube, the bubble expands and collapses primarily along this axis especially when we consider microbubbles, otherwise the bubble migrates upwards due to gravitational forces. During the collapse stage, two counter propagating jets are formed along the tube axis, when the radius of the tube is $\mathfrak{R} \leq 2$. Parallel to the axis of symmetry, the two counter jets impact each other at the end of the collapse stage. When $\mathfrak{R} > 2$, bubbles collapse to a thin disc shape. As the tube becomes thinner, the jets form earlier and have a larger velocity. This phenomenon varies with the maximum bubble size. When the bubble is of micron size and $\mathfrak{R} > 2$, there are no jets in the first cycle and the bubble rebounds. In such cases, the jet usually forms perpendicular to the axis of the symmetry.

For larger tube radius $\mathfrak{R} > 1$, and when eccentricity is large (i.e. near the tube wall), the bubble expands asymmetrically. The bubble surface closest to the tube wall becomes flattened to the tube surface. During the collapse stage, the asymmetry is strengthened as the distal part of the bubble shrinking more rapidly and collapsing towards the tube wall. In the case of a larger bubble, two inclined propagating jets are formed far from the tube wall which meet at the end of the collapse and are directed upwards towards the tube wall. This phenomenon is slightly distinctive from the case of a bubble collapsing near a flat wall. In the case of bubble dynamics near a flat wall, a single jet often forms and impacts the wall at the end of the collapse. For a smaller bubble of micron size, the results show that for $\mathfrak{R} > 2$ a single jet forms during the collapse stage which impacts the

tube surface at the end of the collapse.

For $\mathfrak{R} \leq 1$, the bubble expands non-spherically and forms an elongated bubble during the expansion stage. At the collapse stage of the bubble, compression happens primarily along the tube axis, which results in creating two counter-propagating liquid jets. The bubble lifetime increases with ℓ, ξ and decreases with $\mathfrak{R}$. For the considered cases, the jet velocity increases with $\mathfrak{R}$ when $\xi = 0$ and for asymmetric cases when $\xi \neq 0$, the jet velocity increases with ξ for $\xi \leq 1.5$ and then decreases for $\xi > 1.5$.

6.2 Possible future research

In this thesis, we have modelled and analysed bubble dynamics near solid boundaries. The results have provided excellent insight into several applications of bubble cavitation, though extensions can always be made. One of the possible developments is to model the impact of the bubble jet with the opposite bubble surface and subsequent toroidal bubbles. This can be done using the vortex ring model (Wang et al., 1996; Liu, Wang and Zhang, 2016). A vortex ring is put inside the bubble ring after jet impact, whose circulation is equal to the potential jump at the impact point. The present work can also be developed to the interaction of a bubble and an elastic boundary (Liu et al., 2016).

This study is concerned with microbubble dynamics in an incompressible liquid. Yet, compressibility effects may not be negligible in some situations, especially at the end of violent collapse, which is linked with the emission of shockwaves (Lauterborn and Kurz, 2010; Wang and Blake, 2010, 2011). Weakly compressible flow theory has been developed by (Wang, 2013, 2014) for bubble dynamics. Here in the inner region of the flow domain in terms of the Mach number, the flow near the bubble is approximately incompressible to second order. For the outer region, far away from the flow, analytical methods are used. As such, we can develop a BIM model, including compressible effects for the current three-dimensional incompressible model using the weakly compressible flow theory.

In addition, cavitation processes occur frequently in non-Newtonian fluids (Lind and

Phillips, 2010*b*,*a*). In industry and medicine, non-Newtonian contributions are known to have a significant effect on many aspects. As such, it is important to develop the present model for bubble dynamics in non-Newtonian fluids. The results obtained from the discussed model in this thesis will significantly advance the understanding of bubble dynamics in diverse biological and industrial processes.

Appendices

Appendix A
Image locations and the Greens function in a corner for angle $\alpha = \pi/k$

To elucidate the procedure of locating the images, let wall$_1$ is the plane $z = 0$ and wall$_2$ is the plane $x\sin(\alpha) = z\cos(\alpha)$. Consider the intersection line of these two walls which corresponds to the y-axis and let the source point $\boldsymbol{q}_0 : (x_0, y_0, z_0)$ make an angle θ_0 with wall-1 as shown in figure A.1. Let $qj : (x_j, y_j, z_j),\ j = 1, , 2k-1$ denote the successive images of $\boldsymbol{q}_0$ in both walls. The images lie on a circle with centre at $(0, y_0, 0)$ and radius r_q. Due to the successive reflections in both walls, a sequence of angles θ_j form which subsequently define the location of the images $\boldsymbol{q}_j$. The anglesθ_j may be expressed as follows

$$\theta_{4j} = 2j\alpha + \theta_0, j = 0, 1, , \lfloor (k-1)/2 \rfloor, \quad \text{reflections in wall}_2, \tag{1a}$$
$$\theta_{4j-2} = 2j\alpha - \theta_0, j = 0, 1, , \lfloor (k)/2 \rfloor, \quad \text{reflections in wall}_2, \tag{1b}$$
$$\theta_{2j+1} = -\theta_{2j}, j = 0, 1, , k-1, \quad \text{reflections in wall}_1, \tag{1c}$$

where $\lfloor a \rfloor$ is the greatest integer less than or equal to a. The components of the images are defined to be

$$x_j = r_q\cos(\theta_j), \quad y_j = v_0, \quad \textit{and } z_j = r_q\sin(\theta_j), \tag{2}$$

in which $\theta_j,\ j = 0, ..., 2k-1$ are measured anticlockwise from wall$_1$.

For any point $\boldsymbol{r} = (x, y, z)$in the domain, we have the following Greens function

$$G(\boldsymbol{r}, \boldsymbol{q}) = \sum_{j=0}^{2k-1} \frac{1}{|\boldsymbol{r} - \boldsymbol{q}_j|} = \sum_{j=0}^{2k-1} \frac{1}{R_j}, \text{ and } \nabla G(\boldsymbol{r}, \boldsymbol{q}_0) = -\sum_{j=0}^{2k-1} \frac{\boldsymbol{r} - \boldsymbol{q}_j}{R_j^3} \tag{3}$$

where

$$R_j = |\boldsymbol{r} - \boldsymbol{q}_j| = \sqrt{(x - x_j)^2 + (y - y_j)^2 + (z - z_j)^2}. \tag{4}$$

In the numerical procedure, $\boldsymbol{q}_j$ is parametrized using equation (2.3.4(a)). The unit normal on wall$_1$ is $\boldsymbol{n}_1 =< 0, 0, 1 >$, and on wall$_2$ is $\boldsymbol{n}_2 =< -\sin(\alpha), 0, \cos(\alpha) >$ and let $r_q = |\boldsymbol{q}_0|$.

The Greens function in (3) satisfies the boundary condition $\nabla G \cdot \boldsymbol{n}_1 = 0$, on wall$_1$

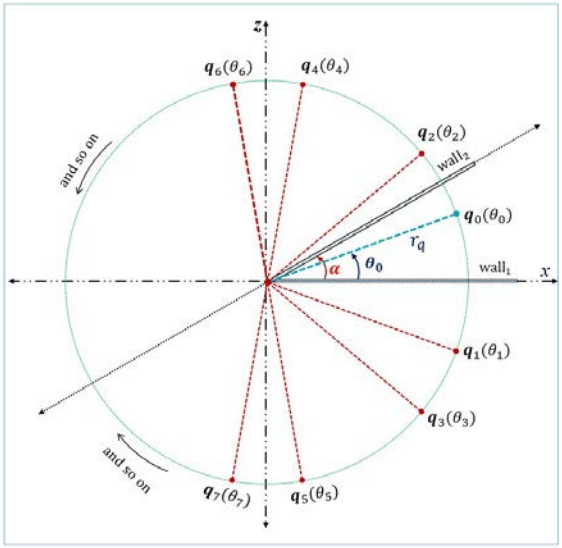

Figure A.1: The images for a source point $\boldsymbol{q}_0$ which makes angle θ_0 with wall$_1$ for $\alpha = \pi/k$.

where $z = 0$ as follows

$$\begin{aligned}\nabla G \cdot \boldsymbol{n}_1 &= -\sum_{j=0}^{2k-1} \frac{z - z_j}{R_j^3} = -\sum_{j=0}^{2k-1} \frac{z - r_q \sin(\theta_j)}{R_j^3} \\ &= \sum_{j=0}^{k-1} \frac{z - r_q \sin(\theta_{2j+1})}{R_{2j+1}^3} + \frac{z - r_q \sin(\theta_{2j})}{R_{2j}^3}\end{aligned} \tag{5}$$

On wall$_1$, the angles are symmetric, as shown in chapter 3 in equation (3.2.5), that is, $\theta_{j+1} = -\theta_{2j}$ and hence $\sin(\theta_{2j+1}) = -\sin(\theta_{2j})$. The denominator of equation (5) can be simplified to yield

$$\begin{aligned}R_{2j+1} &= \sqrt{\Big(x - r_q \cos(\theta_{2j+1})\Big)^2 + \Big(y - y_0\Big)^2 + \Big(-r_q \sin(\theta_{2j+1})\Big)^2} \\ &= \sqrt{\Big(x - r_q \cos(\theta_{2j})\Big)^2 + \Big(y - y_0\Big)^2 + \Big(r_q \sin(\theta_{2j})\Big)^2} = R_{2j}.\end{aligned} \tag{6}$$

Therefore, the terms in (5) cancel in pairs and we have the required result that $\nabla G \cdot \boldsymbol{n}_1 = 0$ on wall$_1$.

Using the same procedure on wall$_2$, $x \sin(\alpha) = zcos(\alpha)$, to show that $\nabla G \cdot \boldsymbol{n}_2 = 0$ on

wall$_2$, we have

$$\begin{aligned}\nabla G \cdot \boldsymbol{n}_2 &= -\sum_{j=0}^{2k-1} \frac{(x-x_j)\sin(\alpha) - (z-z_j)\cos(\alpha)}{R_j^3} = -\sum_{j=0}^{2k-1} \frac{z - r_q \sin(\theta_j)}{R_j^3} \\ &= -\sum_{j=0}^{2k-1} \frac{(x - r_q\cos(\theta_j))\sin(\alpha) - (z - r_q\sin(\theta_j))\cos(\alpha)}{R_j^3} \\ &= -\sum_{(i,j)} \left[\frac{(x\sin(\alpha) - z\cos(\alpha) + r_q \sin(\theta_i - \alpha))}{R_i^3} \right. \\ &\quad \left. + \frac{(x\sin(\alpha) - z\cos(\alpha) + r_q \sin(\theta_j - \alpha))}{R_j^3} \right],\end{aligned} \tag{7}$$

in which i and j represent the two groups of the images described in chapter 3, equation (3.2.5), where $\sin(\theta_j - \alpha) = -\sin(\theta_i - \alpha)$ for i, j are in group one and two respectively. Consequently, the terms corresponding to the ordered pairs in (7) cancel if $R_i = R_j$. On wall$_2$, we have

$$\begin{aligned}\cos(\theta_j) &= \cos(\theta_j - \alpha + \alpha) \\ &= \cos(\theta_j - \alpha)\cos(\alpha) - \sin(\theta_j - \alpha)\sin(\alpha) \\ &= \cos(\theta_i - \alpha)\cos(\alpha) + \sin(\theta_i - \alpha)\sin(\alpha)\end{aligned} \tag{8}$$

And

$$\begin{aligned}\sin(\theta_j) &= \sin(\theta_j - \alpha + \alpha) \\ &= \sin(\theta_j - \alpha)\cos(\alpha) + \cos(\theta_j - \alpha)\sin(\alpha) \\ &= -\sin(\theta_i - \alpha)\cos(\alpha) + \cos(\theta_i - \alpha)\sin(\alpha)\end{aligned} \tag{9}$$

using euations (8) and (9), we have

$$\begin{aligned}R_i^2 &= [x - r_q\cos(\theta_i)]^2 + [y - v_0]^2 + [z - r_q\sin(\theta_i)]^2 \\ &= [x - r_q\cos(\theta_j - \alpha)\cos(\alpha) - r_q\sin(\theta_j - \alpha)\sin(\alpha)]^2 + [y - v_0]^2 \\ &+ [z - r_q\cos(\theta_j - \alpha)\cos(\alpha) + r_q\sin(\theta_j - \alpha)\sin(\alpha)]^2 \\ &= [x - r_q\cos(\theta_j)]^2 + [y - v_0]^2 + [z - r_q\sin(\theta_j)\sin(\alpha)]^2 \\ &- 4r_q\sin(\theta_j - \alpha)\sin(\alpha)[x - r_q\cos(\theta_j - \alpha)\cos(\alpha)] \\ &+ 4r_q\sin(\theta_j - \alpha)\cos(\alpha)[z - r_q\cos(\theta_j - \alpha)\sin(\alpha)] \\ &= R_j^2 + 4r_q\sin(\theta_j - \alpha)[z\cos(\alpha) - x\sin(\alpha)] \\ &= R_j^2.\end{aligned} \tag{10}$$

Thus, the Greens function satisfies the boundary condition,$\nabla G \cdot \boldsymbol{n}_2 = 0$ on wall$_2$. Hence, the Greens function satisfies the boundary condition, $\nabla G \cdot \boldsymbol{n} = 0$ both walls.

Appendix B
Maple code to calculate the analytical Kelvin impulse and F_θ in a corner

B.1 For angle $\alpha = \pi/2$

restart; with(LinearAlgebra); with(VectorCalculus);
$\alpha := \pi/2$;
$\gamma_N := 1$; $\gamma_F := 1$;

eq1 := $\alpha - \alpha_1 - \alpha_2$;
eq2 := $\gamma_N - dc\ \sin(\alpha_1)$;
eq3 := $\gamma_F - dc\ \sin(\alpha_2$;

_EnvExplicit := true;
Sol := solve(eq_1, eq_2, eq_3, dc, α_1, α_2);
vals := eval([dc, α_1, α_2], Sol[2]);
rq := vals[1]; α_1:= vals[2]; α_2 := vals[3]

$x_0 := r_q \cos(\alpha_1)$; $y_0 := 0$; $z_0 := \gamma_N$;
$\theta_0 := \arctan(z_0/x_0)$;
θ_1:= -θ_0;
$\theta_2 := 2\alpha - \theta_0$;
θ_3 := -θ_2;

$r_q := \gamma_N \sin(\alpha_1)$;
$x_1 := rq\ \cos(\theta_1)$;
$z_1 := rq\ \sin(\theta_1)$;
$x_2 := rq\ \cos(\theta_2)$;
$z_2 := rq\ \sin(\theta_2)$;
$x_3 := rq\ \cos(\theta_3)$;
$z_3 := rq\ \sin(\theta_3)$;

$r_P :=< xx, yy, zz >;$
$rq_0 :=< x_0, y_0, z_0 >;$
$rq_1 :=< x_1, y_0, z_1 >;$
$rq_2 :=< x_2, y_0, z_2 >;$
$rq_3 :=< x_3, y_0, z_3 >;$

$GG_0 := r_P - rq_0;$
$GG_1 := r_P - rq_1;$
$GG_2 := r_P - rq_2;$
$GG_3 := r_P - rq_3;$

$G_0 := Norm(r_P - rq_0, 2);$
$G_1 := Norm(r_P - rq_1, 2);$
$G_2 := Norm(r_P - rq_2, 2);$
$G_3 := Norm(r_P - rq_3, 2);$
$G_{rq} := GG_1/G_1^3 + GG_2/G_2^3 + GG_3/G_3^3;$

$\boldsymbol{F} := evalf(simplify(subs(xx = x_0, yy = y_0, zz = z_0, G_{rq})));$
$F_\theta := arctan(F_3/F_1);$
$\boldsymbol{I}_{Tc} := -(4\sqrt{6}\pi)/9\ evalf(Beta(7/6, 3/2))\boldsymbol{F};$
$I_{TcN} := Norm(\boldsymbol{I}(T_c));$

B.2 For angle $\alpha = \pi/4$

restart; with(LinearAlgebra); with(VectorCalculus);
$\alpha := \pi/4;$
$\gamma_N := 1;\ \gamma_F := 1;$

eq1 := $\alpha - \alpha_1 - \alpha_2$;
eq2 := $\gamma_N - dc\ \sin(\alpha_1);$
eq3 := $\gamma_F - dc\ \sin(\alpha_2;$

_EnvExplicit := true;
Sol := solve(eq_1, eq_2, eq_3, dc, α_1, α_2);
vals := eval([dc, α_1, α_2], Sol[2]);
rq := vals[1]; α_1:= vals[2]; α_2 := vals[3]

$x_0 := r_q \cos(\alpha_1);\ y_0 := 0;\ z_0 := \gamma_N;$
$r_q = \gamma_N / \sin(\alpha_1);$
$\theta_0 := \arctan(z_0/x_0);$
θ_1:= -θ_0;
$\theta_2 := 2\alpha - \theta_0;$
θ_3 := -θ_2;

$\theta_4 := 2\alpha + \theta_0;$
$\theta_5 := -\theta_4;$
$\theta_6 := 4\alpha - \theta_0;$
$\theta_7 := -\theta_6;$

$r_q := \gamma_N \sin(\alpha_1);$
$x_1 := rq\ \cos(\theta_1); \quad z_1 := rq\ \sin(\theta_1);$
$x_2 := rq\ \cos(\theta_2); \quad z_2 := rq\ \sin(\theta_2);$
$x_3 := rq\ \cos(\theta_3); \quad z_3 := rq\ \sin(\theta_3);$
$x_4 := rq\ \cos(\theta_4); \quad z_4 := rq\ \sin(\theta_4);$
$x_5 := rq\ \cos(\theta_5); \quad z_5 := rq\ \sin(\theta_5);$
$x_6 := rq\ \cos(\theta_6); \quad z_6 := rq\ \sin(\theta_6);$
$x_7 := rq\ \cos(\theta_7); \quad z_7 := rq\ \sin(\theta_7);$

$r_P :=< xx, yy, zz >;$
$rq_0 :=< x_0, y_0, z_0 >; \quad rq_1 :=< x_1, y_0, z_1 >;$
$rq_2 :=< x_2 y_0, z_2 >; \quad rq_3 :=< x_3, y_0, z_3 >;$
$rq_4 :=< x_4, y_0, z_4 >; \quad rq_5 :=< x_5, y_0, z_5 >;$
$rq_6 :=< x_6, y_0, z_6 >; \quad rq_7 :=< x_7, y_0, z_7 >;$

$GG_0 := r_P - rq_0; \quad GG_1 := r_P - rq_1;$
$GG_2 := r_P - rq_2; \quad GG_3 := r_P - rq_3;$
$GG_4 := r_P - rq_4; \quad GG_5 := r_P - rq_5;$
$GG_6 := r_P - rq_6; \quad GG_7 := r_P - rq_7;$

$G_0 := Norm(r_P - rq_0, 2); \quad G_1 := Norm(r_P - rq_1, 2);$
$G_2 := Norm(r_P - rq_2, 2); \quad G_3 := Norm(r_P - rq_3, 2);$
$G_4 := Norm(r_P - rq_4, 2); \quad G_5 := Norm(r_P - rq_5, 2);$
$G_6 := Norm(r_P - rq_6, 2); \quad G_7 := Norm(r_P - rq_7, 2);$

$G_{rq} := GG_1/G_1^3 + GG_2/G_2^3 + GG_3/G_3^3 + GG_4/G_4^3 + GG_5/G_5^3 + GG_6/G_3^6 + GG_7/G_3^7;$

$\boldsymbol{F} := evalf(simplify(subs(xx = x_0, yy = y_0, zz = z_0, G_{rq})));$
$F_\theta := arctan(F_3/F_1);$
$\boldsymbol{I}_{Tc} := -(4\sqrt{6}\ evalf(Beta(7/6, 3/2))\boldsymbol{F};$
$I_{TcN} := Norm(\boldsymbol{I}(T_c));$

List of References

Abramowitz, Milton and Irene A Stegun. 1965. Handbook of mathematical functions with formulas, graphs, and mathematical table. In *US Department of Commerce*. National Bureau of Standards Applied Mathematics series 55.

Arabi, Sina, Ricardo Camarero and Francois Guibault. 2014. "Unstructured meshes for large body motion using mapping operators." *Mathematics and computers in simulation* 106:26–43.

Arora, M., C. D. Ohl and K. A. Mørch. 2004. "Cavitation inception on microparticles: A self-propelled particle accelerator." *Phys. Rev. Lett.* 92(17):174501.

Bailey, Michael R, James A McAteer, Yuri A Pishchalnikov, Mark F Hamilton and Tim Colonius. 2006. "Progress in lithotripsy research." *Acoustics today* 2(2):18–29.

Benjamin, T. B. and A. T. Ellis. 1966. "The collapse of cavitation bubbles and the pressures thereby produced against solid boundaries." *Philos. Trans. A. Math. Phys. Eng. Sci.* 260(1110):221–240.

Best, J. P. 1993. "The formation of toroidal bubbles upon the collapse of transient cavities." *J. Fluid Mech.* 251:79–107.

Best, J. P. and J. R. Blake. 1994. "An estimate of the Kelvin impulse of a transient cavity." *J. Fluid Mech.* 261:75–93.

Best, JP and A Kucera. 1992. "A numerical investigation of non-spherical rebounding bubbles." *Journal of fluid mechanics* 245:137–154.

Blake, J. R. 1988. "The Kelvin impulse: application to cavitation bubble dynamics." *ANZIAM J.* 30(2):127–146.

Blake, J. R., B. B. Taib and G. Doherty. 1986. "Transient cavities near boundaries. Part 1. Rigid boundary." *J. Fluid Mech.* 170:479–497.

Blake, J. R. and D. C. Gibson. 1981. "Growth and collapse of a vapour cavity near a free surface." *J. Fluid Mech.* 111:123–140.

Blake, J. R. and D. C. Gibson. 1987. "Cavitation bubbles near boundaries." *Annu. Rev. Fluid Mech.* 19(1):99–123.

Blake, J. R., M. C. Hooton, P. B. Robinson and R. P. Tong. 1997. "Collapsing cavities, toroidal bubbles and jet impact." *Phil. trans. R. Soc. A* 355(1724):537–550.

Blake, J. R., P. B. Robinson, A. Shima and Y. Tomita. 1993. "Interaction of two cavitation bubbles with a rigid boundary." *J. Fluid Mech.* 255:707–721.

Blake, J. R. and P. Cerone. 1982. "A note on the impulse due to a vapour bubble near a boundary." *J. Austral. Math. Soc. Ser. A* 23(04):383–393.

Blake, John R, David M Leppinen and Q. X. Wang. 2015. "Cavitation and bubble dynamics: the Kelvin impulse and its applications." *Interface focus* 5(5):20150017.

Blake, JR, Y Tomita and RP Tong. 1998. The art, craft and science of modelling jet impact in a collapsing cavitation bubble. In *In Fascination of Fluid Dynamics*. Springer pp. 77–90.

Borkent, B. M., M. Arora, C. D. Ohl, J. N. De, M. Versluis, D. Lohse, K. A. Mørch, E. Klaseboer and B. C. Khoo. 2008. "The acceleration of solid particles subjected to cavitation nucleation." *J. Fluid Mech.* 610:157–182.

Bremond, N., M. Arora, C. D. Ohl and D. Lohse. 2006. "Controlled multibubble surface cavitation." *Phys. Rev. Lett.* 96(22):224501.

Brennen, C. E. 2013. *Cavitation and bubble dynamics*. Cambridge University Press.

Brennen, Christopher Earls. 2015. "Cavitation in medicine." *Interface focus* 5(5):20150022.

Brujan, E. A., G. S. Keen, A. Vogel and J. R. Blake. 2002. "The final stage of the collapse of a cavitation bubble close to a rigid boundary." *Phys. Fluids* 14(1):85–92.

Brujan, E. A., T. Ikeda and Y. Matsumoto. 2005. "Jet formation and shock wave emission during collapse of ultrasound-induced cavitation bubbles and their role in the therapeutic applications of high-intensity focused ultrasound." *Phys. Med. Biol.* 50(20):4797.

Brujan, EA, A Pearson and JR Blake. 2005. "Pulsating, buoyant bubbles close to a rigid boundary and near the null final Kelvin impulse state." *International journal of multiphase flow* 31(3):302–317.

Brujan, EA, T Ikeda and Y Matsumoto. 2004. "Dynamics of ultrasound-induced cavitation bubbles in non-Newtonian liquids and near a rigid boundary." *Physics of Fluids* 16(7):2402–2410.

Brujan, Emil A, David S Hecht, Frank Lee and Gary A Williams. 2005. "Properties of luminescence from laser-created bubbles in pressurized water." *Physical Review E* 72(6):066310.

Brujan, Emil-Alexandru, Kester Nahen, Peter Schmidt and Alfred Vogel. 2001. "Dynamics of laser-induced cavitation bubbles near elastic boundaries: influence of the elastic modulus." *Journal of Fluid Mechanics* 433:283–314.

Brujan, Emil-Alexandru, Tatsuya Noda, Atsushi Ishigami, Toshiyuki Ogasawara and Hiroyuki Takahira. 2018. "Dynamics of laser-induced cavitation bubbles near two perpendicular rigid walls." *J. Fluid Mech.* 841:28–49.

Caboussat, Alexandre. 2006. "A numerical method for the simulation of free surface flows with surface tension." *Computers & fluids* 35(10):1205–1216.

Calvisi, Michael L, Olgert Lindau, John R Blake and Andrew J Szeri. 2007. "Shape stability and violent collapse of microbubbles in acoustic traveling waves." *Physics of Fluids* 19(4):047101.

Calvisi, ML, JI Iloreta and AJ Szeri. 2008. "Dynamics of bubbles near a rigid surface subjected to a lithotripter shock wave. Part 2. Reflected shock intensifies non-spherical cavitation collapse." *Journal of Fluid Mechanics* 616:63–97.

Chahine, G. L. and A. Bovis. 1980. Oscillation and collapse of a cavitation bubble in the vicinity of a two-liquid interface. In *Cavitation and inhomogeneities in underwater acoustics*. Springer pp. 23–29.

Chahine, G. L. and T. O. Perdue. 1988. Simulation of the three-dimensional behavior of an unsteady large bubble near a structure. In *Proc. Third Inter. Colloquium on Bubbles and Drops, Monterey, California*.

Chahine, Georges L. 1982. Experimental and asymptotic study of nonspherical bubble collapse. In *Mechanics and Physics of Bubbles in Liquids*. Springer pp. 187–197.

Chahine, Georges L, Anil Kapahi, Jin-Keun Choi and Chao-Tsung Hsiao. 2016. "Modeling of surface cleaning by cavitation bubble dynamics and collapse." *Ultrason. Sonochem.* 29:528–549.

Chahine, GL. 1977. "Interaction between an oscillating bubble and a free surface." *Journal of Fluids Engineering* 99(4):709–716.

Chahine, GL, KM Kalumuck and C-T Hsiao. 2003. "Simulation of surface piercing body coupled response to underwater bubble dynamics utilizing 3DYNAFS, a three-dimensional BEM code." *Computational Mechanics* 32(4-6):319–326.

Chen, Chuyi, Yuyang Gu, Juan Tu, Xiasheng Guo and Dong Zhang. 2016. "Microbubble oscillating in a microvessel filled with viscous fluid: A finite element modeling study." *Ultrasonics* 66:54–64.

Chew, Lup Wai, Evert Klaseboer, Siew-Wan Ohl and Boo Cheong Khoo. 2011. "Interaction of two differently sized oscillating bubbles in a free field." *Physical Review E* 84(6):066307.

Cole, R. H. and R. Weller. 1948. "Underwater explosions." *Physics Today* 1(6):35–35.

Coussios, C. C., C. H. Farny, G. Ter Haar and R. A. Roy. 2007. "Role of acoustic cavitation in the delivery and monitoring of cancer treatment by high-intensity focused ultrasound (HIFU)." *Int. J. Hyperthermia* 23(2):105–120.

Crum, LA. 1979. "Surface oscillations and jet development in pulsating bubbles." *Le Journal de Physique Colloques* 40(C8):C8–285.

Cui, Jie, Zhi-Peng Chen, Qianxi Wang, Tao-Ran Zhou and Callan Corbett. 2019. "Experimental studies of bubble dynamics inside a corner." *Ultrasonics Sonochemistry* p. 104951.

Curtiss, G. A., D. M. Leppinen, Q. X. Wang and J. R. Blake. 2013. "Ultrasonic cavitation near a tissue layer." *J. Fluid Mech.* 730:245–272.

De Graaf, KL, PA Brandner and I Penesis. 2014. "The pressure field generated by a seismic airgun." *Experimental Thermal and Fluid Science* 55:239–249.

Dhankhar, Poonam. 2014. "Homogenization fundamentals." *IOSR Journal of Engineering* 4(5):01–08.

Dijkink, Rory and Claus-Dieter Ohl. 2008. "Measurement of cavitation induced wall shear stress." *Applied physics letters* 93(25):254107.

Dindyal, Shiva and Constantinos Kyriakides. 2011. "Ultrasound microbubble contrast and current clinical applications." *Recent patents on cardiovascular drug discovery* 6(1):27–41.

Dular, Matevž, Tjaša Griessler-Bulc, Ion Gutierrez-Aguirre, Ester Heath, Tina Kosjek, Aleksandra Krivograd Klemenčič, Martina Oder, Martin Petkovšek, Nejc Rački, Maja Ravnikar et al. 2016. "Use of hydrodynamic cavitation in (waste) water treatment." *Ultrasonics sonochemistry* 29:577–588.

Falsafioon, Mehdi, Sina Arabi, Ricardo Camarero and Francois Guibault. 2014. Comparison of two mesh smoothing techniques for unstructured grids. In *IOP Conference Series: Earth and Environmental Science*. Vol. **22**(2) IOP Publishing p. 022020.

Farny, Caleb H, R Glynn Holt and Ronald A Roy. 2009. "The correlation between bubble-enhanced HIFU heating and cavitation power." *IEEE Transactions on Biomedical Engineering* 57(1):175–184.

Fong, Siew Wan, Deepak Adhikari, Evert Klaseboer and Boo Cheong Khoo. 2009. "Interactions of multiple spark-generated bubbles with phase differences." *Experiments in fluids* 46(4):705–724.

Freund, Jonathan B, Tim Colonius and Andrew P Evan. 2007. "A cumulative shear mechanism for tissue damage initiation in shock-wave lithotripsy." *Ultrasound in medicine & biology* 33(9):1495–1503.

Fu, Z. and V. Popov. 2011. "Application of the boundary element method to 2D and 3D bubble dynamics." *WIT Trans. Modelling Simul* 52:73–84.

Fuster, Daniel. 2019. "A review of models for bubble clusters in cavitating flows." *Flow, Turbulence and Combustion* 102(3):497–536.

Garimella, Rao V, Mikhail J Shashkov and Patrick M Knupp. 2004. "Triangular and quadrilateral surface mesh quality optimization using local parametrization." *Computer Methods in Applied Mechanics and Engineering* 193(9-11):913–928.

Goh, B. H. T., S.W. Gong, S.W. Ohl and B.C. Khoo. 2017. "Spark-generated bubble near an elastic sphere." *Int. J. Multiph. Flow* 90:156–166.

Gonzalez-Avila, Silvestre Roberto and Claus-Dieter Ohl. 2018. The acoustic pressure generated by the non-spherical collapse of laser-induced cavitation bubbles near a rigid boundary. In *Proceedings of the 10th International Symposium on Cavitation (CAV2018)*. ASME Press.

Gordillo, JM and M Pérez-Saborid. 2006. "Axisymmetric breakup of bubbles at high Reynolds numbers." *Journal of Fluid Mechanics* 562:303–312.

Guerri, L., G. R. LuccA and A. Prosperetti. 1981. A numerical method for the dynamics of non-spherical cavitation bubbles. In *Proceedings of the 2nd Inter. Colloquium on Drops and Bubbles*. pp. 175–181.

Han, Bing, Karsten Köhler, Kerstin Jungnickel, Robert Mettin, Werner Lauterborn and Alfred Vogel. 2015. "Dynamics of laser-induced bubble pairs." *Journal of Fluid Mechanics* 771:706–742.

Han, R, S Li, AM Zhang and QX Wang. 2016. "Modelling for three dimensional coalescence of two bubbles." *Physics of Fluids* 28(6):062104.

Harris, PJ. 1993. "A numerical method for predicting the motion of a bubble close to a moving rigid structure." *Communications in Numerical Methods in Engineering* 9(1):81–86.

Helfield, B., X. Chen, S. C. Watkins and F. S. Villanueva. 2016. "Biophysical insight into mechanisms of sonoporation." *Proc. Natl. Acad. Sci. U.S.A.* 113(36):9983–9988.

Hosseinkhah, N, H Chen, TJ Matula, PN Burns and K Hynynen. 2013. "Mechanisms of microbubble–vessel interactions and induced stresses: a numerical study." *The Journal of the Acoustical Society of America* 134(3):1875–1885.

Hosseinkhah, N and K Hynynen. 2012. "A three-dimensional model of an ultrasound contrast agent gas bubble and its mechanical effects on microvessels." *Physics in Medicine & Biology* 57(3):785.

Hsiao, C-T, J-K Choi, S Singh, GL Chahine, Todd A Hay, Yu A Ilinskii, EA Zabolotskaya, Mark F Hamilton, G Sankin, F Yuan et al. 2013. "Modelling single-and tandem-bubble dynamics between two parallel plates for biomedical applications." *Journal of fluid mechanics* 716:137–170.

Hsiao, Chao-Tsung, A Jayaprakash, A Kapahi, J-K Choi and Georges L Chahine. 2014. "Modelling of material pitting from cavitation bubble collapse." *J. Fluid Mech.* 755:142–175.

Hung, CF and JJ Hwangfu. 2010. "Experimental study of the behaviour of mini-charge underwater explosion bubbles near different boundaries." *Journal of Fluid Mechanics* 651:55–80.

Iloreta, JI, NM Fung and AJ Szeri. 2008. "Dynamics of bubbles near a rigid surface subjected to a lithotripter shock wave. Part 1. Consequences of interference between incident and reflected waves." *Journal of Fluid Mechanics* 616:43–61.

Ishida, Hideshi, Chayut Nuntadusit, Hideo Kimoto, Takashi Nakagawa and Takayoshi Yamamoto. 2001. 'Cavitation bubble behavior near solid boundaries'. In: CAV 2001: *Fourth International Symposium on Cavitation.* California Institute of Technology, Pasadena, CA USA.
URL: *https://resolver.caltech.edu/CAV2001:sessionA5.003*

Johnsen, Eric and Tim Colonius. 2008. "Shock-induced collapse of a gas bubble in shock-wave lithotripsy." *The Journal of the Acoustical Society of America* 124(4):2011–2020.

Joseph, D. D. and J. Wang. 2004. "The dissipation approximation and viscous potential flow." *J. Fluid Mech.* 505:365–377.

Kalumuck, KM, R Duraiswami and GL Chahine. 1995. "Bubble dynamics fluid-structure interaction simulation by coupling fluid BEM and structural FEM codes." *Journal of Fluids and Structures* 9(8):861–883.

Kang, I. S. and L. G. Leal. 1988. "The drag coefficient for a spherical bubble in a uniform streaming flow." *Phys. Fluids* 31(2):233–237.

Keller, Joseph B and Ignace I Kolodner. 1956. "Damping of underwater explosion bubble oscillations." *Journal of applied physics* 27(10):1152–1161.

Keller, Joseph B and Michael Miksis. 1980. "Bubble oscillations of large amplitude." *The Journal of the Acoustical Society of America* 68(2):628–633.

Klaseboer, E., B. C. Khoo and K. C. Hung. 2005. "Dynamics of an oscillating bubble near a floating structure." *J. Fluids Struct.* 21(4):395–412.

Klaseboer, E, KC Hung, C Wang, CW Wang, BC Khoo, P Boyce, S Debono and H Charlier. 2005. "Experimental and numerical investigation of the dynamics of an underwater explosion bubble near a resilient/rigid structure." *Journal of Fluid Mechanics* 537:387–413.

Kolasinski, Kurt W. 2014. "Bubbles: A review of their relationship to the formation of thin films and porous materials." *Open Material Sciences* 1(1).

Koukouvinis, P, M Gavaises, O Supponen and M Farhat. 2016. "Simulation of bubble expansion and collapse in the vicinity of a free surface." *Physics of Fluids* 28(5):052103.

Kucera, A and J. R. Blake. 1990. "Approximate methods for modelling cavitation bubbles near boundaries." *B. Aust. Math Soc.* 41(1):1–44.

Kucherenko, VV and VV Shamko. 1986. "Dynamics of electric-explosion cavities between two solid parallel walls." *Journal of Applied Mechanics and Technical Physics* 27(1):112–115.

Kuprat, Andrew, Ahmed Khamayseh, Denise George and Levi Larkey. 2001. "Volume conserving smoothing for piecewise linear curves, surfaces, and triple lines." *Journal of Computational Physics* 172(1):99–118.

Lamb, H. 1932. "Hydrodynamics, Cambridge Univ." *Press,* pp. 134–139.

Lauterborn, W. 1974. "Laser-induced cavitation." *Acta Acustica united with Acustica* 31(2):51–78.

Lauterborn, W. and A. Vogel. 2013. "Shock wave emission by laser generated bubbles." *Bubble dynamics and shock waves* pp. 67–103.

Lauterborn, W and H Bolle. 1975. "Experimental investigations of cavitation-bubble collapse in the neighbourhood of a solid boundary." *J. Fluid Mech.* 72(2):391–399.

Lauterborn, W and R Mettin. 2015. Acoustic cavitation: bubble dynamics in high-power ultrasonic fields. In *Power Ultrasonics*. Elsevier pp. 37–78.

Lauterborn, W. and T. Kurz. 2010. "Physics of bubble oscillations." *Rep. Prog. Phys.* 73(10):106501.

Lauterborn, W, Th Kurz, R Mettin and CD Ohl. 1999. "Experimental and theoretical bubble dynamics." *Advances in chemical physics* 110:295–380.

Lee, M., E. Klaseboer and B. C. Khoo. 2007. "On the boundary integral method for the rebounding bubble." *J. Fluid Mech.* 570:407–429.

Leslie, Thomas A and James E Kennedy. 2006. "High-intensity focused ultrasound principles, current uses, and potential for the future." *Ultrasound quarterly* 22(4):263–272.

Li, S, R Han, A. M. Zhang and Q. X. Wang. 2016. "Analysis of pressure field generated by a collapsing bubble." *Ocean Eng.* 117:22–38.

Li, S, R Han and AM Zhang. 2016. "Nonlinear interaction between a gas bubble and a suspended sphere." *Journal of Fluids and Structures* 65:333–354.

Li, Shengcai, Christopher E Brennen and Yoichiro Matsumoto. 2015. "Introduction for amazing (cavitation) bubbles.".

Li, Shuai, A-Man Zhang, Rui Han and Qingwei Ma. 2019. "3D full coupling model for strong interaction between a pulsating bubble and a movable sphere." *Journal of Computational Physics* 392:713–731.

Li, Tong. 2014. Cavitation monitoring and spatial mapping for pulsed high-intensity focused ultrasound enhanced drug delivery PhD thesis.

Li, Tong, Shiping Wang, Shuai Li and A-Man Zhang. 2018. "Numerical investigation of an underwater explosion bubble based on FVM and VOF." *Applied Ocean Research* 74:49–58.

Li, Tong, Tatiana D Khokhlova, Oleg A Sapozhnikov, Matthew O'Donnell and Joo Ha Hwang. 2014. "A new active cavitation mapping technique for pulsed HIFU applications-bubble doppler." *IEEE transactions on ultrasonics, ferroelectrics, and frequency control* 61(10):1698–1708.

Li, Zhangrui, Lei Sun and Zhi Zong. 2013. "Numerical analysis of gas bubbles in close proximity to a movable or deformable body." *Archive of Applied Mechanics* 83(12):1715–1737.

Li, Zhangrui, Lei Sun, Zhi Zong and Jing Dong. 2012. "Some dynamical characteristics of a non-spherical bubble in proximity to a free surface." *Acta Mechanica* 223(11):2331–2355.

Lind, Steven John and Timothy Nigel Phillips. 2010*a*. "The effect of viscoelasticity on a rising gas bubble." *Journal of non-Newtonian fluid mechanics* 165(15-16):852–865.

Lind, Steven John and Timothy Nigel Phillips. 2010*b*. "Spherical bubble collapse in viscoelastic fluids." *Journal of non-newtonian fluid mechanics* 165(1-2):56–64.

Lindau, Olgert and Werner Lauterborn. 2003. "Cinematographic observation of the collapse and rebound of a laser-produced cavitation bubble near a wall." *J. Fluid Mech.* 479:327–348.

Liu, Xinguo, Hujun Bao, Heung-Yeung Shum and Qunsheng Peng. 2002. "A novel volume constrained smoothing method for meshes." *Graphical Models* 64(3-4):169–182.

Liu, Y. L., S. P. Wang and A. M. Zhang. 2016. "Interaction between bubble and air-backed plate with circular hole." *Phys. Fluids* 28(6):062105.

Liu, YL, QX Wang, SP Wang and AM Zhang. 2016. "The motion of a 3D toroidal bubble and its interaction with a free surface near an inclined boundary." *Physics of Fluids* 28(12):122101.

Liu, Yunlong, A-Man Zhang, Zhaoli Tian and Shiping Wang. 2018. "Investigation of free-field underwater explosion with Eulerian finite element method." *Ocean Engineering* 166:182–190.

López-Villa, A., L. S. Zamudio and A. Medina. 2014. The Boundary Element Method in Fluid Mech.: Application to Bubble Growth. In *Experimental and Computational Fluid Mechanics*. Springer pp. 17–48.

Lucca, G. and A. Prosperetti. 1981. A numerical method for the dynamics of nonspherical cavitation bubbles. In *Proc. 2nd Int. Colloquium on Drops and Bubbles, California NASA JPL Publications*. Vol. 82 Pasadena, CA: California Institute of Technology. p. 175.

Lugli, Francesca and Francesco Zerbetto. 2007. "An introduction to bubble dynamics." *Physical Chemistry Chemical Physics* 9(20):2447–2456.

Luo, Jing, Weilin Xu, Jun Deng, Yanwei Zhai and Qi Zhang. 2018. "Experimental study on the impact characteristics of cavitation bubble collapse on a wall." *Water* 10(9):1262.

Lv, Liang, Yongxue Zhang, Yuning Zhang and Yuning Zhang. 2019. "Experimental investigations of the particle motions induced by a laser-generated cavitation bubble." *Ultrasonics Sonochemistry* 56:63 – 76.
URL: *http://www.sciencedirect.com/science/article/pii/S1350417718313968*

Maeda, Kazuki, Tim Colonius, Wayne Kreider, Adam Maxwell and Michael Bailey. 2016. "Modeling and experimental analysis of acoustic cavitation bubble clouds for burst-wave lithotripsy." *The Journal of the Acoustical Society of America* 140(4):3307–3307.

Manmi, Kawa. 2015. Three dimensional acoustic microbubble dynamics near rigid boundary PhD thesis University of Birmingham.

Manmi, Kawa and Qianxi Wang. 2017. "Acoustic microbubble dynamics with viscous effects." *Ultrasonics sonochemistry* 36:427–436.

Marui, Tomohiro. 2013. "An introduction to micro/nano-bubbles and their applications." *Systemics, Cybernetics and Informatics* 11(4):68–73.

Miao, Hongyu and Sheryl M Gracewski. 2008. "Coupled FEM and BEM code for simulating acoustically excited bubbles near deformable structures." *Computational Mechanics* 42(1):95–106.

Mohamed, Nurul Akmal. 2013. Numerical solution and spectrum of boundary-domain integral equations PhD thesis Brunel University, School of Information Systems, Computing and Mathematics.

Mushtaq, Muhammad, Nawazish Ali Shah and Ghulam Muhammad. 2010. "Advantages and disadvantages of boundary element methods for compressible fluid flow problems." *J. Am. Sci* 6(1):162–165.

Najafi, Aref Seyyed, Zhenghe Xu and Jacob Masliyah. 2008. "Single micro-bubble generation by pressure pulse technique." *Chemical Engineering Science* 63(7):1779–1787.

Naude, Charl F and Albert T Ellis. 1961. "On the mechanism of cavitation damage by nonhemispherical cavities collapsing in contact with a solid boundary." *Journal of Basic Engineering* 83(4):648–656.

Ohl, Claus-Dieter, Olgert Lindau and Werner Lauterborn. 1998. "Luminescence from spherically and aspherically collapsing laser induced bubbles." *Physical Review Letters* 80(2):393.

Ohl, S. P. and R. E. Allison. 2006. Ultrasonic Inline Inspection of the Moomba to Sydney Pipeline. In *Proceedings of the 6th International Pipeline Conference, Calgary, AB, Canada*. pp. 25–29.

Ohl, S. W., D. W. Wu, E. Klaseboer and B. Khoo. 2015. Spark bubble interaction with a suspended particle. In *J. Phys. Conf. Ser.* Vol. 656 IOP Publishing p. 12033.

Ohl, Siew-Wan, Evert Klaseboer and Boo Cheong Khoo. 2015. "Bubbles with shock waves and ultrasound: a review." *Interface focus* 5(5):20150019.

Ory, E, Huipin Yuan, Andrea Prosperetti, S Popinet and S Zaleski. 2000. "Growth and collapse of a vapor bubble in a narrow tube." *Physics of fluids* 12(6):1268–1277.

Pahk, Ki Joo, Pierre Gélat, Hyungmin Kim and Nader Saffari. 2018. "Bubble dynamics in boiling histotripsy." *Ultrasound in medicine & biology* 44(12):2673–2696.

Pearson, A., E. Cox, J. R. Blake and S. R. Otto. 2004. "Bubble interactions near a free surface." *Eng. Anal. Bound Elem* 28(4):295–313.

Pearson, A, JR Blake and SR Otto. 2004. "Jets in bubbles." *Journal of Engineering Mathematics* 48(3-4):391–412.

Peng, Chi, Shouceng Tian, Gensheng Li and Michael C Sukop. 2018. "Single-component multiphase lattice Boltzmann simulation of free bubble and crevice heterogeneous cavitation nucleation." *Physical Review E* 98(2):023305.

Philipp, A. and W. Lauterborn. 1998. "Cavitation erosion by single laser-produced bubbles." *J. Fluid Mech.* 361:75–116.

Plesset, Milton S and Richard B Chapman. 1971. "Collapse of an initially spherical vapour cavity in the neighbourhood of a solid boundary." *Journal of Fluid Mechanics* 47(2):283–290.

Plesset, MS. 1954. "On the stability of fluid flows with spherical symmetry." *Journal of Applied Physics* 25(1):96–98.

Poulain, S., G. Guenoun, S. Gart, W. Crowe and S. Jung. 2015. "Particle motion induced by bubble cavitation." *Phys. Rev. Lett.* 114(21):214501.

Rayleigh, Lord. 1917. "VIII. On the pressure developed in a liquid during the collapse of a spherical cavity." *The London, Edinburgh, and Dublin Philosophical Magazine and Journal of Science* 34(200):94–98.

Reuter, Fabian and Sebastian A Kaiser. 2019. "High-speed film-thickness measurements between a collapsing cavitation bubble and a solid surface with total internal reflection shadowmetry." *Physics of Fluids* 31(9):097108.

Roberts, W. W., T. L. Hall, K. Ives, J. S. Wolf, J. B. Fowlkes and C. A. Cain. 2006. "Pulsed cavitational ultrasound: a noninvasive technology for controlled tissue ablation (histotripsy) in the rabbit kidney." *J. Urol* 175(2):734–738.

Rosselló, JM, W Lauterborn, M Koch, T Wilken, T Kurz and R Mettin. 2018. "Acoustically induced bubble jets." *Physics of Fluids* 30(12):122004.

Rypl, Daniel and J Nerad. 2016. "Volume preserving smoothing of triangular isotropic three-dimensional surface meshes." *Advances in Engineering Software* 101:3–26.

Sandip, Mehta, Kumar Anil and Raghav ingh. 2017. "Computational Electromagnetics: Techniques and Applications." *International Journal for Research in Applied Science & Engineering Technology* 5(X1):122–125.

Sankin, G. N., F. Yuan and P. Zhong. 2010. "Pulsating tandem microbubble for localized and directional single-cell membrane poration." *Phys. Rev. Lett.* 105(7):078101.

Shima, A, K Takayama, Y Tomita and N Miura. 1981. "An experimental study on effects of a solid wall on the motion of bubbles and shock waves in bubble collapse." *Acta Acustica united with Acustica* 48(5):293–301.

Shima, A and Y Sato. 1980. "The behavior of a bubble between narrow parallel plates." *Zeitschrift für angewandte Mathematik und Physik ZAMP* 31(6):691–704.

Shima, A and Y Tomita. 1977. "On the behavior of a spherical bubble and the impulse pressure in a viscous compressible liquid." *Bulletin of JSME* 20(149):1453–1460.

Shima, A and Y Tomita. 1981. "The behavior of a spherical bubble near a solid wall in a compressible liquid." *Ingenieur-Archiv* 51(3-4):243–255.

Shrikant, B Randhavane and AK Khambete. 2017. "Hydrodynamic Cavitation: A Novel Treatment Approach." *Materials Today: Proceedings* 4(9):9680–9684.

Sousa, Fabrício Simeoni de, A Castelo, LG Nonato, N Mangiavacchi and JA Cuminato. 2007. "Local volume-conserving free surface smoothing." *Communications in numerical methods in engineering* 23(2):109–120.

Soyama, H. 1992. Cavitation observations of severely erosive vortex cavitation arising in a centrifugal pump. In *Proc. 3rd Int. Conf. Cavitation, I Mech E, Cambridge*. pp. 103–110.

Sreedhar, BK, SK Albert and AB Pandit. 2017. "Cavitation damage: Theory and measurements–A review." *Wear* 372:177–196.

Supponen, Outi, Danail Obreschkow, Philippe Kobel, Marc Tinguely, Nicolas Dorsaz and Mohamed Farhat. 2017. "Shock waves from nonspherical cavitation bubbles." *Phys. Rev. Fluid* 2(9):093601.

Szeri, Andrew J, Brian D Storey, Antony Pearson and John R Blake. 2003. "Heat and mass transfer during the violent collapse of nonspherical bubbles." *Phys. Fluids* 15(9):2576–2586.

Tagawa, Yoshiyuki and Ivo R Peters. 2018. "Bubble collapse and jet formation in corner geometries." *Phys. Rev. Fluid* 3(8):081601.

Taib, B. B. 1985. Boundary integral method applied to cavitation bubble dynamics PhD thesis Univ. of Wollongong NSW, Australia: .

Tanizawa, Katsuji. 1995. A nonlinear simulation method of 3-d body motions in waves: formulation with the acceleration potential. In *10th Workshop on Water Waves and Floating Bodies, Oxford*.

Taubin, Gabriel. 1995. Curve and surface smoothing without shrinkage. In *Proceedings of IEEE international conference on computer vision*. IEEE pp. 852–857.

Tian, ZL, YL Liu, AM Zhang and SP Wang. 2018. "Analysis of breaking and re-closure of a bubble near a free surface based on the Eulerian finite element method." *Computers & Fluids* 170:41–52.

Tomita, Y and A Shima. 1986. "Mechanisms of impulsive pressure generation and damage pit formation by bubble collapse." *J. Fluid Mech.* 169:535–564.

Tomita, Y, K Sato and A Shima. 1994. Interaction of two laser-produced cavitation bubbles near boundaries. In *Bubble Dynamics and Interface Phenomena*. Springer pp. 33–45.

Tomita, Y, P. B. Robinson, R. P. Tong and J. R. Blake. 2002. "Growth and collapse of cavitation bubbles near a curved rigid boundary." *J. Fluid Mech.* 466:259–283.

Tong, RP, Werner P Schiffers, Stephen J Shaw, John Robert Blake and DC Emmony. 1999. "The role of splashingin the collapse of a laser-generated cavity near a rigid boundary." *Journal of Fluid Mechanics* 380:339–361.

Tsiglifis, Kostas and Nikos A Pelekasis. 2007. "Nonlinear oscillations and collapse of elongated bubbles subject to weak viscous effects: effect of internal overpressure." *Physics of Fluids* 19(7):072106.

Ueki, Hiroshi, Hideo Kimoto and Kazunari Momse. 1984. "Behavior of a spark-induced bubble between parallel walls." *Bulletin of JSME* 27(229):1358–1365.

van Wijngaarden, Leen. 2016. "Mechanics of collapsing cavitation bubbles." *Ultrasonics sonochemistry* 29:524–527.

Virot, Matthieu, Tony Chave, Sergey I Nikitenko, Dmitry G Shchukin, Thomas Zemb and Helmuth Mohwald. 2010. "Acoustic cavitation at the water- glass interface." *The Journal of Physical Chemistry C* 114(30):13083–13091.

Vogel, A, W Lauterborn and R Timm. 1989. "Optical and acoustic investigations of the dynamics of laser-produced cavitation bubbles near a solid boundary." *J. Fluid Mech.* 206:299–338.

Vyas, Nina, Emilia Pecheva, Hamid Dehghani, Rachel L Sammons, Qianxi X Wang, David M Leppinen and A Damien Walmsley. 2016. "High speed imaging of cavitation around dental ultrasonic scaler tips." *PloS One* 11(3):e0149804.

Vyas, Nina, H Dehghani, RL Sammons, QX Wang, DM Leppinen and AD Walmsley. 2017. "Imaging and analysis of individual cavitation microbubbles around dental ultrasonic scalers." *Ultrasonics* 81:66–72.

Wang, C and BC Khoo. 2004. "An indirect boundary element method for three-dimensional explosion bubbles." *Journal of Computational Physics* 194(2):451–480.

Wang, C, BC Khoo and KS Yeo. 2003. "Elastic mesh technique for 3D BIM simulation with an application to underwater explosion bubble dynamics." *Computers & fluids* 32(9):1195–1212.

Wang, Jia-xia, Kun Liu, Ming-zuo Jiang and Shi-jie Yuan. 2020. "Numerical simulation of the coupled response of stiffened structures subjected to explosion bubble loading." *Journal of Marine Science and Technology* pp. 1–17.

Wang, Q. X. 1998. "The evolution of a gas bubble near an inclined wall." *Theor. Comput. Fluid Dyn.* 12(1):29–51.

Wang, Q. X. 2004. "Numerical simulation of violent bubble motion." *Phys. Fluids* 16(5):1610–1619.

Wang, Q. X. and J. R. Blake. 2011. "Non-spherical bubble dynamics in a compressible liquid. Part 2. Acoustic standing wave." *J. Fluid Mech.* 679:559–581.

Wang, Q. X. and K. Manmi. 2014. "Three dimensional microbubble dynamics near a wall subject to high intensity ultrasound." *Phys. Fluids* 26(3):032104.

Wang, Qianxi. 2014. "Multi-oscillations of a bubble in a compressible liquid near a rigid boundary." *Journal of Fluid Mechanics* 745:509–536.

Wang, Qianxi. 2016. "Local energy of a bubble system and its loss due to acoustic radiation." *Journal of Fluid Mechanics* 797:201–230.

Wang, QX. 2005. "Unstructured MEL modelling of nonlinear unsteady ship waves." *Journal of Computational Physics* 210(1):368–385.

Wang, QX. 2013. "Non-spherical bubble dynamics of underwater explosions in a compressible fluid." *Physics of Fluids* 25(7):072104.

Wang, QX and JR Blake. 2010. "Non-spherical bubble dynamics in a compressible liquid. Part 1. Travelling acoustic wave." *Journal of Fluid Mechanics* 659:191–224.

Wang, QX, KS Yeo, BC Khoo and KY Lam. 1996. "Nonlinear interaction between gas bubble and free surface." *Computers & fluids* 25(7):607–628.

Wang, Shi-Ping, Qianxi Wang, A-Man Zhang and Eleanor Stride. 2019. "Experimental observations of the behaviour of a bubble inside a circular rigid tube." *International Journal of Multiphase Flow* 121:103096.

Wang, SP, QX Wang, DM Leppinen, AM Zhang and YL Liu. 2018. "Acoustic bubble dynamics in a microvessel surrounded by elastic material." *Physics of Fluids* 30(1):012104.

Wang, Zhikai, Dongyan Shi and Aman Zhang. 2015. "Three-dimensional lattice Boltzmann simulation of bubble behavior in a flap-induced shear flow." *Computers & Fluids* 123:44–53.

Watanabe, H. and H. Hashimoto. 1996. "Effects of solid particle properties on cavitation erosion in solid-water mixtures." *J. Fluids Eng.* 118:749.

Wilkerson, Stephen. 1992. A boundary integral approach for three-dimensional underwater explosion bubble dynamics. Technical report Army ballistic research lab Aberdeen Proving ground MD.

Wu, G. X. 1998. "Hydrodynamic force on a rigid body during impact with liquid." *J. Fluid Struct.* 12(5):549–559.

Wu, GX and ZZ Hu. 2004. "Simulation of nonlinear interactions between waves and floating bodies through a finite-element-based numerical tank." *Proceedings of the Royal Society of London. Series A: Mathematical, Physical and Engineering Sciences* 460(2050):2797–2817.

Wu, Ting-Hsiang, Yue Chen, Sung-Yong Park, Jason Hong, Tara Teslaa, Jiang F Zhong, Dino Di Carlo, Michael A Teitell and Pei-Yu Chiou. 2012. "Pulsed laser triggered high speed microfluidic fluorescence activated cell sorter." *Lab on a Chip* 12(7):1378–1383.

xia Wang, Jia, Zhi Zong, Kun Liu and Jie Cui. 2018. "Simulations of the dynamics and interaction between a floating structure and a near-field explosion bubble." *Applied Ocean Research* 78:50–60.

Xu, W., Y. Zhang, J. Luo, Q. Zhang, Y. Zhai et al. 2017. "The impact of particles on the collapse characteristics of cavitation bubbles." *Ocean Sci. J.* 131:15–24.

Zhang, A. M. and Y. L. Liu. 2015. "Improved three-dimensional bubble dynamics model based on boundary element method." *J. Comp. Phys.* 294:208–223.

Zhang, AM and BY Ni. 2014. "Three-dimensional boundary integral simulations of motion and deformation of bubbles with viscous effects." *Computers & Fluids* 92:22–33.

Zhang, Jing, Lingxin Zhang and Jian Deng. 2019. "Numerical Study of the Collapse of Multiple Bubbles and the Energy Conversion during Bubble Collapse." *Water* 11(2):247.

Zhang, S., J. H. Duncan and G. L. Chahine. 1993. "The final stage of the collapse of a cavitation bubble near a rigid wall." *J. Fluid Mech.* 257:147–181.

Zhang, S., J. H. Duncan and G. L. Chahine. 1994. The behavior of a cavitation bubble near a rigid wall. In *Bubble Dynamics and Interface Phenomena*. Springer pp. 429–436.

Zhang, Y., Z. Qian, B. Ji and Y. Wu. 2016. "A review of microscopic interactions between cavitation bubbles and particles in silt-laden flow." *Renew. Sustainable Energy Rev.* 56:303–318.

Zhang, YL, KS Yeo, BC Khoo and C Wang. 2001. "3D jet impact and toroidal bubbles." *Journal of Computational Physics* 166(2):336–360.